

Laser manipulation of
donor-bound electrons in
ultra-pure $^{28}\text{Si}:\text{P}$

Von der Fakultät für Mathematik und Physik
der Gottfried Wilhelm Leibniz Universität
Hannover

zur Erlangung des Grades
Doktor der Naturwissenschaften
Dr. rer. nat.

Genehmigte Dissertation von

M. Sc. Eduard Enrico Sauter

2022

Referent: Prof. Dr. Michael Oestreich
Korreferent: Prof. Dr. Ilja Gerhardt
Korreferent: Prof. Dr. Stephan Reitzenstein
Tag der Promotion: 19.12.2022

*We are currently in the midst of a second quantum revolution.
The first quantum revolution gave us new rules that govern
physical reality.
The second quantum revolution will take these rules and use them
to develop new technologies.*

— Dowling and Milburn [1]

ABSTRACT

Harnessing the quantum nature of donor atoms in silicon may pave the way for a quantum revolution in the modern digital information era. The idea to combine the exceptional spin coherence properties of donor electron spins in silicon with the prospect of exploiting technology prevalent in the semiconductor industry is very appealing. This thesis provides a quantitative limit for the spin coherence times of phosphorus donor-bound electrons in silicon, which is a fundamental parameter for spin-based quantum computation. To this end, the spin-lattice relaxation time in $^{28}\text{Si:P}$ is measured with the highest degree of precision to date for unprecedentedly low temperatures. The measurements yield extremely long spin-lattice relaxation times exceeding twenty hours, which is orders of magnitude larger than originally determined. These long spin-relaxation times confirm the latent potential for devices based on spin manipulation donor electrons in silicon. For very low temperatures and high magnetic fields, the impact of the bosonic phonon distribution on the spin-relaxation time is observed for the very first time and with high accuracy which was predicted by theory more than 60 years ago.

Furthermore, a new method of measuring the bandgap using donor electrons based on optical spectroscopy of the D^0X transition is presented. This new method can be used to locally detect the lattice temperature via the Si bandgap with exceptional accuracy and excellent temporal resolution. With the help of this method, measurements of the bandgap temperature dependence are performed with 7×10^{-10} relative precision. Although the precise measurements verify the theoretical T^4 limit of the bandgap energy shift with high certainty, a discrepancy of the absolute shift questions the existing theory of electron-phonon coupling in semiconductors in the low temperature limit. Additional time-resolved experiments facilitate the use of this new method as a precise local thermometer to be used in $^{28}\text{Si:P}$ based devices.

KEYWORDS: Laser spectroscopy, spin dynamics, semiconductors, spintronics

KURZZUSAMMENFASSUNG

Die Ausnutzung der Quanteneigenschaften von Donatoratomen in Silizium ist ein möglicher Weg, die moderne Ära der Digitalisierung zu revolutionieren. Der Ansatz, die außerordentlichen Kohärenzzeiten von Donatorspins in Silizium mit der Verwendung von existierender Technologie in der Halbleiterindustrie zu kombinieren ist hierbei sehr vielversprechend. Diese Arbeit setzt einen quantitativen Grenzwert für die Spinkohärenzzeiten von Phosphordonor Elektronen fest, welcher einen fundamentalen Parameter für spinbasierte Quantenberechnung darstellt. Um den intrinsischen Grenzwert zu bestimmen, wird die Spin-Gitter-Relaxationszeit mit der größten bis heute erreichten Präzision im Bereich sehr tiefer Temperaturen gemessen. Die resultierenden Relaxationszeiten sind länger als 20 Std. und überschreiten Größenordnungen des ursprünglich gefundenen Grenzwertes, was einen Beweis für das noch ungetastete Potenzial für Spinmanipulation von Donatoratomen in Silizium liefert. Für sehr geringe Temperaturen und hohe Magnetfelder wird zum ersten Mal der vor 60 Jahren theoretisch vorhergesagte Einfluss der bosonischen Phononenverteilung auf die Spinrelaxationszeit beobachtet.

Weiterhin wird in dieser Arbeit eine neue, schnelle und präzise Methode präsentiert, um die lokale Gittertemperatur von Siliziumspin Geräten zu messen, welche auf der Detektion der Bandlücke basiert. Mithilfe dieser Methode wird die Verschiebung der Bandlücke mit einer relativen Präzision von 7×10^{-10} gemessen. Die Messungen verifizieren die theoretisch vorhergesagte T^4 Abhängigkeit der Verschiebung. Allerdings stellt der Absolutwert der Verschiebung die existierende Theorie der Phononen-Elektronen-Wechselwirkung für Halbleiter bei geringen Temperaturen infrage. Weitere zeitaufgelöste Messungen motivieren die Verwendung dieser neuen Methode als präzises lokales Thermometer für $^{28}\text{Si:P}$ Spinbasierte Geräte.

SCHLÜSSELWÖRTER: Laserspektroskopie, Spindynamik, Halbleiter, Spintronik

ACKNOWLEDGEMENTS

If I have seen further it is by standing on the shoulders of Giants.

— Isaac Newton (1675)

I would like to thank all the people who have supported me in creating this thesis. First and foremostly, I am grateful for the excellent supervision of Michael Oestreich who provided the ideas for the projects as well as the laboratory equipment necessary to perform advanced measurements. My gratefulness also extends to Jens Hübner, my co-supervisor. They were always present for discussions providing important suggestions. Only due to them did my research result in high-quality papers that were proudly published.

I would like to thank Nikolay Abrosimov from the IKZ in Berlin for providing the $^{28}\text{Si:P}$ sample, showing us their crystal growth facilities, and a lot of insight about the ^{28}Si sample growth in general. I thank Mike Thewalt and Stephanie Simmons at the SFU in Vancouver for welcoming me into their labs for a few weeks, which helped me to understand a lot more about cryogenic spectroscopy and their exciting experiments with defects in Si in the past and present. I extend great thanks to all the Femtos for the nice barbecues and good working atmosphere. I especially thank Pavel Sterin for so many helpful discussions about programming, machining, cryostats, measurements in frequency space, noise and many more topics. I also thank Carsten Schinke from the solar energy department for helpful discussions about the dynamics of free carriers in natural Si.

I am indebted to the *Quantum Frontiers* research program for financing my position and allowing me to participate in online events of an excellent international research school. I would also like to thank Ilja Gerhardt who kindly agreed to act as co-supervisor. Last but not least, I would like to thank all the referees for expending their time to evaluate my thesis.

CONTENTS

I	INTRODUCTION AND CONTEXT	1
1	MOTIVATION	3
2	SPIN QUBITS	5
2.1	Silicon impurities for quantum technologies	8
3	$^{28}\text{Si:P}$ OPTICAL SPECTROSCOPY	11
3.1	Temperature dependence of the bandgap	13
II	THEORY AND MODELS	15
4	SILICON	17
4.1	Energy band structure	17
4.2	Transitions across the bandgap	19
4.3	Temperature dependence of the bandgap	20
5	DONOR BOUND ELECTRONS	25
5.1	Fine structure and hyperfine structure	28
5.2	Donor bound excitons	31
5.3	D^0X absorption spectrum	35
5.4	Spin relaxation and dephasing	36
5.5	D^0 spin-lattice relaxation	37
5.6	D^0 spin-spin relaxation	39
5.7	Three level system and optical pumping	40
III	SETUP AND METHODS	43
6	OVERVIEW	45
6.1	Setup and methods	47
6.2	Cryogenics	48
6.3	Sample insert	48
7	SIGNAL RECOVERY	53
7.1	Absorption spectroscopy	53
7.2	Optical absorption spectra in Si	54
7.3	Phase modulation absorption spectroscopy	57
7.4	Lock-in amplification	64
8	STABLE LASERS FOR SPECTROSCOPY	69
8.1	External cavity diode laser	69

8.2	Fizeau interferometer	72
8.3	High finesse optical cavity resonator	73
8.4	Pound-Drever-Hall laser stabilization	75
8.5	Heterodyne beat-lock interferometer	78
IV	EXPERIMENTS AND RESULTS	81
9	BANDGAP TEMPERATURE DEPENDENCE	83
9.1	Introduction	83
9.2	Setup	84
9.3	Temperature dependence of the bandgap	88
9.4	Sample heating and cooling dynamics	91
10	LOW-TEMPERATURE RELAXATION OF D ⁰ ELEC- TRON SPINS	101
10.1	Introduction	101
10.2	Setup and methods	102
10.3	Results	106
V	SUMMARY AND OUTLOOK	113
11	SUMMARY	115
12	OUTLOOK	119
12.1	Spectral hole burning	119
12.2	Microresonators for ESR	127
12.3	Sample insert for ESR	129
	BIBLIOGRAPHY	131

LIST OF FIGURES

Figure 1	The intensity on the screen in a double-slit experiment	6
Figure 2	The silicon crystals form in a diamond structure	18
Figure 3	Band structure of silicon	18
Figure 4	A simplified sketch of different possible electron-hole recombination mechanisms in silicon . .	19
Figure 5	Temperature dependence of the Si bandgap	21
Figure 6	Binding energies in units of eV for some donor and acceptor states in silicon according to Ref. [27].	26
Figure 7	Donor bound states of the shallow phosphorus impurity in silicon	26
Figure 8	The probability density functions of the phosphorus donor bound electron	27
Figure 9	The energy diagram of shallow donor states without magnetic field according to Ref. [37]. The electron has several far-infrared transitions within the ground state D^0 , and a donor-bound exciton transition $D^0 \rightarrow D^0X$. .	28
Figure 10	Hyperfine splitting and clock transitions of the D^0	30
Figure 11	The $D^0 \rightarrow D^0X$ transition energy diagram .	32
Figure 12	A resonant absorption experiment on an Avogadro-type $^{28}\text{Si:P}$ sample reveals the twelve dipole-allowed transitions $D^0 \rightarrow D^0X$	33
Figure 13	The width of the absorption lines in samples of different isotopic and phosphorus or boron impurities	34
Figure 14	A flow diagram of the spin relaxation paths	38
Figure 15	Optical pumping in a three-level system . .	40

Figure 16	The measured donor electron spin polarization as a function of the pump rate and the spin relaxation time	42
Figure 17	The setup for laser spectroscopy of the donor-bound exciton transition at very low temperatures	46
Figure 18	A three-quarter section of the sample insert for low-temperature measurements	49
Figure 19	A schlieren image of the $^{28}\text{Si}:\text{P}$ sample inside the insert obtained by illumination with laser light from the back	50
Figure 20	Band-to-band absorption in Si at different temperatures	55
Figure 21	The zero field no-phonon absorption spectrum of the donor-bound exciton in the sample under investigation	57
Figure 22	Sideband power in PM modulation	59
Figure 23	Different PM absorption spectra are calculated from the demodulation of a Lorentzian distribution	61
Figure 24	The dependence of the amplitude of the demodulated signal and the spectral distortion on the modulation index a and frequency ω_m	62
Figure 25	A flow diagram of lock-in detection	64
Figure 26	A typical power spectrum that includes the signal and different sources of noise in the experiment	66
Figure 27	Functional principle of an AlGaAs quantum well diode laser	70
Figure 28	Two different external cavity diode laser designs	71
Figure 29	Schematic of a Fizeau interferometer used to measure the wavelength of coherent light	73
Figure 30	The home-built optical cavity resonator operating in a higher-order spatial mode	74
Figure 31	The setup used to stabilize a laser using the PDH technique	76

Figure 32	Transmission function of the cavity and PDH signal	77
Figure 33	The flow diagram of an optical phase-locked loop (OPLL)	78
Figure 34	The setup for stabilizing of a heterodyne beat signal between the scanning laser and the reference laser	79
Figure 35	The frequency spectrum of the beat signal	80
Figure 36	Experimental setup for measuring the bandgap shift using the D^0X transition	85
Figure 37	The measured dependence of the spectrum amplitude and center frequency on probe laser position relative to the sample	86
Figure 38	The effect of the mixing chamber pressure on the detected D^0X frequency.	87
Figure 39	Temperature dependence of the bandgap of silicon	89
Figure 40	Temperature dependent frequency change before and after SiO_2 removal	90
Figure 41	The D^0X resonance frequency dynamics after switching the ABE excitation on and off	92
Figure 42	The lattice temperature dynamics calculated according to Eq. 42	94
Figure 43	A flow diagram of the heat transfer model used to explain the results in Fig. 42	95
Figure 44	The measured temperature response for periodic modulation of heat flow	96
Figure 45	Results of fast ABE modulation with only 20 ms period and extraction of the temperature differences for different base temperatures	97
Figure 46	The relative sensitivity of different contactless temperature sensing techniques	98
Figure 47	The D^0X PM absorption spectrum at different magnetic fields	102
Figure 48	The setup for measuring the T_1 relaxation times	103

Figure 49	The polarization scan and time dependent polarizations	104
Figure 50	The dependence of the spin polarization decay times τ on the pause interval	105
Figure 51	The magnetic field dependence of T_1 for intermediate temperatures 2.5 K to 3.6 K.	107
Figure 52	External data for spin relaxation rates.	108
Figure 53	The spin relaxation time T_1 for very low temperatures and various magnetic fields	110
Figure 54	The resonant peaks in the D^0X absorption spectrum and the cavity transmission spectrum	120
Figure 55	The PM demodulation spectrum obtained from probing the linearly polarized π_- transition in a transverse magnetic field	121
Figure 56	Experimental anti-hole spectrum obtained from subtracting spectra with different pump powers	122
Figure 57	Persistent spectral hole which is burned and probed by the same laser	123
Figure 58	Evolution of the persistent spectral hole for increasing pump durations	125
Figure 59	Widths and depths of persistent spectral holes	125
Figure 60	Layout of a niobium microresonator	127
Figure 61	The exchange-gas sample insert for simultaneous optical absorption and ESR experiments	129

LIST OF TABLES

Table 1	Performance of various qubits	7
Table 2	The natural abundance of the stable isotopes of silicon	11
Table 3	A listing of different enriched bulk samples .	12
Table 4	Constants in the Breit-Rabi equation	29
Table 5	Performance parameters of the optical cavity resonator	75
Table 6	Thermal resistances and capacities of the heat transfer model	96
Table 7	Coefficients for calculation of the spin relaxation rate	109

ACRONYMS

ULE	Ultra-Low Expansion
ECDL	External-Cavity Diode Laser
LD	Laser Diode
PD	Photo Diode
HV	High-Voltage
AWG	Arbitrary Waveform Generator
ABE	Above Bandgap Excitation
PZT	Lead Zirconium Titanate
SAF	Surface-Angle-Facet
HVA	High-Voltage Amplifier
PBS	Polarizing Beam Splitter
EOM	Electro-Optic Modulator
LPF	Lowpass Filter
LO	Local Oscillator
PDH	Pound-Drever-Hall
FWHM	Full Width at Half Maximum
ESR	Electron Spin Resonance
NMR	Nuclear Magnetic Resonance
MZI	Mach-Zehnder Interferometer
PLL	Phase-Locked Loop
OPLL	Optical Phase-Locked Loop

PM Phase Modulation

PI Proportional Integral

PID Proportional Integral Derivative

RF Radio Frequency

GLOSSARY

$^{28}\text{Si:P}$ Isotopically enriched silicon doped with phosphorus

D^0 Donor-bound electron

D^0X Donor-bound exciton

T_1 Spin(-lattice) relaxation time

T_2 Spin(-spin) coherence time

e Elementary charge

\hbar Reduced Planck constant

ϵ_0 Vacuum permittivity

ϵ_r Relative permittivity

Θ_D Debye temperature

m_e Electron mass

m^* Relative effective electron mass

γ_e Electron gyromagnetic ratio

g_e Electron g-factor

γ_n Nuclear gyromagnetic ratio

g_n Nuclear g-factor

μ_B (Electron) Bohr magneton

μ_n Nuclear Bohr magneton

B Magnetic flux density

k_B Boltzmann constant

δ Bandgap shift

- γ Resonance linewidth
 α Absorption coefficient
 κ Extinction coefficient
 f Frequency
 T Temperature
 t Time

Part I

INTRODUCTION AND CONTEXT

MOTIVATION

Quantum objects are vanishingly tiny compared to things we see every day, but they continue to amaze us with unintuitive behavior that seems unpredictable. Although research should be sufficiently motivated by curiosity, it is also possible to gain an advantage in our lives by utilizing systems that exhibit these fascinating and unique quantum properties. The prospect of improving our lives with quantum technology has continued to drive the funding of projects around the world in recent years.

Many problems are very difficult to solve with a classical computer. One such popular problem is the efficient prime factorization of large numbers. Shor's quantum algorithm provides means to solve data encryption problems by factoring large numbers using a quantum computer. Quantum computers excel at this task, and even modestly sized quantum computers outperform the largest supercomputers that exist today. Another challenge is the simulation of quantum systems such as large molecules that make up life as we know it. Not surprisingly, quantum computers excel at simulating quantum systems, and therefore they are bound to become a very useful tool to solve problems in physics, nanotechnology, chemistry, biology, and pharmacology. With the development of quantum computers being a comparably young research field, the possible applications of quantum computing will likely exceed the scope imaginable as of now, and more interesting fields based on quantum technology will emerge in the years to come.

The quantum bit (qubit) is the evolution of the classical bit from two discrete states, on and off, to a continuum of states that exist inside a vector space. Reproducible manipulation of the state of n qubits means accurately controlling a quantum state in a vector space of 2^n complex dimensions. This task proved to be very challenging due to the fragility of quantum states (especially entangled states) compared to discrete bits. While we can scale the size of a classical bit, e.g. a transistor, to make it more robust, this is

usually not possible for a quantum bit because the increase in size increases the likelihood of decoherence and therefore degrades the quality of the qubit. Ironically, it is also not possible to shrink a classical transistor to an arbitrary size because the latent quantum properties of matter begin to emerge.

Modern computers can rely on a high bit count and an efficient infrastructure to compensate for the quantum mechanical miniaturization limit. If we compare the transistor (bit) count of several billion in modern processing units to a painstakingly designed state-of-the-art quantum computer which only has about a hundred qubits, each working sub-optimally, it becomes obvious that there is still a lot of research to do. We, as physicists, are left with the challenging task of finding more suitable materials and understanding their unique quirks as well as evaluating them according to benchmarks such as fidelity and coherence times, so that we may ultimately improve that number. It should be remarked that the number of qubits is not directly a measure of quantum computer performance. The way qubits interact and keep in a well-defined state massively influences the ability of a quantum computer to solve modern day problems. As a result, different physical implementations of qubits will lead to a largely different result, even by using the same amount of qubits. The next chapter will discuss some of the most popular qubit implementations, including silicon donor spin qubits.

SPIN QUBITS

A qubit is a quantum mechanical two-level system whose state can be initialized, coherently controlled, and measured with system-dependent fidelity. Research efforts focus on physical implementations and materials that offer the best prospects for large-scale integration. Although solid-state implementations of quantum computers somewhat lack behind trapped ions, infrared photons, or superconducting qubits currently, semiconductor spin qubits offer a lot of advantages if some of the technical problems can be overcome [2]. The field of semiconductor qubits itself includes a variety of systems, materials, and setups. Any useful implementation of a qubit system will impose challenging requirements on the manufacturing process and require a suitable environment that is challenging to maintain. Hard to maintain millikelvin temperatures, very high vacuums, and very little electromagnetic disturbance are only some prime examples. Even if the ambient conditions are met and measurement and manipulation of the quantum state of a qubit become possible, the interaction between many qubits is a large hurdle that many implementations cannot overcome. Probably the most quoted source of criteria for a good qubit architecture is authored by DiVincenzo [3]. The DiVincenzo criteria are briefly summarized below.

SCALABILITY The number of well-characterized qubits that can be combined in a single platform. Well-characterized means that, despite a high number of qubits, an accurate physical description including a differential equation for each qubit exists, which completely describes the state of the qubit and the interaction with other qubits.

INITIALIZATION The quantum state of the whole system needs to be initialized into a well-defined state, such as the ground state, before performing further operations. This is similar to initializing a classical register with a certain number in order

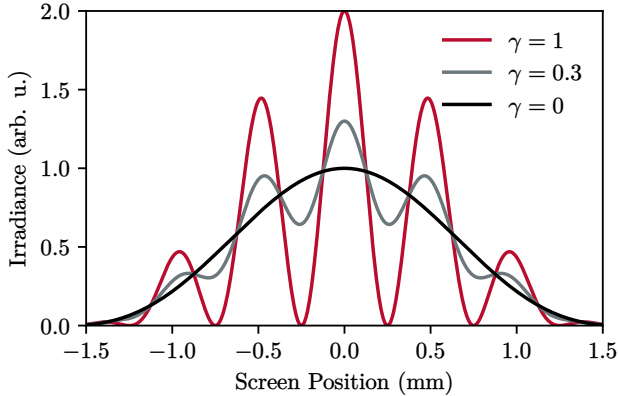


Figure 1: The intensity on the screen in a double-slit experiment. This figure illustrates how spatial coherence ($\gamma = 1$) results in observable interference. Partially coherent light ($\gamma = 0.3$) produces only a reduced contrast in the interference fringes, and incoherent light ($\gamma = 0.0$) has no observable fringes at all.

to, e.g., compute the sum with a different register. The efficient initialization is of utmost importance for quantum error correction, because it requires the qubits to be initialized into the original state many times over.

COHERENCE The coherence time for a quantum state is the period over which there is no mixing with other states and the state remains pure. There exists a principal mechanism in quantum mechanics that, after the decoherence of a state, classical behavior emerges. The result of the double-slit experiment in Fig. 1 illustrates how interference is lost by decoherence.

UNIVERSAL SET OF QUANTUM GATES Similar to a classical computer, there are sets of fundamental logical operations that can be chained to perform any possible operation in state space. The difference from a classical computer is that the operations are continuous transformations within a certain time where the strength can be tuned, e.g., by the in-

Type of qubit	T_2	Error (%)
Infrared photon	0.1 ms	0.016
Trapped Ion	15 s	0.48
Trapped Neutral Atom	3 s	5
Liquid molecule nuclear spins	2 s	0.01
e^- spin in GaAs quantum dot	3 μ s	5
e^- spins bound to $^{28}\text{Si}:\text{P}$	0.6 s	5
^{29}Si nuclear spins in ^{28}Si	25 s	5
NV centre in diamond	2 ms	2
Superconducting circuit	4 μ s	0.7

Table 1: Demonstrated performance of various qubits according to Ref. [4]. The error represents the deviation from 100 % fidelity.

tensity of laser light or a microwave field. In this sense, quantum gate operations are tunable interactions between different qubits that need to be accurately implemented for the quantum algorithm to succeed.

QUBIT-SPECIFIC MEASUREMENT CAPABILITY It should be possible to perform measurements on every individual qubit in the system independently. The quantum efficiency of these measurements determines how much information is lost during each measurement and is an important benchmark for the performance of a quantum computing platform.

Several qubit platforms are being researched extensively, and each has benefits and downsides. Table 1 lists some examples including the corresponding coherence times T_2 and error rates, which are direct complements of the fidelity. It should be noted that the values in Tab. 1 are not fundamentally limited, but depend on engineering and environmental parameters and are likely to change in the future as technology improves.

Phosphorus impurities embedded in enriched ^{28}Si host material, in particular, fulfill all the DiVincenzo criteria above [2] and thus are a promising platform for quantum computation. Their coher-

ence times are comparable to those of trapped ions, but unlike trapped ions, solid-state spin qubits do not require an ultra-high vacuum environment. $^{28}\text{Si:P}$ spin qubits are close to their maximum coherence time already at around 4 K [5] which is far above the operating temperature of superconducting qubits on the order of ≈ 10 mK. The main downside of silicon spin qubits is the lack of a convenient infrastructure to address and manipulate individual qubits like waveguides and junctions connecting superconducting qubits. However, it is not unreasonable to assume that this technological challenge can be overcome with extensive research [6].

2.1 SILICON IMPURITIES FOR QUANTUM TECHNOLOGIES

Semiconductivity in silicon is a collective, macroscopic phenomenon that depends on the density and type of the dopants and the temperature. However, through increased miniaturization of nanoscale devices, the quantum behavior of single dopants becomes more and more apparent. Many recent approaches commonly aim to harness the quantum nature of spins in silicon which arise from the electronic structure of single dopants [2, 7, 8]. On the smallest scale, single dopants are suggested for use in quantum computing in order to encode quantum information into the nuclear spin of a phosphorus atom in $^{28}\text{Si:P}$ [9]. More recently, single defects in Si have been investigated using optical methods [7] and their spin state is manipulated efficiently. Even the infrastructure for quantum technologies based on optical manipulation of defect spins in Si is advancing at a rapid rate [8]. On a slightly larger scale, there are several approaches based on coupling small ensembles of donors to the microwave field of superconducting resonators in order to encode quantum information into donors [10–14]. In this thesis, an ensemble of $^{28}\text{Si:P}$ donors is used, and their spin state is manipulated by resonant laser absorption.

The ^{31}P donor atoms of phosphorus in silicon possess an additional valence electron compared to the Si host atoms. Changes in the electric field around the substitutional site as a result of the different number of valence electrons between the impurity and host atoms are screened by the neighboring valence electrons of the host atoms and electrons. The screening effect reduces the binding en-

ergy of the outermost electrons and the binding potential becomes comparable to a Coulomb potential [15]. Accordingly, the wavefunctions are, in good approximation, comparable to those of the hydrogen atom. The weak binding potential of the electron in this artificial atom is low enough to allow a significant amount of carriers to escape into the neighboring energy bands even at room temperature.

Since the binding energy of the electron for the shallow impurity is low, it is easily excited into one of the higher energy states at elevated temperatures and it becomes impossible to observe any quantum properties. However, at cryogenic temperatures below 20 K, the electron is frozen in the ground state and quantum behavior emerges, which can be detected using fluorescence or resonant microwave excitation methods. In one of the first experiments, Fletcher *et al.* were able to determine the hyperfine splitting of the electron-donor system in the ground state at liquid helium temperatures [16]. Not long after, Luttinger and Kohn developed the effective mass theory for impurity states in silicon [17] to accurately predict the value of the hyperfine splitting. The fine structure splitting of the phosphorus-bound electron was also measured in more detail a few years later [18]. All existing experiments confirm that the phosphorus atom in silicon possesses a weakly bound electron (45 meV) in a 1s-like orbital with a Bohr radius of $r = 4\pi\hbar^2\epsilon_0\epsilon_r/(m_e e^2) \approx 2$ nm. The weakly bound electron, labeled as D^0 , has a donor bound exciton transition $D^0 \rightarrow D^0X$ that is used in this thesis to manipulate the donors via resonant laser absorption.

$^{28}\text{Si}:\text{P}$ OPTICAL SPECTROSCOPY

The fascinating results of magnetic resonance experiments on doped Si and the emergence of laser technology were followed by several optical absorption experiments on donors in Si. However, optical spectroscopy with $^{\text{nat}}\text{Si}:\text{P}$ was mainly restricted to determining the fine structure of donors and donor-bound excitons in high magnetic fields where the splittings become larger than the optical linewidths of donor-bound exciton transitions [19]. The linewidths of optical band-to-band transitions are limited by the residual impurity concentration and the natural isotopic composition of silicon (Tab. 2) and therefore largely depend on the quality of the material used in the experiments. The increasing purity of available silicon material soon caused the isotopic composition to become a limiting factor for the optical linewidths. The increase in linewidth due to the random isotopic distribution was accurately described by M. Cardona [20], who is on the forefront of research on isotope effects in the solid-state. The purest solid-state material ever refined originated in the context of the Avogadro project, which aimed to create a sphere consisting of exactly¹ $6.022\,14 \times 10^{23}/28$ silicon atoms [21]. As a result of the Avogadro project, ultra-pure enriched ^{28}Si material became available which allowed measuring the isotopic broadening of the near-infrared electronic transitions [22]. The result is a remarkable ensemble linewidth of 30 MHz for the bound exciton transition. Different samples made available by the

¹ They achieved a final relative uncertainty in the atom number of 2×10^{-8}

Isotope	^{28}Si	^{29}Si	^{30}Si
Concentration (%)	92.2	4.7	3.1

Table 2: The natural abundance of the stable isotopes of silicon.

Name	^{28}Si %	Phosphorus (cm^{-3})	Boron (cm^{-3})
nat	92.23	5×10^{14}	3×10^{13}
c	99.92	5×10^{14}	3×10^{13}
b	99.983	2×10^{13}	2×10^{14}
a	99.991	2×10^{12}	5×10^{13}
3.3.1	99.991	2×10^{14}	1×10^{14}
3.3.6	99.991	7×10^{14}	1×10^{14}
3.3.7	99.991	7×10^{14}	1×10^{14}
3.3.9	99.991	1×10^{15}	1×10^{14}
3.1.6	99.995	1.2×10^{15}	5×10^{13}
avo	99.995	5×10^{11}	1×10^{13}

Table 3: A listing of different bulk samples and their respective impurity concentrations measured by Thewalt’s group and in this work (3.1.6). The silicon material was enriched and refined throughout the Avogadro project. The *Leibniz-Institut für Kristallzüchtung* kindly provided doped Avogadro Si material in bulk samples for experiments.

Avogadro project (listed in Tab. 3) all were produced by the IKZ after receiving inquiries from M. L. W. Thewalt and M. Cardona and all the initial measurements on these samples were performed by Thewalt’s group. In a landmark experiment, they determined a very long coherence time of the ionized phosphorus nuclear spin exceeding 30 minutes at room temperature in a ^{28}Si sample [23]. This result was achieved by optically addressing and ionizing the nuclear spin ensemble using the neutral donor-bound exciton transitions.

Although much work on nuclei in $^{28}\text{Si:P}$ has been done by the same group, information on electron spin relaxation was still lacking up to this date. The latest published experiments on phosphorus donor electron spin relaxation date back more than half a century ago with ambiguous results, particularly for temperature and magnetic field dependence [18, 24]. The task in question is to provide experimental proof of the mechanisms involved in the relax-

ation of the donor electron spins in $^{28}\text{Si:P}$ using optical absorption spectroscopy of the bound exciton transition.

3.1 TEMPERATURE DEPENDENCE OF THE BANDGAP

Device performance can be highly influenced by temperature, which is made evident, e.g., by the strong temperature dependence of the spin relaxation times. Using external temperature sensors may lead to undesired systematic errors in the measured device temperature. Especially fast changes in temperature are hard to detect because of the delayed temperature response. The bandgap of silicon has a distinct temperature dependence that can be used to measure the lattice temperature locally within the sample. Measuring the bandgap directly by optical band-to-band absorption does not yield a sufficient relative precision for determining the temperature in the regime below 20 K. Fortunately, there exists a method to measure the bandgap in $^{28}\text{Si:P}$ using optical spectroscopy of the bound electrons [25] which can be used to directly measure the lattice temperature. The temperature dependence of the bandgap can be measured via this method with a high degree of precision by utilizing the energetically narrow donor-bound exciton transition. This thesis aims to precisely quantify the temperature dependence of the bandgap using the donor-bound exciton transition in $^{28}\text{Si:P}$ and use the measured information for directly determining of the time-dependent local lattice temperature. To this end, a setup is presented that allows all-optical, and contactless measurements of the lattice temperature with exceptional temporal resolution. The setup is used to verify the temperature dependence in the low-temperature limit with much higher precision and lower temperatures compared to existing measurements in Ref. [25].

Part II

THEORY AND MODELS

SILICON

Silicon crystallizes in the diamond structure (Fig. 2), which consists of two interpenetrating face-centered cubic lattices displaced along the diagonal by $\frac{a}{4}$ where $a \approx 0.543$ nm is the lattice spacing between the atoms. The diamond structure and the strong covalent atomic bonds make silicon a very hard and brittle material. Bulk silicon has an opaque appearance due to its bandgap that causes absorption of light in the visible region. Silicon can form two different oxides SiO and SiO₂ where the former is less commonly found and the latter is commonly known in its crystalline form as quartz, the native oxide of silicon. SiO₂ layers naturally form with a thickness of a few nanometers within hours of exposure of Si to oxygen [26]. Silicon is favored in semiconductor manufacturing, mainly because the SiO₂ oxide layer is chemically very inert and highly insulating. Surface passivation is a crucial part in creating a plethora of complex devices based on metal oxide-semiconductor technology, e.g., CPUs and power electronics. This fact, combined with its large natural abundance, makes silicon the workhorse of the semiconductor industry.

4.1 ENERGY BAND STRUCTURE

In order to understand the interaction of Si with visible and infrared light, it is necessary to study the energy band states of the electrons involved in the bonding of the atoms. The energy of electrons generally depends on their crystal momentum, which is derived from the Bloch equations [15]. Calculating the energies of electrons using the Bloch formalism in complex crystals like Si can be done only numerically in general. Figure 3 shows the result of such numerical calculations for the case of silicon. The structure of the Si valence bands is very similar to that of other semiconductors such as GaAs and Ge, with the exception that the bands degen-

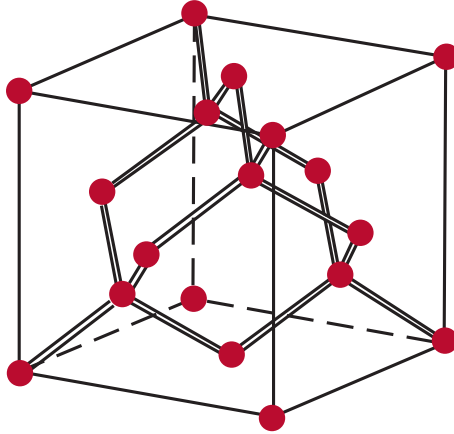


Figure 2: The silicon crystals form in a diamond structure. From Ref. [15].

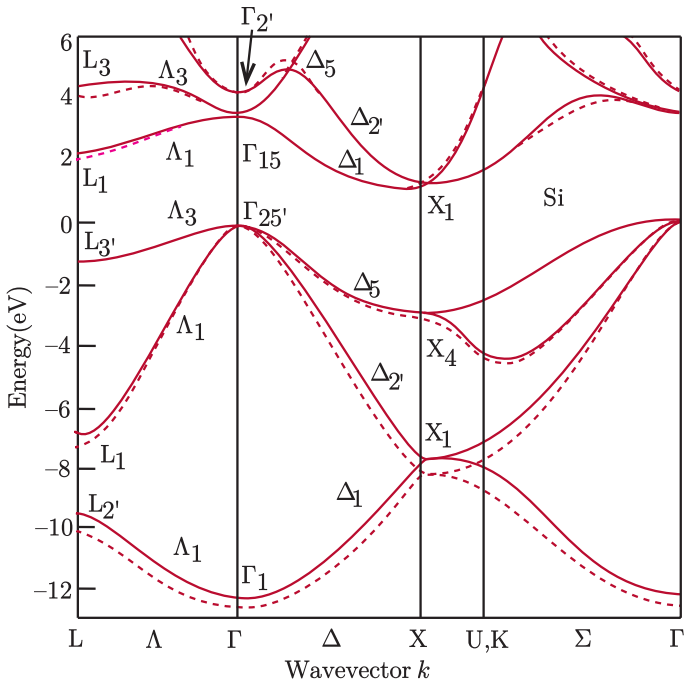


Figure 3: Band structure of silicon. From Ref. [15].

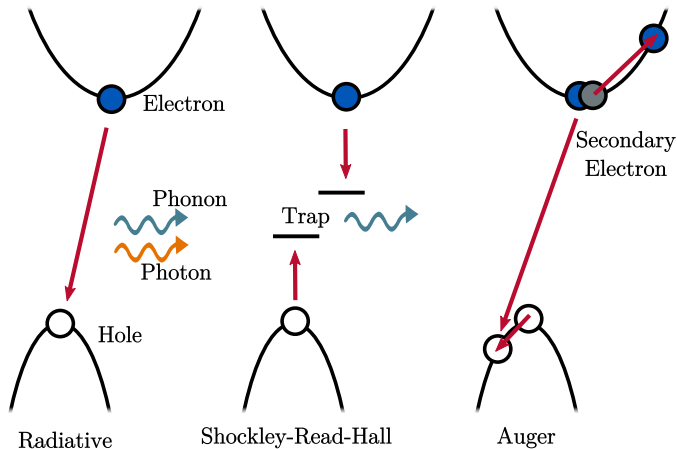


Figure 4: A simplified sketch of different possible electron-hole recombination mechanisms in silicon.

erate at the Γ'_{25} maximum point in the Brillouin zone because of the lack of spin-orbit coupling. Like all semiconductors, Si has a bandgap between the valence band and the conduction band. The conduction band minimum is displaced from the Brillouin zone center Γ , located at $0.85X$ [27]. The proximity to the X point makes silicon an indirect semiconductor.

4.2 TRANSITIONS ACROSS THE BANDGAP

The indirect nature of the Si bandgap causes electrons in transition from the conduction band to the valence band to experience a change in momentum. There are several possible momentum-conserving electron-hole recombination mechanisms, which are sketched in Fig. 4. Because momentum is conserved, it needs to be transferred to either another electron, a phonon, or some type of dislocation within the lattice. Photons carry only very little momentum, and therefore radiative transitions in Si must be phonon assisted leading to radiative lifetimes that are much longer than those in direct semiconductors. Radiative transitions occurring with-

out the assistance of phonons are also possible, but only if the electron is captured in a defect state, e.g., a shallow phosphorus donor. The difference in momentum for so called *zero-phonon* transitions is absorbed by a defect and the energy difference is compensated almost completely by the photon. Phonon-assisted radiative transitions can occur at several energy offsets, where the phonon momentum matches the difference in electron momentum. Phonon-assisted transitions experience an additional frequency broadening caused by the phonon energy dispersion and the finite lifetime of phonons [28]. This broadening is very relevant for optical absorption experiments, making zero-phonon transitions a much preferred alternative.

Defect-assisted recombination can occur with deep defects under the emission of a phonon, where the momentum difference is absorbed by the defect state. This mechanism is called Shockley-Read-Hall recombination. Lastly, an important non-radiative inter-band transition mechanism is the Auger recombination, where the electron and hole recombine and transfer the excess energy and momentum to a secondary electron which is raised to the conduction band. The secondary electron usually relaxes in small energy steps, generating many acoustic phonons during the process. This mechanism is dominant at either high free carrier densities or for localized electronic states such as the phosphorus donor-bound exciton state. Decay via the Auger mechanism results in many phonons generated from the excess energy of the carrier, which in turn results in an increased temperature. This temperature change impacts the bandgap of silicon, which is demonstrated by precise measurements of the bandgap in this thesis.

4.3 TEMPERATURE DEPENDENCE OF THE BANDGAP

Arguably the most prominent feature of silicon is the conveniently sized energy gap. With a value of ≈ 1.12 eV at 300 K, the gap is large enough to sufficiently suppress thermal generation of carriers and still small enough to absorb visible light, making silicon an ideal semiconductor for transistor and light-sensing applications. The size of the bandgap can be tuned within a certain range, as it increases for $T \rightarrow 0$ to about 1.17 eV. There are several approaches

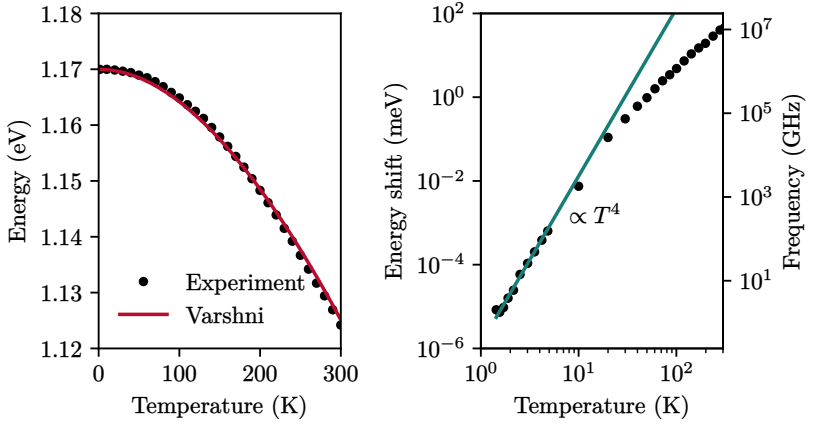


Figure 5: Temperature dependence of the Si bandgap. The data is from Ref. [30].

to quantitatively describe this temperature dependence, the most common being the phenomenological Varshni relation [29]

$$E_g(T) = E_0 - \frac{\alpha T^2}{\beta + T}, \quad (1)$$

where $E_0 \approx 1.17$ eV, $\alpha \approx 7 \times 10^{-4}$ eV K⁻¹, and $\beta \approx 1100$ K are empirical parameters that depend on the material. Figure 5 shows a comparison of the experimental data with Eq. 1. The Varshni relation fits the data well, but it has no theoretical foundation. The formula predicts a quadratic temperature dependence for $T \rightarrow 0$ where theory requires a T^4 dependence [25]. However, the Varshni relation is widely used despite the availability of more accurate theoretical alternatives derived from Bose-Einstein statistical factors [30].

The temperature dependence of the bandgap can be decomposed into two components, one due to the lattice contraction and the other due to the electron-phonon interaction [30]. A T^4 dependence for low temperatures can be derived from the latter using the volume deformation potential in combination with the Grüneisen parameters that describe the change in the frequencies of phonons

$\omega(\vec{q}, r)$ depending on the volume of the sample V for a quasi-harmonic potential. A small uniform expansion of the crystal by δV shifts the energy of the electronic band extremum $E_n(\vec{q})$ by an amount

$$\delta E_n(\vec{q}) = a_n(\vec{q}) \frac{\delta V}{V}, \quad (2)$$

where $a_n(\vec{q})$ is the volume deformation potential of the energy level $E_n(\vec{q})$ in the n -th band at the point \vec{q} in the momentum space [15].

In practice, there are very few experimental techniques that can directly measure the volume deformation potential. In order to indirectly measure the volume deformation with optical experiments, the energy differences between two bands are determined in dependence on hydrostatic pressure, which induces a volume change according to

$$p = -B \frac{\delta V}{V} - \frac{\partial}{\partial V} \sum_{\vec{q}, r} \frac{1}{2} \hbar \omega_r(\vec{q}) - \hbar \sum_{\vec{q}, r} \frac{\partial \omega_r(\vec{q})}{\partial V} \frac{1}{\exp \frac{\hbar \omega_r(\vec{q})}{k_B T} - 1}. \quad (3)$$

Here, p is the hydrostatic pressure, B is the bulk modulus, and $r = 3r'N$ with N being the number of atoms in the crystal and r' the number of atoms in the unit cell [31]. Equation 3 contains the partial derivative of the frequency with the volume. For a harmonic potential, the frequencies of the phonon modes are independent of the volume $\frac{\partial \omega_r(\vec{q})}{\partial V} = 0$ meaning the sample volume only depends on the pressure p . For a quasi-harmonic potential, the Grüneisen parameters are defined as

$$\gamma_r(\vec{q}) = -\frac{V}{\omega_r(\vec{q})} \frac{\partial \omega_r(\vec{q})}{\partial V}. \quad (4)$$

The values for the Grüneisen parameters for Si generally depend on the phonon branch and momentum, but are mostly very close to unity [15]. Seeing that the electron-phonon interaction depends on the Grüneisen parameters, it is possible to approximate the deformation energy using experimental values of γ_r .

Simplifying Eq. 3 is possible in the low temperature limit by using the Debye approximation for the phonon density of states.

Within the Debye model, the phonon frequencies are approximated by a linear dispersion¹ $\omega_r(\vec{q}) \approx q\nu_r$ where ν_r is the speed of sound. The sum of the phonon modes can be approximated by an integral that includes the phonon density of states² for each phonon branch $D_r(q) = \frac{V}{2\pi^2} \frac{q^2}{\nu_r}$ [31]. Here, the volume dependency of the phonon energy in the distributional term of Eq. 3 is neglected because $\delta V \frac{\partial \hbar\omega_r}{\partial V} \ll k_B T$ holds within the first-order approximation.

Within the Debye limit, subtracting the temperature dependent part and using an averaged Grüneisen parameter for all phonon branches $\gamma_r(\vec{q}) \rightarrow \bar{\gamma}$, as well as an isotropic constant deformation potential $a_n(\vec{q}) \rightarrow \bar{a}$, Eq. 2 becomes [32]

$$\begin{aligned} \delta E(T) - \delta E(T=0) &= \frac{9\bar{a}\bar{\gamma}}{BV_0} \hbar\omega_D \left(\frac{T}{\Theta_D} \right)^4 \\ &\times \int_0^{\Theta_D/T} dx \frac{x^3}{\exp x - 1}. \end{aligned} \quad (5)$$

Here, V_0 is the volume of the unit cell, $\Theta_D = \hbar\omega_D/k_B$ is the Debye temperature, and $\omega_D = \nu(6\pi^2 N/V)^{1/3}$ is the Debye frequency.

The ratio Θ_D/T is very large for temperatures far below the Debye temperature, and the integral approaches the constant $\pi^4/15$ resulting in a simple T^4 power law for the temperature dependence of the bandgap. Using approximate experimental values for the deformation potential of $\bar{a} \approx -30$ eV [33] and the Debye temperature $\Theta_D \approx 645$ K, $V_0 = (0.543 \text{ nm})^3$, $\bar{\gamma} \approx 1$ as well as the bulk modulus $B \approx 100$ GPa, the temperature dependence becomes $E(T) - E(0) \approx -1 \text{ eV}(T/\Theta_D)^4$. There exists only one experimental value of the prefactor ≈ -250 eV, which is more than two orders of magnitude larger [25] than the given estimate. Another more sophisticated calculation is shown in Ref. [32] that concludes with a prefactor roughly sixty times smaller than the experimentally determined value. A substantial part of this thesis is dedicated to confirming the T^4 limit of the bandgap at temperatures even lower than those in Ref. [25] and to measure the prefactor with greater precision using the bound exciton transitions of the donors in ²⁸Si:P.

¹ This approximation is ideal for the acoustic phonon branches.

² This is also called the “large crystal approximation”.

DONOR BOUND ELECTRONS

Although the electronic band structure describes the energy relation of free electrons well, doping silicon with, e.g., phosphorus or boron atoms introduces additional states for holes or electrons into the system with energies inside the bandgap. Figure 6 shows the energy levels of some common dopants for silicon. Phosphorus and boron, which are widely used in the large-scale manufacturing of semiconductor devices, both have a binding energy of approximately 45 meV. The lower binding energy, compared to hydrogen, stems from the fact that the extra charge and mass of the donor or acceptor are shielded by the covalent silicon electrons. The states of holes and electrons in Si:P are called shallow impurity states due to their low binding energy. A quantitative description of shallow impurities is given by effective mass theory [34]. The effective mass m^* describes the charge and mass shielding of electrons using a parabolic energy-momentum relationship around the band extremum [15].

The energetic states of shallow donor-bound electrons are located directly below the conduction band, as shown in Fig. 7. The corresponding binding energy can be computed from the hydrogen 1s ionization energy

$$E = -\frac{E_R m^*}{\epsilon_r^2 m_0}, \quad (6)$$

where $E_R \approx 13.6$ eV is the Rydberg energy, m^* is the effective mass ratio, and m_0 is the mass of the free electron. The effective mass of conduction electrons in silicon is not isotropic with respect to the crystal axes, but it is possible to estimate the binding energy with an effective mass $m^* = (m_{\perp} + m_{\parallel})/2 \approx (0.191 + 0.916)/2m_0$. Together with the relative permittivity of silicon $\epsilon_r \approx 11.4$, the binding energy becomes 58 meV [35]. This value has the right order of magnitude, but does not exactly match the experimental

Li	Sb	P	As	Bi	Te	Ti	C	Mg
<u>.033</u>	<u>.039</u>	<u>.045</u>	<u>.054</u>	<u>.069</u>	Conduction (1.12 eV)			<u>.110</u>
					<u>.140</u>	<u>.210</u>	<u>.250</u>	
Center (0.56 eV)								
				<u>.300</u>	<u>.340</u>		<u>.350</u>	
<u>.045</u>	<u>.067</u>	<u>.072</u>	<u>.160</u>					<u>.170</u>
Valence (0 eV)								
B	Al	Ga	In	Tl	Pd		Na	Be

Figure 6: Binding energies in units of eV for some donor and acceptor states in silicon according to Ref. [27].

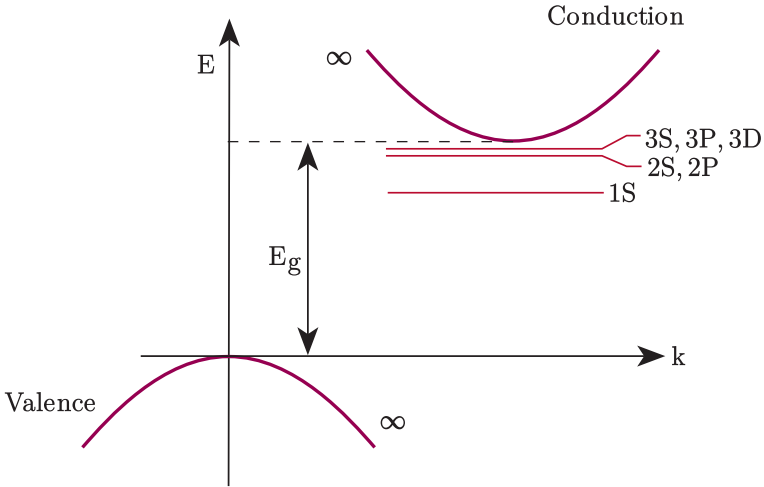


Figure 7: Donor bound states of the shallow phosphorus impurity in silicon. The conduction band has a quasi-infinite amount of states for the free electron, with a parabolic energy-momentum relation close to the band edges. From Ref. [15].

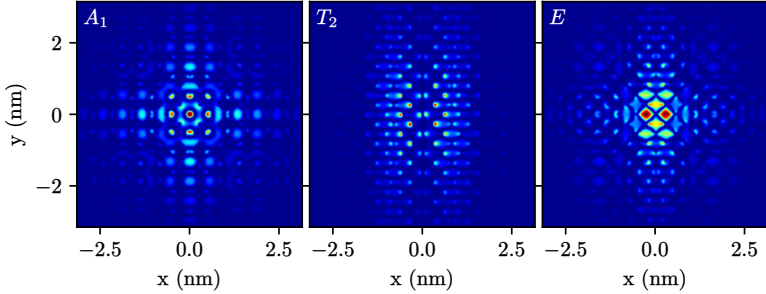


Figure 8: The A_1 , T_2 , E probability density functions for the $1s$ orbital (left to right accordingly) for the phosphorus donor bound electron. The orbitals were calculated using multivalley envelope functions according to Ref. [36].

value of 45 meV. The main reason why effective mass theory does not accurately predict the binding energies is the strong attractive potential that leads to valley-orbit coupling and deviations from the Coulomb potential [36]. Figure 8 shows the wave functions for the donor ground state that were calculated from a multivalley envelope effective mass approach, which accurately predicts the binding energies.

For the excited donor states, the situation becomes more complicated because the reduction in symmetry causes some valley-dependent degeneracies to be lifted. Figure 9 shows the energy levels of the shallow donor states, including the excited states. On the left side of Fig. 9 are the labels for the ground state and the first excited state within the effective mass approximation. The electron in its ground state has a large overlap with the donor atom, resulting in a large valley splitting. Although there are six conduction band valleys, the levels are still degenerate for each irreducible representation of the donor tetrahedral symmetry group A_1, T_2, E [15]. Valley splitting is also relevant for the $2s$ state, which has a large overlap with the donor nucleus, but not for the $2p$ states, where there is no overlap [37].

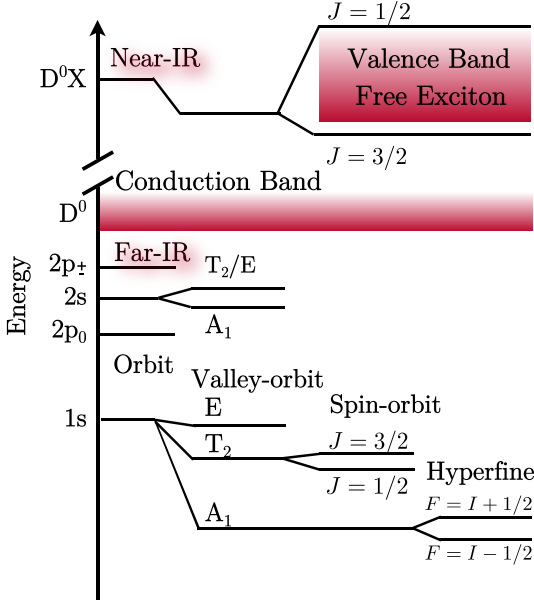


Figure 9: The energy diagram of shallow donor states without magnetic field according to Ref. [37]. The electron has several far-infrared transitions within the ground state D^0 , and a donor-bound exciton transition $D^0 \rightarrow D^0X$.

5.1 FINE STRUCTURE AND HYPERFINE STRUCTURE

The donor-bound electron and the phosphorus nucleus have a spin $\frac{1}{2}$, which leads to an observable hyperfine-structure interaction and magnetic field dependence of the energy levels of the four possible spin orientations. Spin-orbit coupling is negligible for the ground state energy of the donor $1s, A_1$ resulting in an isotropic g-factor of the electron spin with a value of $g \approx 2$, very close to the free-electron value. The electron-nuclear spin system is very well described by the Breit-Rabi model [38]. In this model, a nuclear spin \hat{I} is coupled to the electron spin \hat{S} and both are coupled to the static external magnetic field \hat{B} . This quantum mechanical description uses the Breit-Rabi Hamiltonian and gyromagnetic ratios for

γ_e	γ_n	A	g_e	g_n
27.972 GHz T ⁻¹	17.252 MHz T ⁻¹	117.53 MHz	2	2

Table 4: The constants in Eq. 7 according to Ref. [18]. The g-factors g_e and g_n are calculated from the gyromagnetic ratios using $\gamma_e = \frac{g_e \mu_B}{\hbar}$ and $\gamma_n = \frac{g_n \mu_n}{\hbar}$ with μ_B being the Bohr magneton, μ_n the nuclear magneton, and \hbar the Planck constant.

electron and nuclear spin, γ_e and γ_n , respectively, as well as the hyperfine constant A :

$$\hat{H} = -\gamma_e \hat{S} \cdot \hat{B} - \gamma_n \cdot \hat{B} + A \hat{S} \cdot \hat{I}. \quad (7)$$

Solving Eq. 7 for the eigenvalues of \hat{H} with electron spin $\frac{1}{2}$ and $\gamma_n \ll \gamma_e$ results in the energies of the electron-nuclear spin system

$$E(F_{\pm}, m, B) = \pm \frac{A}{4} + AF \sqrt{1 + 2mx + x^2}, \quad (8)$$

where $F = \pm \frac{1}{2}$ is the projected electron spin, $m = 0$ corresponds to antiparallel spin orientation, $m = 1$ corresponds to parallel spin orientation, and $x = \frac{\gamma_e B}{A}$ is the ratio of electron magnetic field splitting to the zero field splitting. The upper part of Fig. 10 shows the four energy levels at a low magnetic field $B < 100$ mT. Both electron branches scale linearly at higher fields $B > 100$ mT according to the electron Zeeman splitting with the hyperfine splitting remaining below 117 MHz for $B < 3.4$ T. The lower part of Fig. 10 shows the difference frequency between the F_+ and F_- branches. The parallel spin branches follow a linear dependency for the magnetic field energies, and the antiparallel spin branches show an anticrossing with the parallel branches for higher field values. The energy difference between the parallel and antiparallel spin branches change rapidly for small magnetic field values. There are two clock transitions at $B_0 = 0$ mT and $B_0 = 84.5$ mT where the magnetic field differential vanishes.

$$\frac{d}{dB} [E(F, 0, B) - E(F, 1, B)] = 0 \quad (9)$$

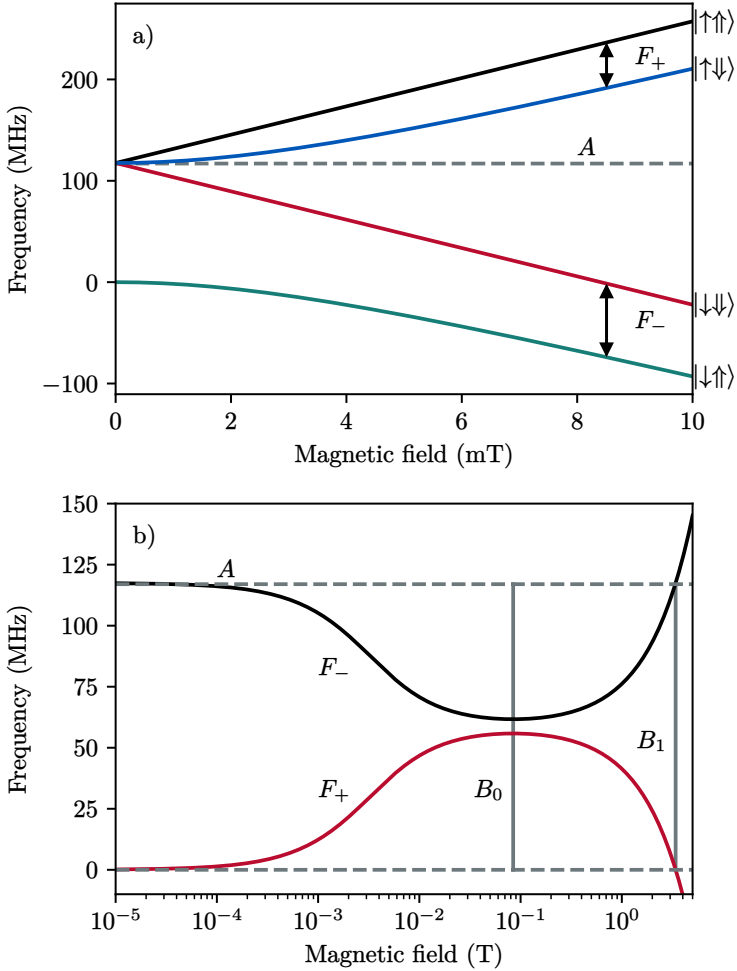


Figure 10: Energy levels of the D^0 electron ground state calculated from Eq. 8 using the constants in Tab. 4. **(a)** The hyperfine splitting A at 0 T and the clock transitions of the donor ground state at B_0 are shown on a logarithmic scale according to Eq. 8. Above a magnetic field of B_1 , the nuclear spin effectively decouples from the electron spin. **(b)** Relative energy differences between nuclear states of the donor electron spin complex for low magnetic field values.

At this point, the F_+ branch splitting has a global maximum, and the F_- branch splitting has a global minimum:

$$E(F_+, 0, B_0) - E(F_+, 0, B_0) = 56 \text{ MHz}, \quad (10)$$

$$E(F_-, 0, B_0) - E(F_-, 0, B_0) = 62 \text{ MHz}. \quad (11)$$

The F_+ branches eventually intersect around $B_1 \approx 3.4 \text{ T}$ where the F_- branch energy difference is exactly A for $B = B_1$ in Eq. 8:

$$E(F_+, 0, B_1) - E(F_+, 0, B_1) = 0 \text{ MHz}, \quad (12)$$

$$E(F_-, 0, B_1) - E(F_-, 0, B_1) = 117 \text{ MHz}. \quad (13)$$

Above this magnetic field value B_1 , the electron and nuclear spin are essentially uncoupled.

5.2 DONOR BOUND EXCITONS

Excitons are Coulomb-correlated electron-hole pairs created by interband transitions of electrons in semiconductors. When the sample contains a small number of donors, excitons are attracted to these neutral impurities by van der Waals interaction if the temperature is sufficiently low [15]. The binding energy of electron-hole pairs is lowered in the vicinity of the impurity, and the excitons exist in an impurity-bound state. In the case of Si:P, a single electron-hole pair is bound to a neutral phosphorus donor D^0 , and the phosphorus donor-bound exciton is labeled D^0X . There exists a more general theory of bound multiple exciton complexes for donors in Si with excited states, which can be described using a shell model [39]. The multiexciton complexes only form under conditions of very high excitation and thus are not relevant here.

For a single bound exciton D^0X in Si:P, the donor electron and the conduction electron form a spin singlet, leaving only an observable fine structure splitting of the heavy hole with spin $j = \frac{3}{2}$. The spin singlet has an increased binding energy of $\approx 5 \text{ meV}$ compared to the free exciton [40]. Hyperfine interaction is absent for the D^0X due to the non-existing overlap between the exciton wave function and the donor nucleus. The energies of the light hole and the heavy hole are degenerate in the ground state of the bound ex-

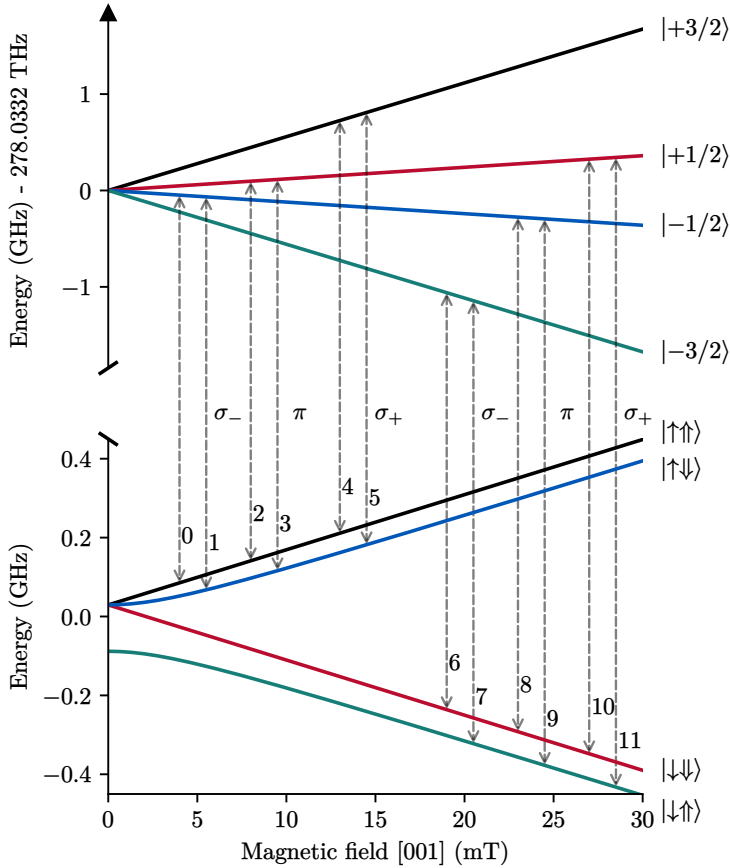


Figure 11: The $D^0 \rightarrow D^0X$ transition energy diagram. On the bottom are the D^0 ground state energies and on the top are the D^0X energies. Each transition is labeled as either linearly polarized π or circularly polarized σ_{\pm} . The numbers 0 to 11 mark the ascending order of the difference energies for the allowed transitions. The order is valid for magnetic fields below 3.4 T.

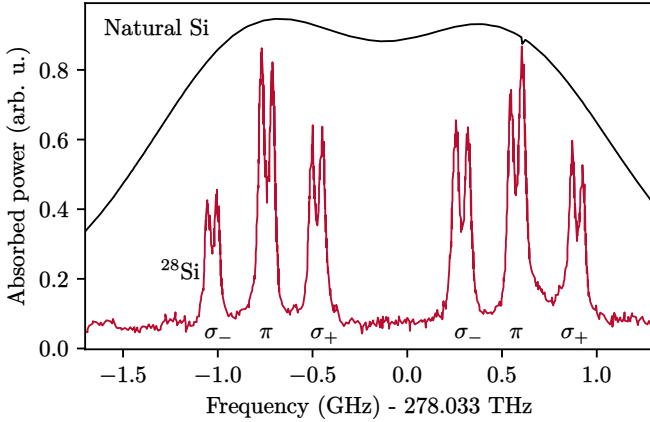


Figure 12: A resonant absorption experiment on an Avogadro-type $^{28}\text{Si}:\text{P}$ sample reveals the twelve dipole-allowed transitions $D^0 \rightarrow D^0X$. The FWHM for this p-type sample is around 30 MHz. The natural Si spectrum is highly broadened and only shows the electron fine structure. From Ref. [43].

citon, but the degeneracy may be lifted by biaxial strain or a static electric field [41]. The wave function of the D^0X heavy hole is not isotropic, but has an angular dependence [19], leading to a different linear slope of the $m_j = \pm\frac{1}{2}$ versus the $m_j = \pm\frac{3}{2}$ and therefore to different g-factors. When the magnetic field points in the [001] crystal direction, the values of the g-factors are $g_{1/2}^h \approx 0.86$ and $g_{3/2}^h \approx 1.33$ [19]. Figure 11 shows the magnetic field dependence of the D^0X fine structure, including the difference in g-factors which can be seen by the different slopes of the black and red lines in the upper part. While donor-bound excitons in direct semiconductors such as GaAs recombine very quickly via radiative recombination on the order of ≈ 1 ns, the phosphorus donor-bound excitons in silicon mainly recombine nonradiatively via the Auger mechanism with a lifetime of ≈ 0.3 μs [42].

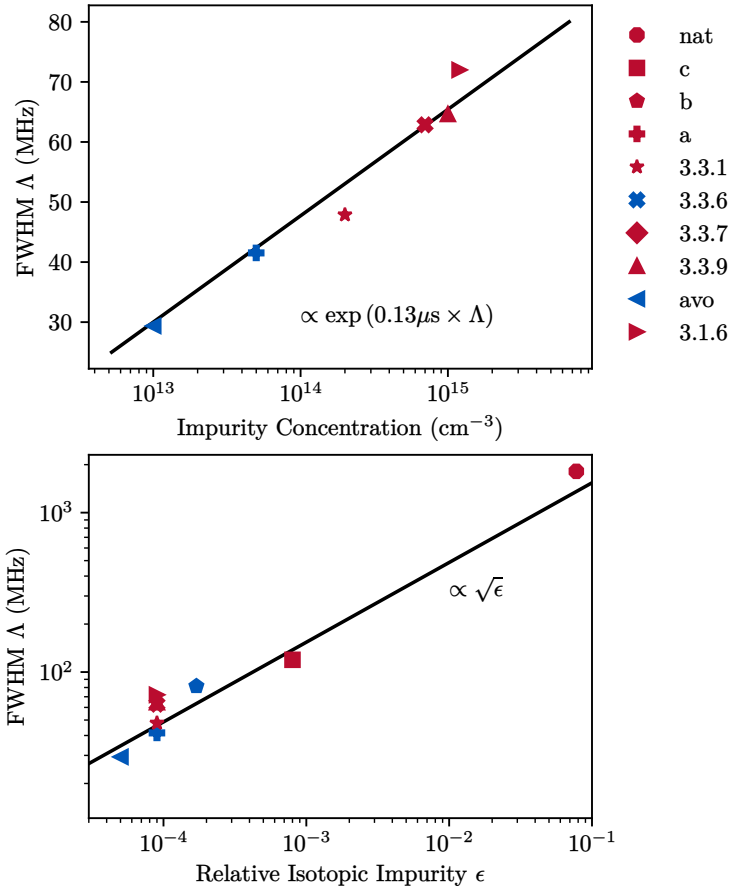


Figure 13: The width of the absorption lines in samples of different isotopic and phosphorus or boron impurities. Blue colored markers represent p-type while the red markers represent n-type samples. The data is extracted using fits of spectra from Thewalt's group, contained in the thesis of Yang [44] with sample specifications listed in Tab. 3. The black lines show the approximate scaling of the widths Δ .

5.3 D^0X ABSORPTION SPECTRUM

While the four D^0 energy levels and four D^0X energy levels would possibly allow for sixteen NIR transitions, only twelve of them are electric-dipole allowed. Figure 11 marks the allowed one-photon transitions as vertical arrows. Depending on the difference in angular momentum, the absorption responds to either linearly polarized ($m = 0$) or circularly polarized ($m = \pm 1$) light. The allowed one-photon transitions have an angular momentum difference of -1, 0, or 1, and are numbered in ascending order according to their energy difference. Because the exact energy of the $D^0 \rightarrow D^0X$ transition can spatially vary due to different Si isotopes and other impurity atoms present in the crystal, the linewidth of the donor-bound exciton transition strongly depends on the sample refinement. However, as Fig. 12 shows, the twelve lines can be well resolved spectroscopically for the purest ^{28}Si samples via resonant laser absorption measurements. Figure 13 shows the linewidths for the ^{28}Si samples doped with phosphorus (n-type) or boron (p-type) for different levels of enrichment. In this work, the ^{28}Si :P sample 3.1.6 is used, which has a relatively high doping concentration and, therefore, a greater linewidth. The sample comes from a batch of Avogadro material that contains 99.995 % ^{28}Si atoms and was doped with phosphorus by the *Leibniz-Institut für Kristallzüchtung* in Berlin (See Tab. 3). Unsurprisingly, the Avogadro ^{28}Si sample with an impurity concentration of less than 10^{13} cm^{-3} [21] shows the narrowest transition linewidth.

The linewidth has an overall lower bound, which is called the natural linewidth. The natural linewidth originates from the quantum mechanical energy-time uncertainty:

$$\Delta E \cdot \Delta t \geq \frac{\hbar}{2}, \quad (14)$$

$$\Delta f_{\text{nat}} = \frac{1}{2\pi\tau}. \quad (15)$$

The lower bound for the linewidth is therefore ≈ 0.5 MHz according to the measured D^0X lifetime of $\tau = 0.3 \mu\text{s}$. The linewidths in Fig. 13 are much larger than the fundamental limit, which is due to the inhomogeneous broadening via impurity atoms that create a

spatial distribution of transition frequencies. Extrapolation of the data in Fig. 13 to the lowest impurity concentrations yields the estimated values required to achieve the fundamental limit, which is a residual $^{29,30}\text{Si}$ concentration of 10^{-8} and an acceptor/donor concentration of $2 \times 10^{11} \text{ cm}^{-3}$. Although these values are impossible to achieve with current technology, there is another technique to circumvent inhomogeneous broadening, which is spectral hole burning. In principle, this technique should yield the natural linewidth, but even spectral holes were observed to possess linewidths that are broadened to roughly four times the natural linewidth [45]. The mechanism of the broadening itself is not yet well understood. An unusual property of the inhomogeneously broadened ensemble is the nearly Lorentzian lineshape. In contrast to the observations, a random spatial distribution of donor frequencies is expected to result in a Gaussian lineshape. Although there are known mechanisms based on donor-donor interactions, such as instantaneous diffusion, which can lead to Lorentzian frequency distributions [46], the context of this or other mechanisms and optical spectroscopy is not discussed in the known literature.

5.4 SPIN RELAXATION AND DEPHASING

Relaxation and dephasing of a spin ensemble are traditionally defined within the framework of the Bloch-Torrey equations [47]:

$$\frac{d}{dt}M_x = \gamma(M_y B_z - M_z B_y) - \frac{M_x}{T_2} \quad (16)$$

$$\frac{d}{dt}M_y = \gamma(M_z B_x - M_x B_z) - \frac{M_y}{T_2} \quad (17)$$

$$\frac{d}{dt}M_z = \gamma(M_x B_y - M_y B_x) - \frac{M_z - M_z^0}{T_1} \quad (18)$$

$$\vec{B}(t) = \{B_x(t), B_y(t), B_z\}. \quad (19)$$

Here, \vec{M} is the average magnetization of the spin ensemble, $\vec{B}(t)$ is the time-dependent external magnetic field with a static longitudinal component, M_z^0 is the static magnetization in thermal equilibrium, and γ is the gyromagnetic ratio. Spin diffusion can

be neglected for donor-bound electrons because they are localized spins.

The T_1 time is denoted as the longitudinal spin relaxation time. The spin relaxation time measures the duration required to establish a thermal equilibrium of the spin population with the lattice. Spin-lattice relaxation involves transfer of energy to and from the lattice, which usually occurs via phonons. The T_2 time is denoted as the transverse spin-spin coherence time. Spins in the x, y plane precess around the static magnetic field vector with a frequency given by $B_z\gamma$. The spin coherence time is the period over which the precessing spins lose their phase relation to each other irreversibly. While there is no general relation between the T_1 and the T_2 time, the inequality $T_2 \leq 2T_1$ generally holds [47]. Consequently, the T_1 time represents a fundamental limit for the coherence time which is a crucial parameter for quantum computation as it defines an upper time boundary over which the qubits can be manipulated without significant loss of information.

Very often, the T_1 time cannot be significantly improved in a given solid-state system because it is limited by phonon interactions of which the likelihood essentially depends only on the temperature. This is in contrast to the T_2 time, which can be dependent on small magnetic field fluctuations induced by strain or other factors that strongly depend on device engineering. For this reason, it is important to look at the spin relaxation time T_1 in detail, as it represents an important physical parameter that quantifies the latent performance of the device.

5.5 D⁰ SPIN-LATTICE RELAXATION

Electrons bound to shallow donors were reported to have very long spin relaxation times more than 60 years ago [18]. The spin relaxation time was found to be independent of the donor density for concentrations below 10^{16} cm^{-3} and to rapidly shorten for higher concentrations. There are three relevant processes involved in the spin relaxation of the donor-electron nucleus system. Figure 14 shows the electron spin relaxation time T_1^e , the nuclear spin relaxation time T_1^n and the cross-relaxation time T_1^x . The cross-relaxation mechanism involves a simultaneous spin flip of the elec-

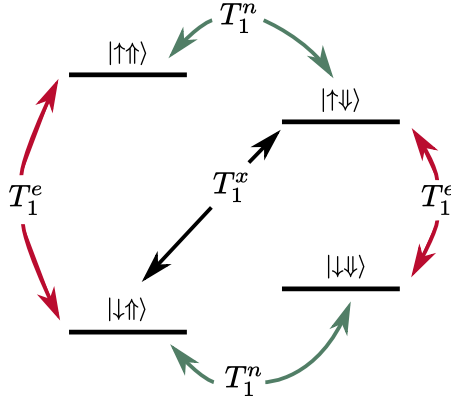


Figure 14: A flow diagram of the spin relaxation paths for donors in a magnetic field according to Ref. [18]. T_1^e , T_1^n and T_1^x are the electron, nuclear and cross-relaxation times, respectively.

tron and the nucleus, with a relaxation time that is long compared to the electron spin relaxation T_1^e . The nuclear spin relaxation time T_1^n is only established as a lower bound of 10 hours [18], but is likely much longer. The electron spin relaxation time T_1^e has arguably received the most attention in existing experiments, but the theory is still ambiguous regarding the exact mechanisms involved at low temperatures. An empirical formula describing the temperature dependence of electron spin relaxation below the Debye temperature of silicon (≈ 645 K) and in the low donor concentration regime was proposed 80 years ago by Castner *et al.* [24]:

$$\frac{1}{T_1^e} = \bar{A}B^4T + \bar{B}B^2T^7 + \bar{C}T^9 + \bar{D}T^{13} + \bar{E}(B)e^{-\Delta/(k_B T)}. \quad (20)$$

Here, T is the lattice temperature, H is the static external magnetic field, $\Delta/k_B \approx 123$ K is the energy splitting between the A_1 donor ground state and the T_2 excited state (see Fig. 9), and \bar{A} , \bar{B} , \bar{C} , \bar{D} , $\bar{E}(B)$ are empirical coefficients. Several sources describe theoretical interactions that result in terms of given powers in temperature, including magnetic field dependencies, but fail to predict the observed empiric coefficients [48–53]. The B^4T term origi-

nates from a single phonon absorption process in which the phonon energy matches the energy difference of the electron spin states $E_{\text{phonon}} \approx \gamma_e H$ [50]. The $B^2 T^7$ comes from an anisotropic Zeeman interaction [53]. The T^9 originates from spin-orbit interaction [50]. The T^{13} only exists under the assumption of dilatational deformations and is negligible in ²⁸Si:P [48]. Finally, the exponential term originates from an Orbach-type interaction [50]. The Orbach mechanism can be understood by considering the T_2 excited electron state as a mixed spin state from where the electron may relax to the ground state with either spin orientation under equal probability. The probability of the electron to be excited is given by the Boltzmann distribution, and therefore it can be easily seen that $T_1^{-1} \propto \exp(-\Delta/(k_B T))$.

5.6 D⁰ SPIN-SPIN RELAXATION

Long spin coherence times of donor-bound electrons in ²⁸Si:P have prompted interest in donor electrons as quantum bits. In natural silicon, the ²⁹Si isotopes with nonzero nuclear spin drive the decoherence of electron spins due to spectral diffusion. Spectral diffusion occurs via random magnetic field fluctuations caused by the ²⁹Si nuclear spins resulting in spin coherence times $T_2 \approx 1$ ms that are many magnitudes below the limit of the spin relaxation time $T_2 \leq 2T_1$. In ²⁸Si:P samples, random magnetic field fluctuations are absent, and the main decoherence mechanism becomes the dipolar interaction between the donor spins [5].

Even at a very low concentration of donors, the interaction between the electron spins cannot be neglected. If a microwave pulse is used to drive spin rotations in an experiment to coherently manipulate and measure spins, a small number of spins are excited by the microwave field, leading to spin flips. The spin flips change the local magnetic field and, therefore, the resonance frequency distribution of the total spin ensemble. This effect is called instantaneous spin diffusion of magnetization [46] because in most cases the pulse duration is negligible compared to the spin relaxation time. The instantaneous diffusion mechanism causes the spin echo in a two-pulse experiment to diminish for increasingly longer pulse durations and thus increases the measured spin decoherence rate

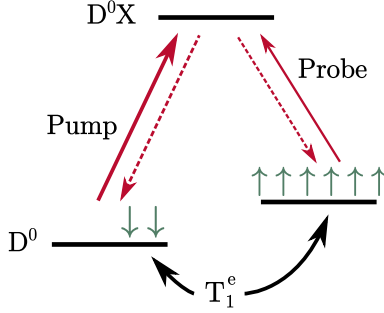


Figure 15: Optical pumping in a three-level system. The green arrows represent the donor electron spins.

[54]. The optimal pulse duration with a maximum spin echo amplitude in a two-pulse experiment corresponds to a rotation of 180° which reduces the spin coherence to 20 ms by instantaneous diffusion [5]. Measuring the intrinsic spin coherence time would require infinitely small rotation angles, leading to vanishing spin echo amplitudes. However, the spin relaxation time can be extrapolated from longer pulses to a pulse length of zero to extract the intrinsic coherence time. According to Ref. [54] the instantaneous diffusion relaxation time T_2' in a two pulse echo experiment is

$$T_2' \propto \sin(\theta^2/2), \quad (21)$$

where θ is the pulse rotation angle and can be easily extrapolated using linear regression. Using this technique, an intrinsic spin coherence time of 10 s is obtained for $^{28}\text{Si:P}$ with a phosphorus doping concentration of 10^{14} cm^{-3} [5].

5.7 THREE LEVEL SYSTEM AND OPTICAL PUMPING

While resonant RF pulses create coherent superpositions of the ground states, optical pumping can move ground state populations away from thermal equilibrium [55]. Thus, it is possible to change the magnitude of spin magnetization, or equivalently spin polarization, only by optical pumping. Figure 15 shows a simplified sketch of the donor-bound electron with a fine structure splitting of $g\mu_B B$

in an external magnetic field. The nuclear spin of phosphorus and the fine structure of the excited state are neglected for simplicity, resulting in an effective three-level system. Resonant pulsed microwave excitation ultimately must depend on the thermal equilibrium spin polarization to measure the spin dynamics. In thermal equilibrium, the ground state polarization of the ensemble is given by

$$\rho = \frac{N_{\uparrow} - N_{\downarrow}}{N_{\uparrow} + N_{\downarrow}} = 1 - \frac{2}{1 + \exp \frac{\gamma_e B}{k_B T}}, \quad (22)$$

where N is the population of spins in the up or down state, γ_e is the electron gyromagnetic ratio, T is the lattice temperature, and B is the static external magnetic field. In a typical ESR experiment [5] where $B \approx 350$ mT and $T = 2$ K the equilibrium spin polarization amounts only to approximately 12 %.

Efficient optical pumping is based on the fact that the D^0X hole spin relaxes very quickly. Because the hole spins relax within the lifetime of the donor-bound exciton, electron spin orientations are randomized after the exciton recombines. By utilizing a high-power pump laser, it is therefore possible to move the population from one electron spin state to the other very effectively. When the pump laser is turned on, increased absorption of the probe laser can therefore be observed for the transition with opposite electron spin.

In contrast to the thermal equilibrium polarization in Eq. 22, the steady state spin polarization induced by resonant optical pumping depends on the ratio of the pump rate p to the spin relaxation rate $\Gamma_s = 1/T_1^e$

$$\rho = \frac{1}{1 + 4 \frac{\Gamma_s}{p}}. \quad (23)$$

For the case of donors in silicon, pump rates of $p \gg \Gamma_s$ are easily achievable and spin polarizations very close to unity can be obtained almost independently of temperature and magnetic field. In an actual experiment, the D^0X spin polarization cannot approach 100 % for higher pump rates, because the conduction electrons created by the Auger decay of the D^0X have high excess energy and

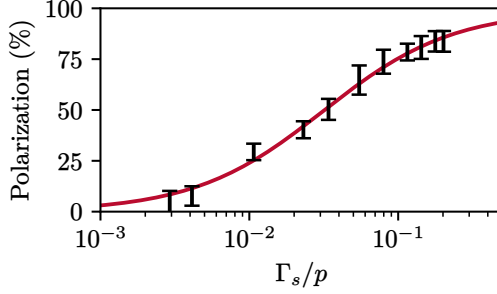


Figure 16: The measured donor electron spin polarization as a function of the quotient of the spin relaxation time and pump rate. The black error bars are experimental values and the red line represents a fit for the pump rate coefficient using Eq. 23.

cause some of the D^0 electron spins to relax [56]. Optical pumping and probing of spins is the main technique used in this work to measure the spin-lattice relaxation times to a high degree of accuracy. Independent of the external magnetic field and temperature, the experimental spin polarizations achieved are well above 80%.

Part III

SETUP AND METHODS

OVERVIEW

Many parts in the given setup need to work in a controlled way in order to collect the data necessary to provide reliable statements about the dynamics of spin polarization or bandgap changes. Various parameters such as environmental temperature and optical frequencies need to be controlled. The procedures for each experiment are very complex and involve fast, reliable, and synchronous execution of dozens of individual devices. Precisely probing the frequency spectrum and absorption amplitude of the bound exciton transitions requires exact and fast control over laser frequencies with minimal external perturbation. The unique methods used to implement these requirements are broken down and discussed in the following sections. The discussion begins with the general layout of the cryogenic optical absorption experiments and further delves into the details for additional requirements of high-precision spectroscopy.

The aim of this work is to precisely measure the energy gap of Si, to determine the spin-lattice relaxation times of donor electrons, and to detect and create persistent spectral holes in the spectrally broadened donor-bound exciton transition. Each aim requires an individually optimized setup, but some concepts such as phase modulation absorption spectroscopy and lock-in detection are common to all setups and are covered in the following sections in detail. The sections in question may serve as a reference on how to achieve optimal performance with the given setup and are supposed to provide insight into the specific parameters chosen to perform the experiments here. The details relating to each experiment are individually discussed in Part IV of this thesis.

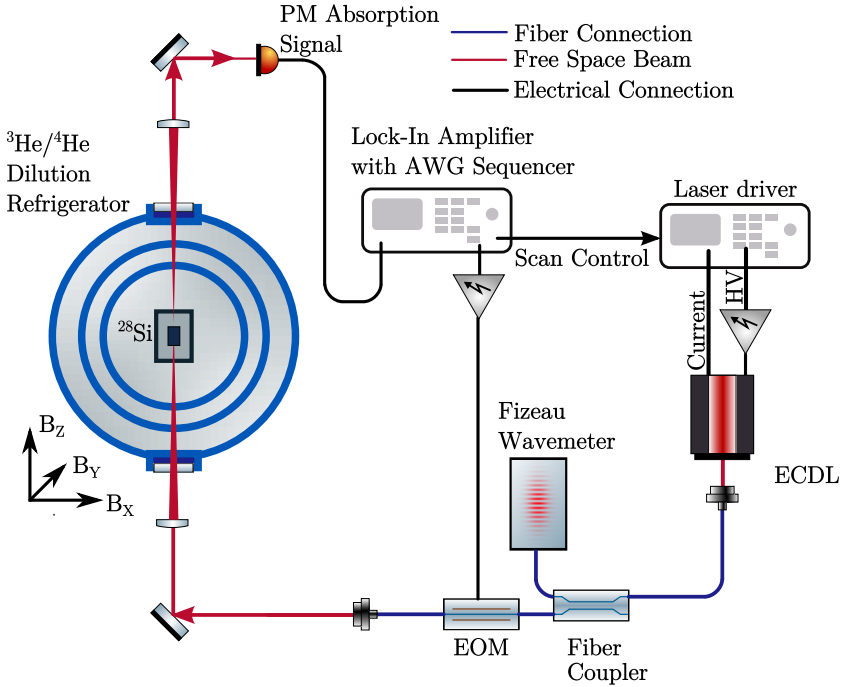


Figure 17: The setup for laser spectroscopy of the donor-bound exciton transition in $^{28}\text{Si:P}$ at very low temperatures. The arbitrary waveform generator (AWG) and lock-in detector work uniformly to produce the absorption signal which is evaluated on a computer. The laser frequency is controlled by the AWG using the laser driver modulation input and measured using a Fizeau wavelength meter via a fiber-coupled input. The very low sample temperature of 35 mK is provided by the high-performance dilution refrigerator including optical access and vector magnets for arbitrary magnetic field directions.

6.1 SETUP AND METHODS

Resonant laser absorption spectroscopy probes the absorption spectrum of a sample in order to quantitatively assess the concentration of certain species. The species investigated in this thesis is the donor spin complex¹ in $^{28}\text{Si:P}$, which has unique and fascinating spectral properties and, consequently, poses unique demands on the spectroscopy setup. The foundation of resonant laser absorption spectroscopy are a tunable laser and a photodetector which monitor the frequency- and time-dependent absorption. Figure 17 shows the basic experimental configuration used in this work to detect the D^0X absorption spectrum in $^{28}\text{Si:P}$. The setup consists of a tunable external cavity diode laser source (ECDL), an optically accessible cryostat with superconducting vector magnets for low temperatures of 35 mK and high static magnetic fields up to 1.2 T, as well as photodetectors and fiber-based modulators for low noise measurements. The ECDL output wavelength (see Sect. 8.1) is controlled by adjusting the high-voltage and current control outputs of the laser driver. The wavelength is measured with a Fizeau-type wavelength meter (see Sect. 8.4) in order to obtain the frequency-dependent laser absorption spectrum. Because the amount of light absorbed by the $2 \times 4 \times 0.8\text{mm}$ $^{28}\text{Si:P}$ sample is very low (only about 0.5%), a sophisticated method to recover the laser absorption signal is required. Signal recovery is achieved here via optical phase modulation and demodulation with a high-performance lock-in amplifier (see Chap. 7). The unique setup in combination with sensitive detection techniques allows to obtain information that is usually difficult to access by conventional cryogenic spin-resonance setups [24]. For example, limited to no information on the donor electron spin relaxation or the dependence of the energy gap at temperatures below 1 K for varying magnetic fields was available to date. Precise measurements in this regime are very challenging even with the setup described here because of the difficulty in maintaining a low sample temperature under simultaneous heating by the laser absorption. Efficient cooling of the sample at very low temperatures is provided by a specially designed sample insert con-

¹ Only the relative concentration of spins with certain orientation is assessed here in order to obtain the spin polarization.

nected to the cold plate of a $^3\text{He}/^4\text{He}$ dilution refrigerator, which is discussed in the next chapter.

6.2 CRYOGENICS

Experiments on donor-bound exciton transitions in $^{28}\text{Si:P}$ require cryogenic temperatures $T \lesssim 20\text{K}$ due to the low excitation energies of donor-bound excitons [40]. Even lower sample temperatures are desired to accurately measure the spin dynamics and the energy gap over a wide temperature range and to detect very long relaxation times. The cryostat used in all experiments is an *Oxford Triton 400* dry² dilution refrigerator. The cryostat provides a base temperature of 35 mK including optical access and continuous operation over months, which is crucial for long-term measurements. Static magnetic fields up to 1.2 T can be applied in all spatial dimensions to investigate the donor spins in the sample by a vector magnet. Performing experiments with this cryostat requires a non-magnetic sample insert which can benefit optimally from the low base temperatures. The specially designed sample insert is discussed below.

6.3 SAMPLE INSERT

Cooling the $^{28}\text{Si:P}$ sample below liquid helium temperatures efficiently poses a very challenging task. The Kapitza resistance quantifies the heat flow that occurs at the interface between the sample and liquid helium in a simple immersion bath. Kapitza heat flow is known to be very efficient and to scale well with higher temperatures [57]. Although it is potentially possible to liquify a large amount of helium inside a dilution refrigerator and cool it below the boiling point of ^4He using the cryogenic cold plate, this method is difficult to implement and requires a continuous supply of external helium due to the volatility of the superfluid phase. Another option to cool the sample is applying high contact pressure to the cold plate of the dilution refrigerator [58]. When high contact pressure is applied, there is significant contact heat flow between the

² Dry means that there is no external supply of liquid helium.

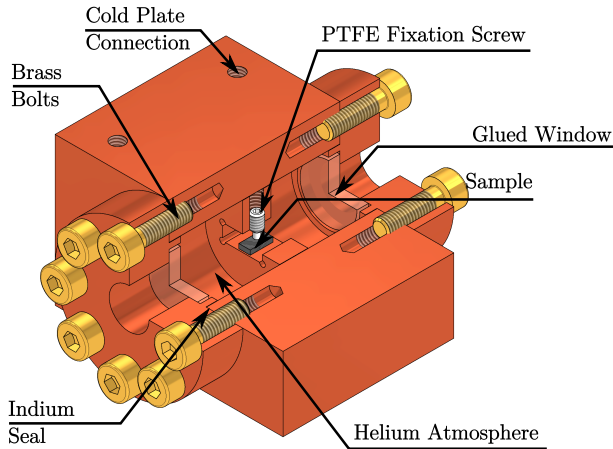


Figure 18: A three-quarter section of the sample insert for low-temperature measurements. This drawing is not to scale.

sample surface and the cold plate surface. However, the contact pressure also leads to strain in the sample, which is undesirable as it disturbs the experiment. A different option is to use thermal bonding material that provides low thermal resistance, supports very low temperatures, and does not contaminate the sample or cause strain. Unfortunately, no suitable bonding material is known that matches the unique requirements here.

Instead, efficient thermal interfacing of the sample is achieved by using a low-pressure helium exchange gas inside a hermetically sealed sample insert. Figure 18 shows the specially designed cryogenic insert. Beryllium copper is chosen as the base material because it has high strength and thermal conductivity, and is at the same time nonmagnetic and excellently machinable. Optical access is provided by windows made from an N-BK7 substrate with a broadband antireflection coating at a design wavelength of 1064 nm. The windows are glued with epoxy resin³ to a compressing ring with tightly spaced holes for high pressure bolted connections. Sealing the insert is performed by compressing indium

³ *Loctite Stycast 2850FT* is mixed with 24LV catalyst, air bubbles are removed using a vacuum container and curing is performed at an elevated temperature.

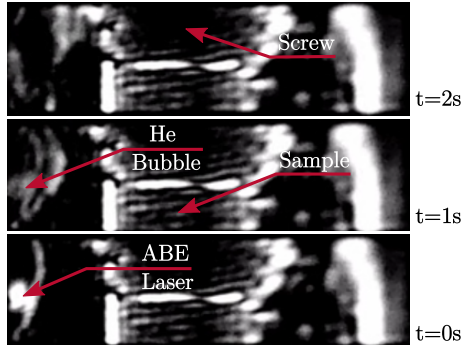


Figure 19: A schlieren image of the $^{28}\text{Si:P}$ sample inside the insert obtained by illumination with laser light from the back. A second high-power laser is focused onto the edge of the sample insert to vaporize the superfluid helium and create a bubble. The bubble is visible on the left side and continuously expands and pops again.

inside the spherical outer edge between the insert and the compressing ring. The compressing bolts are made from brass, which has a higher thermal contraction than beryllium copper, causing the compression to increase at lower temperatures. The sample is loosely fixed inside the insert using a PTFE fixation screw that contracts stronger than beryllium copper and consequently keeps strain at low temperatures to a minimum. Connecting the insert to the cold plate can be done using bolted connections at the top.

The creation of an effective seal for the very volatile superfluid helium is the most critical part of constructing the sample insert. The parts need to be cleaned in an isopropyl ultrasonic bath before the windows are glued and the indium compressing seal is created. Fortunately, the design of the insert requires the windows to be glued only once, and the sample can be exchanged by opening one of the compressing rings and closing them again under a helium atmosphere. The sample and components of the insert are inserted into a *glove bag* that is then sealed and flushed several times to create a perfect helium atmosphere. One way to verify a successful seal is by measuring the temperature-dependent D^0X absorption spectrum under laser irradiation with increased powers. Another way is to directly probe the helium content of the sample insert using

schlieren imaging, as shown in Fig. 19. The slight refractive index change in liquid helium causes intensity changes in the schlieren image that can be detected by a camera. It is even possible to create expanding superfluid helium bubbles in the sample insert by local heating with a focussed laser beam. The oscillating behavior of the bubble impressively demonstrates the creeping film flow and the vanishing viscosity of superfluid helium.

SIGNAL RECOVERY

Performing laser spectroscopy of the donor-bound exciton transition is challenging due to the low absorption coefficient of the sample. The low absorption coefficient is necessary because a low donor concentration reduces undesired donor-donor interactions. Hence, a sophisticated method is needed to recover the small laser absorption signal from the background noise. Phase modulation spectroscopy in combination with lock-in amplification provides an excellent way to reduce background noise and allows for precise measurements of the donor-bound exciton transition. The following sections discuss the principles of laser absorption spectroscopy in general and explain the methodology of phase modulation absorption spectroscopy as well as lock-in amplification.

7.1 ABSORPTION SPECTROSCOPY

When a coherent planar light wave propagating in z -direction enters a linear optical medium¹, the electric field transmitted through the medium can be expressed as the real part of a complex-valued electric field function

$$E(z, t) = \Re \left(E_0 e^{i(kz - \omega t)} \right), \quad (24)$$

where k is the wave vector of the light, ω is the angular frequency, $|E_0|$ is the amplitude of the wave entering the material, and $k(\omega)$ is a complex parameter depending on the medium. For a linearly absorbing medium, the wave number can be written as

$$k = (n + i\kappa) \frac{\omega}{c}, \quad (25)$$

¹ Examples of non-linear optical media include strongly birefringent crystals, magneto-optic materials, and meta-materials.

where $n(\omega)$ is the linear refractive index of the material and $\kappa(\omega)$ is called the extinction coefficient. Inserting Eq. 25 into Eq. 24 results in the following expression for the electric field:

$$E(z, t) = e^{-\kappa\omega z/c} \Re \left(E_0 e^{i(\omega n z/c - \omega t)} \right). \quad (26)$$

When detecting the photocurrent with a photodetector, not the electric field amplitudes but only the power arriving at the detector is relevant. Taking the absolute square gives the optical power which is proportional to the photocurrent:

$$|E(z)|^2 = |E_0|^2 \exp(-2\kappa\omega z/c) \equiv |E_0|^2 \exp(-\alpha z). \quad (27)$$

The absorption coefficient is defined as $\alpha = \frac{4\pi\omega}{c}$ and is frequently used to describe the amount of power absorbed per distance under light transmission at a given frequency². Equation 27 directly relates the detected photocurrent to the optical absorption coefficient, which is the basic working principle of laser absorption spectroscopy. Some results of absorption measurements on Si are discussed in the next section.

7.2 OPTICAL ABSORPTION SPECTRA IN SI

While the band-to-band absorption coefficient exceeds 10^3 cm^{-1} easily in Si, donor-bound exciton absorption in the sample under investigation³ is comparatively low. The absorption coefficient for the 3.1.6 sample is determined at resonance as $\alpha \approx 1.4 \times 10^{-2} \text{ cm}^{-1}$, which is in good agreement with existing measurements [59]. Figure 20 compares band-to-band absorption with resonant D⁰X absorption in the investigated sample. Band-to-band absorption approximately scales with the square root of the photon energy, which is due to the parabolic band edges [15]. The onset of band-to-band absorption follows the temperature dependence of the energy gap and the phonon energy distribution in Si. Although band-to-band absorption is negligible at low temperatures for the D⁰X transition frequency, room temperature absorption is relatively high, which

² See also the Beer-Lambert law for reference.

³ The sample has a donor concentration of $1.2 \times 10^{15} \text{ cm}^{-3}$.

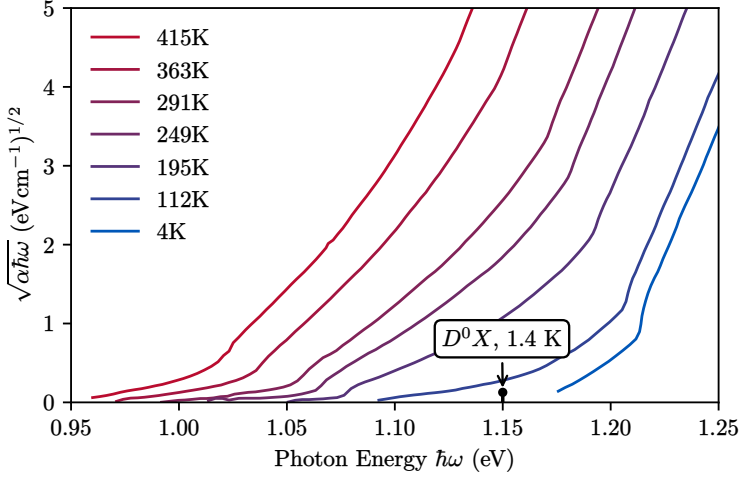


Figure 20: Band-to-band absorption in Si at different temperatures.

The black dot represents the zero phonon line of the donor-bound exciton absorption at 1.4 K in the 3.1.6 sample under investigation. The band-to-band absorption data is taken from Ref. [60].

is important for the utilization of Si photodetectors or Si-based integrated photonic devices in experiments involving the D^0X transitions. In comparison to strong band-to-band absorption, donor-bound exciton absorption is significantly weaker but also much sharper in frequency. Figure 20 shows why the use of band-to-band absorption in Si is suboptimal for detecting the temperature-dependent bandgap. The indirect nature of the bandgap in combination with the phonon distribution causes a severe broadening of the onset of absorption, which leads to high measurement uncertainty. Instead, the energetically narrow D^0X transitions are used to precisely determine the temperature dependence of the bandgap.

A quantitative description of the energetically very sharp $D^0 \rightarrow D^0X$ absorption can be obtained by considering an electric dipole oscillator model. Within the dipole approximation, a charge q oscillates in response to an alternating electric field with frequency ω . The cumulative response of the electric dipoles in the sample to

the alternating field influences the relative absorption and refractive index according to [61]

$$\kappa = \frac{Nq^2}{8\varepsilon_0 m \omega_0} \frac{\gamma}{(\omega_0 - \omega)^2 + (\gamma/2)^2} \quad (28)$$

$$n = 1 + \frac{Nq^2}{4\varepsilon_0 m \omega_0} \frac{\omega_0 - \omega}{(\omega_0 - \omega)^2 + (\gamma/2)^2}. \quad (29)$$

Here, N is the number of oscillators (donor electrons), m is the dipole mass, γ is the absorption linewidth (FWHM), and ω_0 is the resonance frequency of the dipole oscillator. The photon energy is $\hbar\omega_0 \approx 1.150$ eV for the zero phonon line of the donor-bound exciton transition. In practice, the frequency distribution of $D^0 \rightarrow D^0X$ absorption is well described by Eq. 29. The natural linewidth (≈ 0.5 MHz) in the given sample is not observed in direct absorption as a result of the inhomogeneous broadening of the ensemble. Nevertheless, the frequency-dependent extinction coefficient and refractive index from Eq. 29 are used to model the phase modulated absorption spectrum. Figure 21 shows the measured zero-field D^0X absorption spectrum, which displays a multitude of distinct resonances. The two leftmost lines (singlet state and triplet state, respectively) originate from the hyperfine splitting $A = 117$ MHz and the third line (*) is likely a shifted duplicate of the hyperfine spectrum due to random local fields⁴.

While it is possible to directly detect the energetically sharp D^0X transition simply by acquiring the DC absorption signal of a tunable diode laser via a photodetector according to Eq. 27, this technique is subject to a significant amount of background noise. The next section discusses a low-noise method that is ideally suited to recover the D^0X absorption spectrum for the sample under investigation.

⁴ A similar splitting is described in Refs. [44, 62] with different sample-dependent values.

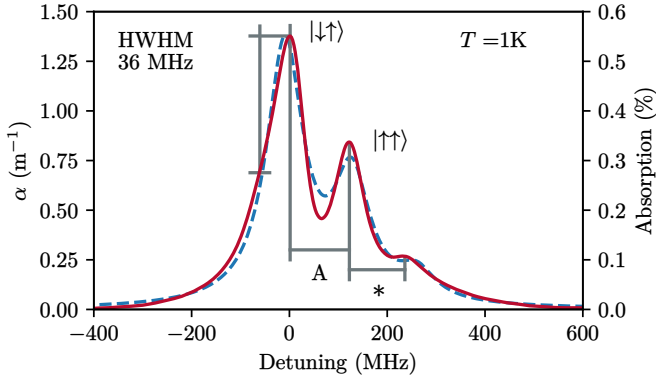


Figure 21: The zero field no-phonon absorption spectrum of the donor-bound exciton in the sample under investigation. $A = 117.53$ MHz is the hyperfine splitting and the asterisk * marks a sample-dependent splitting due to random field fluctuations [62].

7.3 PHASE MODULATION ABSORPTION SPECTROSCOPY

The background noise of DC laser absorption experiments can be circumvented by detecting the heterodyne⁵ beat signal that occurs when the phase modulated (PM) optical spectrum of the probe laser is distorted by the spectral feature of interest. Calculating the relationship between a PM absorption spectrum and a regular absorption spectrum requires knowledge of the phase modulated electric field amplitudes. Phase modulation of a carrier field with frequency ω_0 can be described in terms of complex functions as

$$E_{\text{PM}}(t) = E_0 \exp [i(\omega_0 t + a \sin(\omega_m t + \varphi_m))], \quad (30)$$

where ω_m is the phase modulation frequency, a is the so-called modulation index, and φ_m is the phase modulation offset. The

⁵ Heterodyne methods, in contrast to homodyne methods, utilize multiple carrier frequencies to generate the desired signal.

electric field in Eq. 30 can be redefined in terms of Bessel functions of the first kind J_n via the Jacobi-Anger identity [63]:

$$E_{\text{PM}}(t) = E_0 \exp(i\omega_0 t) \sum_{n=-\infty}^{\infty} J_n(a) \exp(in(\omega_m t + \varphi_m)). \quad (31)$$

From Eq. 31, it becomes apparent that the phase modulated electric field has multiple frequency components $\{\dots, \omega_0 - 2\omega_m, \omega_0 - \omega_m, \omega_0, \omega_0 + \omega_m, \omega_0 + 2\omega_m, \dots\}$, each offset by integer multiples of the modulation frequency. The sidebands of order n have frequencies $\omega_0 \pm n\omega_m$ and power $|E_0|^2 J_n(a)^2$. Figure 22 (a) shows two exemplary power spectra of the modulated carrier. While a low modulation index $a = 0.1$ leads to only two visible sidebands, a modulation index of $a = 2$ produces many visible sidebands. The relative sideband power is shown in Fig. 22 (b).

When the phase modulated electric field is transmitted through a medium, the sideband n experiences a phase shift $\phi_n(\omega)$ due to the refractive index and absorption $\delta_n(\omega)$ related to the extinction coefficient. The total transmitted electric field then becomes

$$E_{\text{PM,T}}(t) = E_0 \exp(-\delta_0 - i\phi_0) \exp(i\omega_0 t) \times \sum_{n=-\infty}^{\infty} J_n(a) \exp(-\delta_n - i\phi_n) \exp(in(\omega_m t + \varphi_m)). \quad (32)$$

Again, only the optical power impinging on a photodetector can be measured in the experiment. For the case of weak absorption⁶ it can be assumed that $|\delta_n| \ll 1$ and $|\phi_n| \ll 1$. Furthermore, only the

⁶ The absorption in this work is in all cases less than 0.6 %.

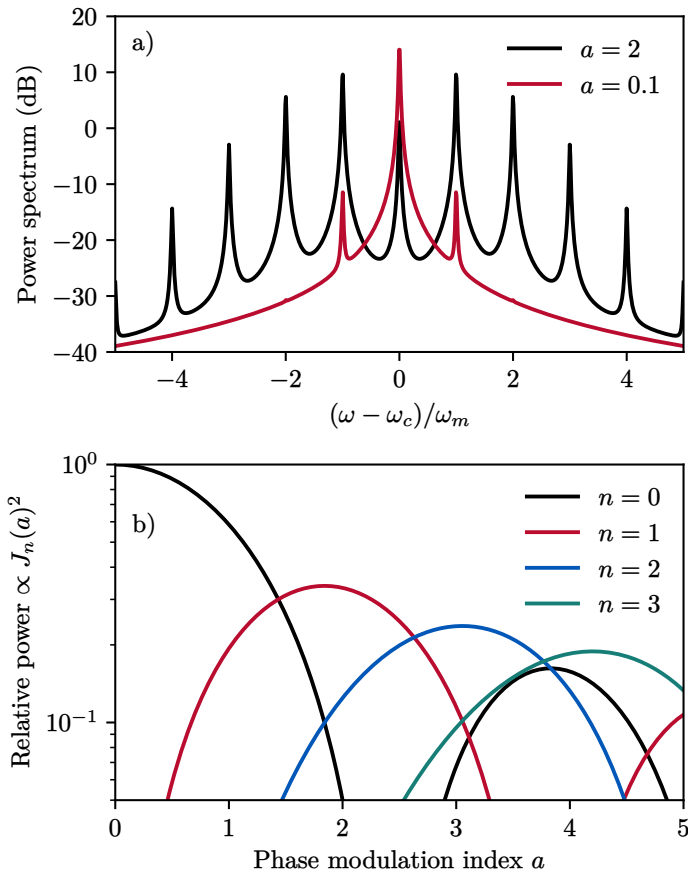


Figure 22: (a) The optical power spectrum for phase modulated light with carrier frequency ω_c and modulation frequency ω_m for high and low modulation depths. (b) The sideband power can be determined using the squared Bessel functions of the first kind.

terms at the phase modulation frequency are kept for simplicity. The detected power can then be approximated as [64]

$$\begin{aligned}
 |E_{\text{PM,T}}|^2 = & |E_0|^2 \exp(-2\delta_0) \times \left[1 \right. \\
 & + 2 \cos(\omega_m t + \varphi_m) \sum_{n=0}^{\infty} J_n(a) J_{n+1}(a) \\
 & \quad \times (\delta_{-n-1} - \delta_{n+1} + \delta_{-n} - \delta_n) \\
 & + 2 \sin(\omega_m t + \varphi_m) \sum_{n=0}^{\infty} J_n(a) J_{n+1}(a) \\
 & \quad \times (\phi_{-n-1} - \phi_{-n} + \phi_{n+1} - \phi_n) \\
 & \left. \right]. \tag{33}
 \end{aligned}$$

Equation 33 contains a DC term that is equivalent to Eq. 27, as well as a cosine term that depends on the difference in absorption δ and a sine term that depends on the difference in phase shift ϕ . The prefactors of the cosine and sine functions are termed the in-phase component (X) and the quadrature component (Y), respectively, and can be conveniently measured using various quadrature demodulation techniques⁷. In an actual setup, the phase shift of the modulation signal leads to a mixing of X and Y, which is explained by a rotation of the 2D coordinates. However, the modulation phase φ_m can be adjusted to compensate for phase shifts and obtain the distinct X and Y components in Eq. 33 as the detected in-phase and quadrature components.

It is useful to discuss some results of quadrature demodulation using the theoretical resonant absorption spectrum for different values of a and ω_m . The theoretical spectrum assumes a Lorentzian distribution with the extinction coefficient and refractive index given by Eq. 29. Figure 23 shows different exemplary PM absorption spectra calculated from the theoretical distribution where γ is equal to the FWHM. Although the signal for small modulation frequencies is mainly contained in the X component, higher modulation frequencies also produce a significant signal in the Y component. Higher modulation indices prove beneficial for the de-

⁷ Probably the most common technique in experiments is lock-in detection.

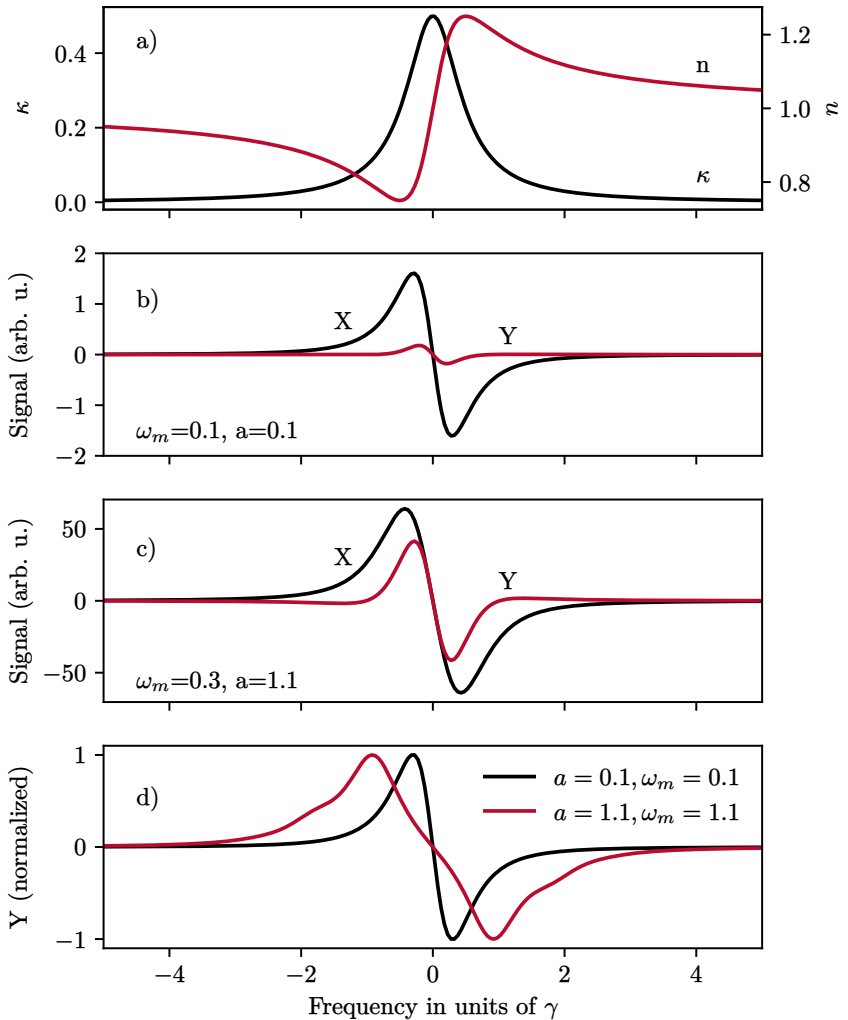


Figure 23: Different PM absorption spectra are calculated from the demodulation of a Lorentzian distribution. (a) Extinction and absorption coefficient according to Eq. 29 with $\gamma = 1$ and every other parameter set to 1. (b) For small modulation frequencies, the X component dominates. (c) Quadrature signals for higher modulation frequency and index yield a much larger signal that roughly scales with $\omega_m \cdot a$. (c) The spectrum obtained from the in-phase quadrature is visibly distorted for high values of the demodulation and index.

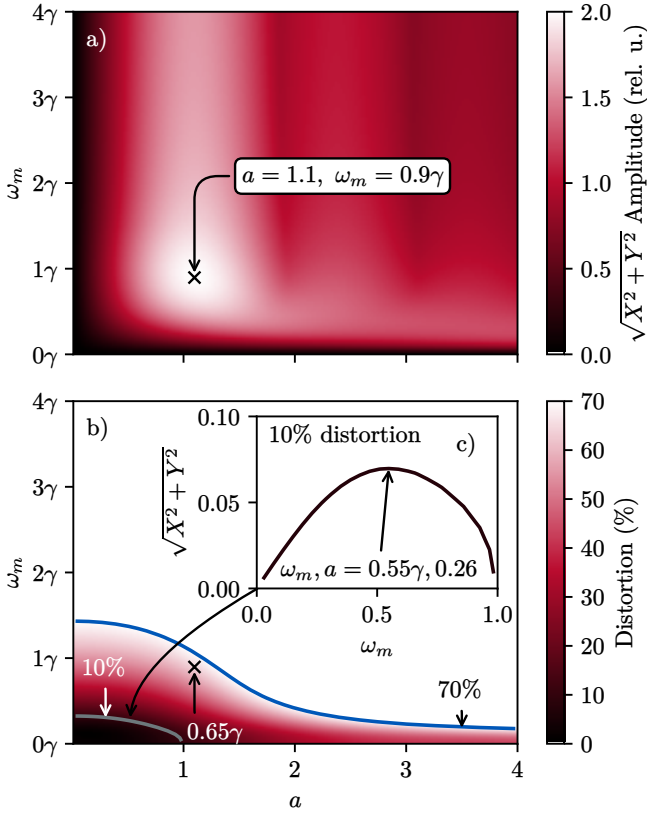


Figure 24: The dependence of the amplitude of the demodulated signal and the spectral distortion on the modulation index a in units of 2π , and modulation frequency ω_m in units of γ . **(a)** The amplitude of the demodulation magnitude is calculated as $R = \sqrt{X^2 + Y^2}$. There exists a global maximum at a PM frequency of 0.9γ and a modulation depth of 1.1 full phase rotations. **(b)** The distortion value is calculated from the standard error between the measured and the ideal spectrum and normalized by the integrated ideal spectrum. The ideal spectrum is multiplied with $\omega_m \cdot a$ to account for amplitude scaling. The grey and blue contours mark areas of low distortion (10%) and high distortion (70%), respectively. The point of maximal demodulation amplitude has a distortion of almost 70% (See Fig. 23 for comparison). **(c)** The inset shows the demodulation amplitude around the contour of low distortion. A value of roughly only 6% of the maximal achievable amplitude can be reached while maintaining low distortion.

modulation signal, but they also lead to a visible distortion of the absorption spectrum which is shown in Fig. 24. This is especially the case in combination with high modulation frequencies. For this reason, it is necessary to carefully consider the choice of modulation parameters for PM absorption spectroscopy experiments. Although for some experiments the larger signal yield is very important, the accurate determination of lineshapes should be performed with lower modulation frequencies $\omega_m \ll \gamma$ and indices $a \ll 1$. For the case of sufficiently low modulation parameters, the demodulated components in Eq. 33 can be further simplified by dropping every sideband except where $n = \pm 1$ [64]

$$\begin{aligned} |E_{PM,T}|^2 \approx E_0^2 \exp(-2\delta_0) \times [1 \\ + a \cos(\omega_m t) \times (\delta_{-1} - \delta_1) \\ + a \sin(\omega_m t) \times (\phi_{-1} + \phi_1 - 2\phi_0)]. \end{aligned} \quad (34)$$

It becomes apparent that the X component in Eq. 34 is proportional to the frequency derivative of the extinction coefficient given the limit $\omega_m \rightarrow 0$. On the other hand, the Y component shows two separate resonances corresponding to the difference in dispersion between the carrier and sidebands. A further assumption can be made that the dispersion differences scale in the same way as the absorption differences⁸ and thus $\phi_{-1} - \phi_0 + \phi_1 - \phi_0 \ll \delta_{-1} - \delta_1$ holds because the difference in dispersion is taken only between adjacent modulation bands. This assumption yields the most simple equation for PM absorption

$$|E_{PM,T}|^2 \approx E_0^2 \exp(-2\delta_0) [1 + a(\delta_{-1} - \delta_1) \cos \omega_m t], \quad (35)$$

where the Y component and, accordingly, the phase shift of the field are neglected via the argument made previously.

Determining the linewidths of optical transitions with high accuracy should be performed using Eq. 35 in, e.g., a spectral hole burning experiment in which very narrow spectral features are investigated. For determining the polarization of donor-bound electrons, a maximal signal amplitude is desired and hence Eq. 33

⁸ This assumption is founded on the Kramers-Kronig relations [65] which directly connect the extinction coefficient κ to the refractive index n .

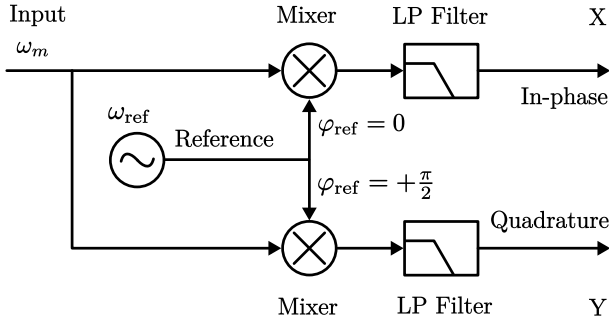


Figure 25: A flow diagram of lock-in detection.

should be used in conjunction with the optimal parameters given in Fig. 24. Regardless of the parameter choice, lock-in amplification yields the optimal signal-to-noise ratio for detecting the in-phase and quadrature components, which is discussed in the next section.

7.4 LOCK-IN AMPLIFICATION

Lock-in amplifiers are capable of extracting signal amplitudes and phases in extremely noisy environments. The lock-in method is based on a homodyne detection scheme combined with low-pass filtering to measure the amplitude and phase of the signal relative to a periodic reference. Because the signal is detected in a very well-defined frequency band around the reference frequency, noise contributions in all other frequency components are efficiently rejected [66].

Figure 25 visualizes the basic working principle of lock-in amplification in a flow diagram. The detector voltage output (proportional to the optical power in Eq. 33) has frequency components at the known modulation frequency ω_m . After splitting the detector output, the voltage is multiplied by two local oscillators, which

are relatively phase shifted by $\pi/2$ and therefore orthogonal. The following time-dependent signal is obtained after multiplication:

$$V_{\text{mix}}(t) = V_{\text{ref}} \sin(\omega_{\text{ref}} + \varphi_{\text{ref}}) \times [\quad (36)$$

$$+ V_X(t) \sin(\omega_m t + \varphi_m)$$

$$+ V_Y(t) \cos(\omega_m t + \varphi_m)]$$

$$= \frac{V_{\text{ref}}}{2} V_X(t) \times [\quad (37)$$

$$+ \cos((\omega_{\text{ref}} - \omega_m) + \varphi_m - \varphi_{\text{ref}})$$

$$- \cos((\omega_{\text{ref}} + \omega_m) + \varphi_m + \varphi_{\text{ref}})]$$

$$+ \frac{V_{\text{ref}}}{2} V_Y(t) \times [\quad (38)$$

$$+ \sin((\omega_{\text{ref}} - \omega_m) + \varphi_m - \varphi_{\text{ref}})$$

$$+ \sin((\omega_{\text{ref}} + \omega_m) + \varphi_m + \varphi_{\text{ref}})], \quad (39)$$

where $V_X(t)$ and $V_Y(t)$ are the time-dependent amplitude signals of the in-phase and quadrature components, respectively. The resulting signal after mixing $V_{\text{mix}}(t)$ has components at the difference and sum between the modulation frequency and the reference frequency. For all purposes in this work, $\omega_m = \omega_{\text{ref}}$ holds and only the phase relation between the reference and modulation signal is of importance⁹. The low pass filter (LP) is chosen in a way that the cutoff frequency is at least a factor ten lower than $2\omega_m$, but high enough to transmit the time-dependent experimental signals $V_X(t)$ and $V_Y(t)$. If the phases are chosen as $\varphi_m - \varphi_{\text{ref}} = 0$, the detected DC signal after low-pass filtering yields the in-phase and quadrature components $V_X(t)$ and $V_Y(t)$ of the PM modulation signal.

The benefits of lock-in detection for low-noise signal recovery can be understood by looking at the modulated signals and filters in frequency space. Figure 26 shows two demodulation bands (dashed blue lines) and experimental signals (red bars) at frequencies ω_1 and ω_2 . The width of the demodulation bands is given

⁹ This relation is equivalent to locking the phase between the modulated signal and the reference signal, which is also the reason for the name “lock-in” amplification. Reference and modulation signals are usually compared in a phase-locked loop (PLL).

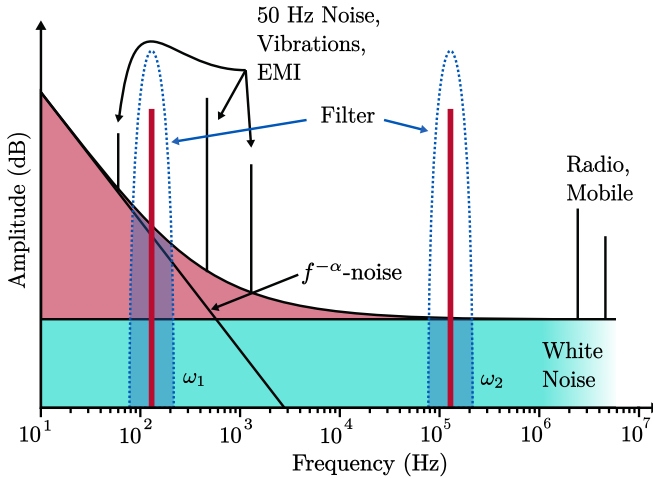


Figure 26: A typical power spectrum that includes the signal and different sources of noise in the experiment. Adapted from Ref. [67].

by the LP cut-off frequency. A high cut-off frequency yields wider bands containing more noise. At lower frequencies, there is an increased noise background scaling with roughly $f^{-\alpha}$ ¹⁰. The noise background also includes various sources of electromagnetic interference (EMI) and acoustic vibrations. There are two main benefits of moving the signal modulation to higher frequencies. The first is the absence of low-frequency interference, such as EMI and $f^{-\alpha}$ noise, which reduces the background to only white noise. Shot noise is an important source of such white noise, which limits the SNR at high laser powers and originates from the particle nature of photons. Another source of white noise is resistance fluctuation caused by finite temperatures of the photodetector, which becomes important at low laser powers. The second benefit of high modulation frequencies is the wider possible detection bandwidth, which can accommodate faster signals and therefore leads to faster measurements. For example, mobile communication systems are advancing to increasingly higher frequency bands¹¹ to accommodate higher

¹⁰ $f^{-\alpha}$ -noise is also called pink noise for the case $\alpha = 1$.

¹¹ The 6G standard could use 100 GHz and more.

bandwidths and less EMI. The modulation frequency in this work is limited to $f < 100$ MHz by the bandwidth of the low-noise amplified photodetector.

In addition to external interference, a very important source of noise in PM absorption spectroscopy is the laser itself. Sudden laser frequency jumps can lead to spurious amplitude noise at the PM modulation frequency, and wavelength drifts can cause systematic errors in the measurement. Chapter 8 discusses the laser system used to achieve minimal interference and the fast, fiber-based PM modulation method utilized in this work.

STABLE LASERS FOR SPECTROSCOPY

A continuous wave laser emits coherent light ideally at a single frequency. However, this frequency is subject to small temporal fluctuations, and thus the lasing intensity is fluctuating as well. Amplitude, frequency, and phase fluctuations result in spurious sidebands that can severely affect precise measurements or even render them impossible to perform. For this reason, stable laser operation is essential in any given experiment performed throughout this work, and great care has been taken with respect to the design, operational infrastructure, detection, and control schemes of lasers.

Fortunately, the D^0X transition has a very accessible wavelength in the near-infrared region at roughly ≈ 1078 nm. The near-infrared wavelength allows for the use of cost-efficient, high-performance semiconductor lasers, photodetectors, fiber optics, and optical fiber modulators. The following sections describe the tunable semiconductor lasers used in this work and different means of precisely measuring and controlling their frequency.

8.1 EXTERNAL CAVITY DIODE LASER

Semiconductor laser diodes based on the semiconducting compound material AlGaAs are very inexpensive and reliable [69]. Figure 27 shows the basic operating principle of an AlGaAs diode laser. Electron hole pairs are generated via electric current mainly within the optically active AlGaAs quantum well layer. The quantum well thickness, as well as the aluminum content¹, are chosen in order to achieve maximum photon emission at the desired wavelength. In a conventional external cavity laser diode (ECDL) design, one facet of the quantum well layer is terminated with a highly reflective

¹ The aluminum content heavily influences the size of the AlGaAs energy gap.

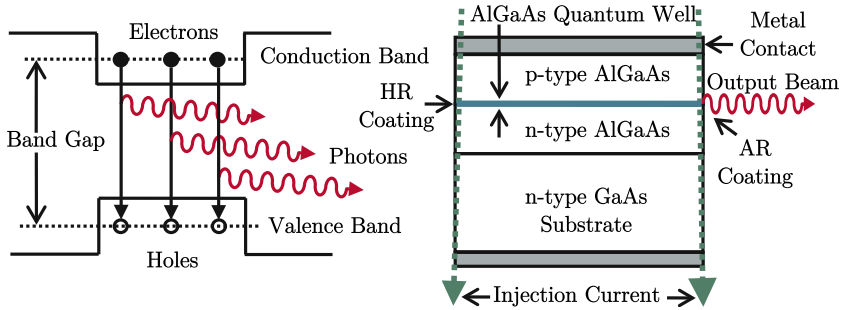


Figure 27: Functional principle of an AlGaAs quantum well diode laser. Adapted from Ref. [68].

coating, while the other facet is anti-reflection coated. External feedback is applied using dispersive optics, such as a blazed Bragg grating, to allow lasing at a controllable wavelength.

Figure 28 shows two different ECDL designs based on a conventional gain chip and a surface-angled facet (SAF) gain module, both of which are used in this work. The first-order diffracted beam of a blazed Bragg grating² provides external feedback to the optical gain medium. The position of the grating can be tuned via a piezo-electric actuator (PZT). The conventional ECDL gain chip has a highly reflective end facet as well as a transmissive feedback facet, and the zero-order reflected beam acts as the laser output. The SAF ECDL has a much lower reflectivity on the feedback side and therefore extremely minimized round-trip losses. Where the conventional ECDL is highly reflective on the opposite facet, the SAF module is slightly transmissive with an optimized transmission coefficient for maximum output power and stability. An optical fiber is spliced onto the output facet, allowing the laser to be conveniently connected to fiber optic devices, including modulators and isolators. The SAF design is a more modern development in ECDL technology and provides overall improved laser stability and single-mode power [70, 71].

² A narrow-band filter can also be used instead of a Bragg grating, leading to a “cats-eye” configuration [70] which can provide more frequency stability.

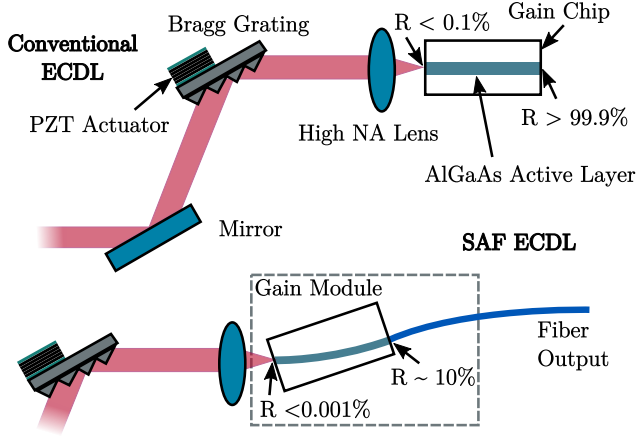


Figure 28: Two different external cavity diode laser designs. The upper design is based on a conventional gain chip, and the lower design is based on a surface-angle facet gain module.

As a consequence of the external cavity design, it is only possible for the diode laser to operate in specific resonant modes that meet the standing wave condition:

$$f_q = \frac{c}{2L}q. \quad (40)$$

Here, f_q is the frequency of mode q , c is the speed of light, and L is the effective optical path length of the resonator. The optical length L generally depends on the temperature and laser current due to thermal expansion of the cavity, atmospheric pressure changing the reflective index, and mechanical vibrations of the cavity. The frequency selectivity of the Bragg reflection grating is usually lower than the mode spacing $c/(2L)$ leading to mode competition and mode hopping.

There are several options to control the laser frequency and keep it operating in a single resonant mode. The PZT actuator voltage can be adjusted, the laser current can be slightly modulated, and the base temperature of the cavity and gain medium can be controlled. The PZT voltage allows for a wide frequency control on the

order of 10 GHz with a modulation bandwidth of approximately 100 Hz. On the other hand, the laser current can be changed very rapidly with a bandwidth of ≈ 1 MHz, but only allows for small tunability on the order of 100 MHz and influences the lasing intensity as an undesired side effect. Cavity temperature tuning is very slow and unreliable, and thus the cavity temperature is kept with millikelvin stability at a fixed value.

Optimal frequency control is achieved by dividing the control output into a high-frequency part and a low-frequency part through electronic filters. Depending on the task at hand, the lasing frequency may be modulated in an open loop, as is the case for electron polarization measurements, or in a closed feedback loop, as is the case for high-resolution spectroscopy. In any case, the frequency of the laser needs to be measured within a certain range of accuracy, for which there are two methods used here, Fizeau interferometry and heterodyne interferometry with a stabilized reference laser. Both methods are discussed in the following sections.

8.2 FIZEAU INTERFEROMETER

In this work, a commercial Fizeau interferometer³ is used to measure the absolute frequency of light. The light is coupled into the instrument via fiber and then collimated via a lens, before entering the solid-state Fizeau interferometers. The interference pattern is imaged by a cylindrical lens onto a Si-based CCD camera as shown in Fig. 29. The recorded interference pattern is analyzed to obtain the laser frequency with a nominal precision of 1 MHz. However, without continuous recalibration of the instrument, the detected frequency can drift on the order of 10 MHz within days due to changes in atmospheric pressure and temperature. The device has a fiber switch attached and therefore allows for simultaneous detection of two different laser frequencies.

While the wavelength meter allows for controlling laser frequencies via a PID feedback loop, there are several downsides to this method. On top of drift with atmospheric pressure and tempera-

³ HighFinesse Ångstrom WS Ultimate 2 Wavelength Meter

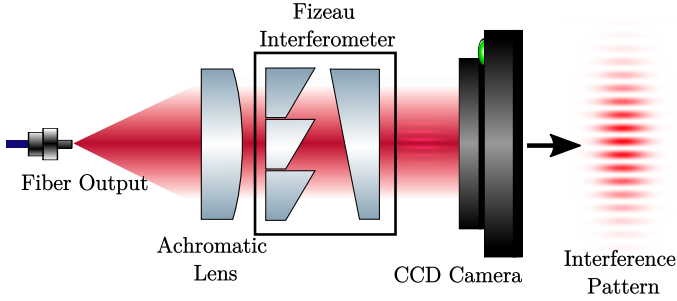


Figure 29: Schematic of a Fizeau interferometer used to measure the wavelength of coherent light.

ture⁴, the frequency detection bandwidth is very low on the order of 100 Hz. Due to the low detection bandwidth, fast mode hopping cannot be suppressed, and scanning the frequency is relatively slow, leading to increased noise and measurement time. For this reason, a different method based on a high-finesse optical cavity is used for precise laser frequency control, which is described in the next section.

8.3 HIGH FINESSE OPTICAL CAVITY RESONATOR

Ultrastable optical cavities are a standard tool for stabilizing laser systems used in high-resolution spectroscopy. The resonance frequencies of optical cavities depend on the longitudinal and transverse spatial modes and are given for the case of circular symmetry⁵ by [72]

$$f_{plq} = \frac{c}{2L} \left[q + \frac{2p + l + 1}{\pi} \arccos \sqrt{g_1 g_2} \right], \quad (41)$$

where p and l are the transverse mode indices, q is the longitudinal mode index, L is the optical mirror spacing, c is the speed of light, and $g_i = 1 - L/R_i$ are parameters depending on the radii of curva-

⁴ With coefficients $-0.58(3) \text{ MHz Pa}^{-1}$ and $-14(2) \text{ MHz K}^{-1}$, respectively.

⁵ The transverse spatial modes in Eq. 40 can be neglected because the gain medium is too small to support higher-order spatial modes.

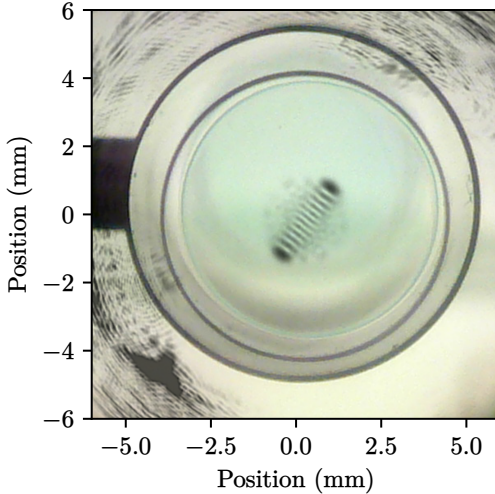


Figure 30: The home-built optical cavity resonator operating in a higher-order spatial mode. The two mirrors, as well as the frame machined from ULE glass, are visible as shadows in the picture.

ture R_i ⁶ of the two cavity mirrors. For a planar Fabry-Perot cavity, $g_1 g_2 = 1$ holds and all transverse mode frequencies are degenerate. In practice, however, it is not possible to produce perfectly flat mirrors, and the uncertainty in curvature causes slight frequency changes, which lead to mode competition and frequency instability. Therefore, the optical cavity used in this work has a plano-concave mirror setup where $g_1 g_2 = 0.725$. In this setup, the frequency degeneracy of the cavity is effectively lifted, and stable operation in a single spatial mode is possible without problems. The optimal choice of spatial mode for practical operation is the fundamental mode ($p = l = 0$) since it best matches the original spatial intensity distribution of a Gaussian laser beam.

To achieve optimal frequency stability of a fundamental longitudinal cavity mode, the correct choice of material and geometry for the resonator is of utmost importance. Ultra-low expansion (ULE) glass and a cylindrical cavity design are the best option here, as

⁶ $R_1 \approx 3$ km, $R_2 = 400$ mm and $L = 110$ mm, for the home-built resonator.

Finesse	Free spectral range	Zero crossing temperature
26×10^3	1.362 GHz	19(3) °C
Frequency drift	Linewidth	Temperature stability
1 kHz h ⁻¹	4 kHz	1.7 kHz mK ⁻¹

Table 5: Performance parameters of the optical cavity resonator.

they allow for a cavity with the lowest daily drift [73]. The low daily drift is achieved by the minimal thermal expansion of ULE glass at room temperature in combination with thermal decoupling and precise temperature control. The resonator is additionally kept in an ultra-high vacuum environment at all times using an ion-getter pump, thereby eliminating any atmospheric absorption or refractive index fluctuations. All these precautions combined lead to a daily drift on the order of 10 kHz which is more than sufficient for any experiment carried out in this work. Table 5 shows the measured parameters of the optical cavity. Here, the free spectral range (FSR) is the frequency spacing between two longitudinal modes in Eq. 41, and the finesse can be calculated from round-trip losses $2\pi/\rho$ where $\rho \approx 24 \times 10^{-5}$.

Locking the laser to any of the fundamental modes is possible around the design wavelength of 1.03(7) μm where the cavity mirrors are highly reflective. In practice, a frequency mode very close to the D⁰X absorption line (278.0332 THz) is used to allow frequency measurement close to the D⁰X resonance. The next section shall discuss how to use the very stable fundamental resonator modes to create a laser frequency reference to perform high-precision spectroscopy experiments using the D⁰X transition.

8.4 POUND-DREVER-HALL LASER STABILIZATION

The Pound-Drever-Hall (PDH) method is a sophisticated technique for stabilizing a laser using the reflected optical power of a high-finesse cavity resonator. While the frequency dependence of the reflected laser power is symmetrical around the cavity resonance,

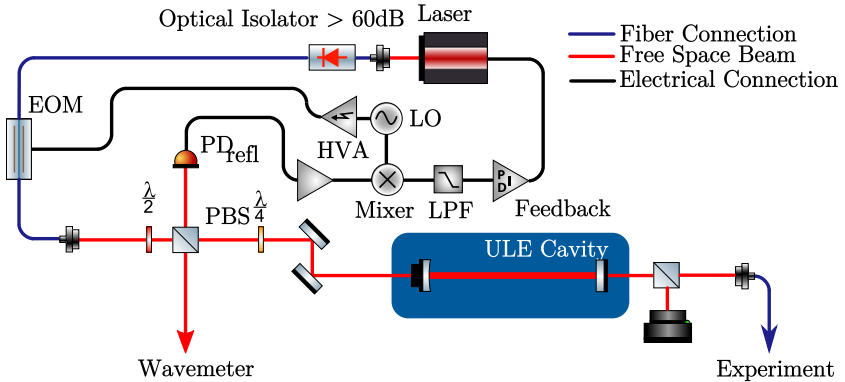


Figure 31: The setup used to stabilize a laser using the PDH technique. Mixer, local oscillator, and PID are integrated in the *Optica FALC110* module specifically designed for Pound-Drever-Hall frequency control. The laser current is modulated using the fast modulation input of the *Koheron CTL200* digital laser diode controller.

phase modulation of the laser can be used to create an asymmetrical error signal which is ideally suited for frequency control.

Figure 31 shows the setup that is used to detect the cavity reflection signal. The laser is coupled into a fiber, optically isolated, and phase modulated via a fiber electro-optic modulator (EOM). A half-wave plate is used to adjust the output powers of the polarizing beam splitter (PBS) cube, where one output is used to measure the absolute laser frequency using a wavelength meter, and the other output is sent into the cavity. The double pass of the quarter-wave plate after the PBS effectively rotates the reflected light polarization by $\lambda/2$ and causes it to be reflected onto the photodiode PD_{refl} . A local oscillator at the phase modulation frequency is used to demodulate the reflected signal to obtain a PM spectroscopy signal via quadrature demodulation (see Sect. 7.4).

The PDH error signal is fundamentally very similar to a PM absorption spectroscopy signal [74]. Figure 32 (b) shows the reflected optical cavity power and the resulting PDH error signal. The PDH signal can be readily calculated from the quadrature component Y in Eq. 33 and the cavity transmission profile. The resonance width is scaled up in Fig. 32 for visual clarity. The actual reso-

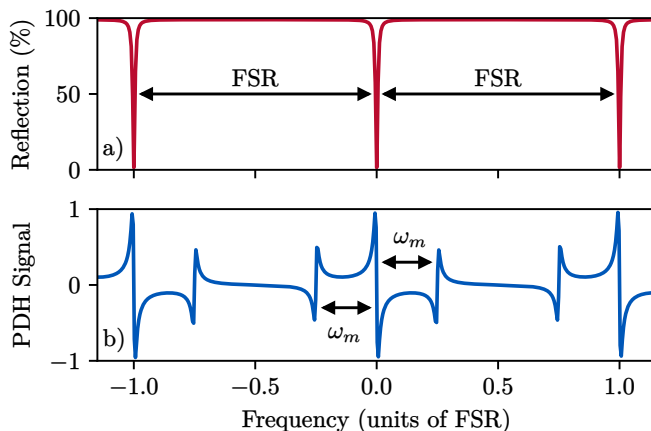


Figure 32: (a) The reflectivity of the cavity resonator. The width of the transmissive bands is exaggerated for visual clarity. (b) The Pound-Drever-Hall signal results from the PM signal demodulation. The sideband signal is shifted by the phase modulation frequency ω_m .

nance linewidth of the cavity in the experiment is $\gamma \approx 4$ kHz and the modulation frequency is $\omega_m = 20$ MHz. Because the modulation frequency is high $\omega_m \gg \gamma$ and the modulation depth is small $a \approx 0.1$, the sideband spectrum of the modulated laser is directly reflected by three distinct resonances in the PDH signal corresponding to the strong carrier and the two weaker sidebands. Locking the laser frequency can be performed very effectively using the steep slope of the PDH signal close to the carrier resonance (Fig. 32 b) as feedback for the laser frequency control. In principle, it is also possible to lock the laser in the transmission of one of the sidebands, which allows to create a variable offset of the carrier frequency and the resonance of the cavity by tuning the modulation frequency [75]. However, this approach has issues with frequency slew rate and is technically difficult to implement. A different method for laser frequency tuning is described in the next section, where the laser is locked into cavity resonance, and a tunable frequency offset is derived from a scannable laser by stabilizing their relative phase.

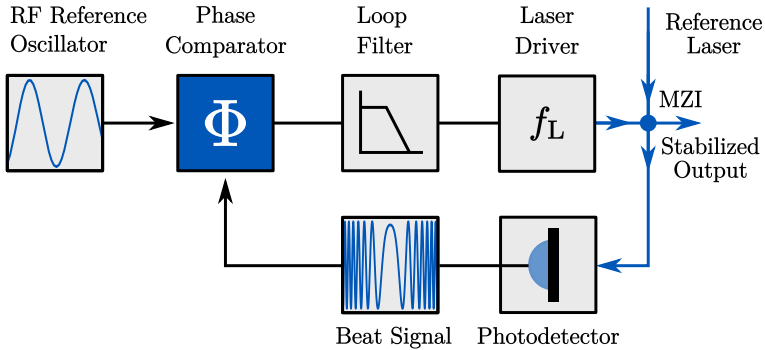


Figure 33: The flow diagram of an optical phase-locked loop (OPLL).

8.5 HETERODYNE BEAT-LOCK INTERFEROMETER

An optical phase-locked loop (OPLL) is a feedback control system that allows frequency stabilization between two lasers with an absolute, adjustable offset. Figure 33 demonstrates the working principle of a basic OPLL. A heterodyne beat signal is created by interference of two lasers inside a Mach-Zehnder interferometer (MZI) and detected via a fast photodetector. The relative phase of the beat signal and a stable reference oscillator is continuously detected by the phase comparator and output as a phase error signal. The error signal passes through a loop filter and is then supplied as feedback to the laser frequency control. The loop filter acts to adjust the frequency response of the error signal to remove undesired instabilities in the laser frequency control.

A special technique of phase locking is fractional synthesis. When a fractional phase comparator is used, it is possible to synthesize frequencies that are fractional values of the reference oscillator frequency. Fractional synthesis is performed by dividing the beat frequency and the reference oscillator frequency individually. The fractional synthesizer used in this work is a *Hittite HMC703LP4E* chip that works at high frequencies up to 8 GHz with programmable frequency output and support for arbitrary frequency waveforms. With a reference frequency of 20 MHz and a fractional resolution of 24 bits, the programmable frequency steps can be as low as

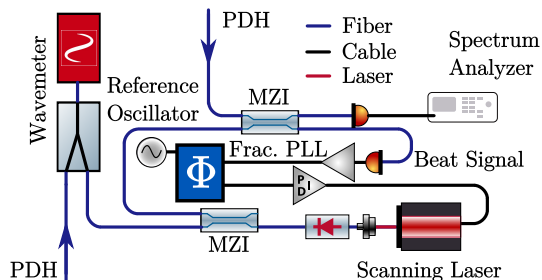


Figure 34: The setup for stabilizing of a heterodyne beat signal between the scanning laser and the reference laser. The reference input originates from the PDH setup in Fig. 31.

1 Hz which is more than sufficient for any experiment carried out here. Both the reference oscillator and synthesizer are integrated on a circuit board specifically designed for this setup. The loop filter used here is a *Koheron PI200* adjustable proportional-integral laser servo controller, which has a fast output for current modulation and a slow output for PZT modulation of the ECDL.

Figure 34 shows the setup infrastructure which provides precise and reliable frequency modulation for high-speed laser absorption spectroscopy experiments. The reference laser is locked via the PDH method to a ULE cavity (see Sect. 8.3 and 8.4). A fiber-based Mach-Zehnder interferometer (MZI) with outputs connected to fiber-coupled 5 GHz bandwidth photoreceivers are used to create the electronic beat signal between the two lasers. The spectrum analyzer detects the OPLL output spectrum during operation, and the wavemeter detects the absolute frequency and relative offset of the lasers.

The scanning speed and stability of the setup are verified by the measurements shown in Fig. 35. The laser is scanned around a center frequency of 700 MHz to verify the accuracy of the rapid frequency ramps. A fast continuously triggered FFT spectrometer⁷ records the MZI output signal to obtain the time-dependent beat frequency. A high slew rate of 400 GHz s^{-1} can easily be achieved, which is ideal for low-noise, time-resolved measurements. Opera-

⁷ The oscilloscope input of the Zurich Instruments UHFLI is used with a sample rate of 1.8 GHz.

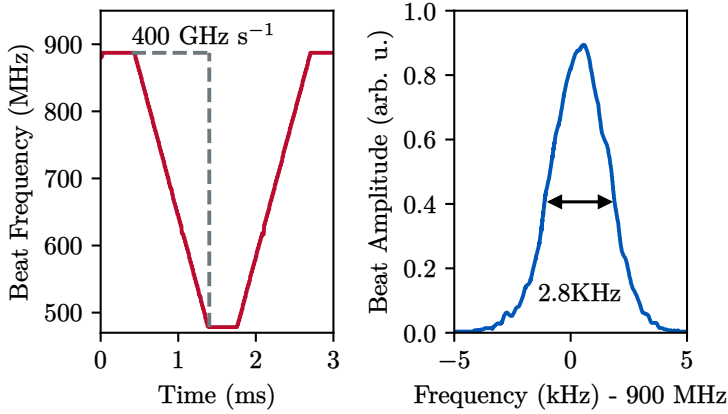


Figure 35: The frequency spectrum of the beat signal. **(a)** The beat signal is detected during a fast frequency scan and converted to a time-dependent frequency spectrum using a fast Fourier transform (FFT) spectrometer with a sampling rate of 1.8 GHz. **(b)** The beat note between reference and scanning laser for a set frequency of 900 MHz. The frequency spectrum is acquired by an *R&S 3000FSL* swept spectrum analyzer with a resolution bandwidth of 300 Hz and a sweep time of 100 ms.

tion at a constant programmable frequency offset is possible with a relative frequency stability of 2.8 kHz, which is very close to the estimated reference cavity linewidth of 4 kHz.

Part IV

EXPERIMENTS AND RESULTS

BANDGAP TEMPERATURE DEPENDENCE

9.1 INTRODUCTION

There exists a direct connection between the optical transition frequency of the donor-bound exciton and the Si bandgap. With this connection, it is possible to use the narrow frequency D^0X transitions in $^{28}\text{Si:P}$ to precisely determine the temperature dependence of the bandgap and measure the local lattice temperature. The temperature dependence of the bandgap is measured here in the regime from 0.05 K to 3 K to improve the temperature range, precision, and time resolution of existing data concerning the temperature dependence of the bandgap [25]. The absolute parameters of the behavior of $A \cdot T^p$ in the low temperature limit are verified and compared with the existing theory [32] yielding $p = 4.03(5)$ with high confidence. However, a discrepancy for A by a factor of approximately 30 compared to the theoretical value is extracted. The specially designed fast and precise laser scanning setup allows for precise measurement of the bandgap energy and facilitates time-resolved D^0X absorption measurements as a fast and contactless local thermometer. Together with the precise knowledge of the temperature dependence of the spin-lattice relaxation times [76], such a local thermometer can be used to verify the performance limitations of quantum technology based on electron donor spins in $^{28}\text{Si:P}$.

9.2 SETUP

The sample 3.1.6, with specifications given in Tab. 3, is placed inside the helium exchange gas insert described in Sect. 6.2. The insert is filled with ^4He at 1 bar pressure at room temperature before sealing. High-resolution PM laser absorption spectroscopy is used for precise measurements of the D^0X absorption frequency. Figure 36 shows the experimental setup for PM absorption measurements. A reference laser is locked to the ULE cavity with the PDH method (see Sect. 8.4). The scanning laser frequency is stabilized relatively to the reference laser frequency via an OPLL setup (see Sect. 8.5). The scanning velocities for this experiment are kept at 200 GHz s^{-1} and the laser is adjusted to allow for mode-hopping free scans over the zero-field D^0X spectrum. At zero magnetic field, the spin dynamics can be neglected due to the fast spin relaxation of the electron donor spin complex. At higher magnetic fields, optical spin pumping leads to a build-up of spin polarization which is undesirable as the spin population needs to be actively pumped back to probe the transition. The wavelength meter is used initially to lock the reference laser to the cavity resonance close to the zero-field absorption spectrum and to roughly adjust the bias and feedforward current of the scanning laser around the desired frequency range. Setting the PM frequency to 41 MHz suppresses interference fringes in the detected spectrum which originate from residual amplitude modulation in the fiber modulator. This exact modulation frequency matches the free spectral range of the fiber modulator and therefore causes the demodulated difference signal between the sidebands to vanish [77, 78] which improves the signal quality. Above-bandgap excitation (ABE) is applied via an ECDL laser tuned to 1022 nm wavelength. Complete absorption of light in the sample is guaranteed in very good approximation at this wavelength and therefore the ABE laser functions as a controllable local heat source.

The scanning laser is swept multiple times around the steep low-frequency flank of the zero-field absorption spectrum (see Fig. 21) with 400 MHz range. The resulting demodulated signal is averaged over each sweep into a single low-noise spectrum. Frequency scanning is performed by triggering the PLL circuit at a constant rate

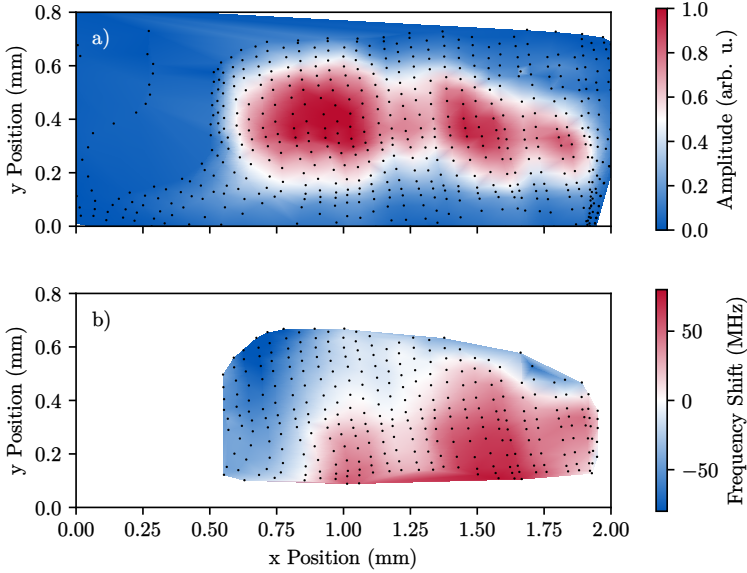


Figure 37: The measured dependence of the spectrum amplitude and center frequency on probe laser position relative to the sample, where black dots mark the probed positions. **(a)** The demodulation amplitude. **(b)** The central frequency shift in the regions of high amplitude.

using the AWG sequencer which results in a symmetric, triangular waveform devoid of any interruptions in-between the scans. Data acquisition and averaging are achieved by using the sequencer to trigger a digital oscilloscope¹ connected to the fast lock-in demodulation output in-sync with the frequency scan. The data from the oscilloscope is acquired and evaluated using a custom python program. The frequency shifts are computed with least squares optimization of the residuals between the measured spectrum and a reference spectrum shifted by a variable frequency. The low-noise reference spectrum is acquired by averaging a large number of spectra in a small temperature range. This technique works well for detecting small relative shifts, as is the case in this experiment.

¹ Meilhaus ME-5200 PCIe card with 2 MHz sample rate and 16-bit resolution

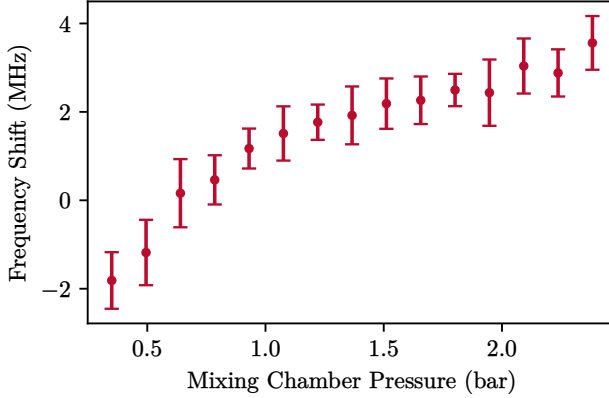


Figure 38: The effect of the mixing chamber pressure on the detected D^0X frequency.

While all the mentioned precautions act well to reduce the statistical error in the detected spectrum, the main systematic error originates from a probe laser position-dependent frequency shift. The positional amplitude and frequency variations of the spectrum are measured for different probe laser positions and are shown in Fig. 37. The patterns in the signal amplitude variations are believed to arise from a combination of optical aperture limitations and laser interference within the sample. The origin of the strong positional frequency shift might be sample strain or inconsistent doping concentrations, but it is ultimately unknown.

The positional frequency shift translates into a temperature-dependent shift mainly due to the following mechanism: The mixing chamber of the dilution refrigerator is filled with a $^4\text{He}/^3\text{He}$ mixture at a temperature-dependent pressure. The He pressure acts as a force upon the refrigerator construction and therefore leads to slight mechanical deformations and positional shifts. At temperatures below 0.7 K, all the helium mixture must be condensed inside the mixing chamber to provide sufficient cooling. To achieve very low temperatures down to 35 mK, the mixing chamber additionally needs to be heated to evaporate more ^3He which results in a high pressure up to 3 bar. Figure 38 shows the fre-

quency shift caused by pressure changes in the mixing chamber. By regulating the still heater with a digital PI feedback loop to a stable chamber pressure at 1.000(2) bar, and keeping the base temperature stable with a secondary cold plate heater, it is possible to achieve temperature control while maintaining constant mixing chamber pressure. With a slope value of 2.2(1) MHz bar⁻¹, the pressure-dependent shift is well suppressed for the given stability of 2 mbar. This method cannot be used for temperatures above 0.7 K, however, since the still heater is turned off and only part of the He mixture is condensed into the chamber for decreased cooling. With less of the He present, the still heater cannot be used to control the chamber pressure in this temperature regime. In addition to the lack of pressure control at higher temperatures, slight variations of about 0.5 MHz in the temperature-dependent frequency shift persist even under stable pressure. The origin of the residual shift is unknown, but it is probably caused by thermal expansion inside the cryostat. The residual shift is well suppressed by regulating the probe laser position relative to the sample using two additional lasers that measure the x and y positions of the sample insert. Positional feedback is applied to a PZT actuated mirror² via a digital PI control loop. The final frequency deviations that include all the precautions mentioned above are estimated at 0.2 MHz. The maximal absorbed power of the probe laser is only roughly 0.32 μ W which excludes any significant heating of the sample³, and therefore the cold plate temperature well represents the Si lattice temperature.

9.3 TEMPERATURE DEPENDENCE OF THE BANDGAP

Figure 39 shows the frequency shift of the bound exciton transition as a function of the cryostat base temperature. The data shows a monotonous decrease at the lowest and highest temperatures and a distinct dip around 1.5 K for the intermediate temperatures. This behavior can be understood by not only taking into account the

² The PZT mirror control is not used for time-dependent temperature measurements, and the positional control lasers are not shown in Fig. 36 for simplicity.

³ This is evident from the time-dependent ABE measurements discussed in the next section.

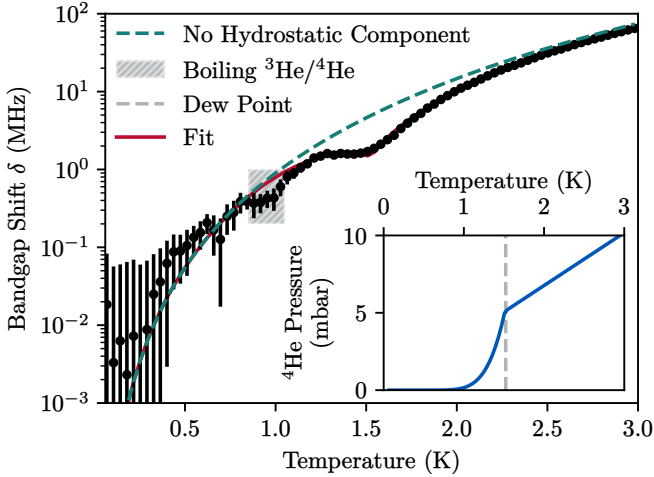


Figure 39: Temperature dependence of the bandgap of silicon.

theoretical limit of T^p , where $p = 4$ for $T \rightarrow 0$ according to Debye theory, but also a temperature-dependent pressure shift $k_h P(T)$ caused by the helium exchange gas. The theoretical He exchange gas pressure is calculated from the Van der Waals equation for He above the dew point, and from the T_{58} temperature scale [79] below the dew point. The pressure-temperature relationship of the exchange gas is shown as an inset in Fig. 39 and reveals a sharp drop around the dew point at 1.5 K which agrees well with the observations. The resulting functional relationship for the fit shown in red can be written as

$$\delta(T) = A \cdot T^p + k_h \cdot P(T), \quad (42)$$

where P is the exchange gas pressure, A is the electron-phonon coupling coefficient, $p = 4$ for $T \rightarrow 0$ according to the Debye theory (see Sect. 4.3), and k_h is the coefficient of hydrostatic shift. The fit yields $p = 4.03(5)$, which is well in accordance with the Debye theory. The optimized pressure coefficient $k_h = 0.64(5) \text{ MHz mbar}^{-1}$ disagrees in sign and magnitude with existing measurements [80] which might be due to the much lower hydrostatic pressures. The

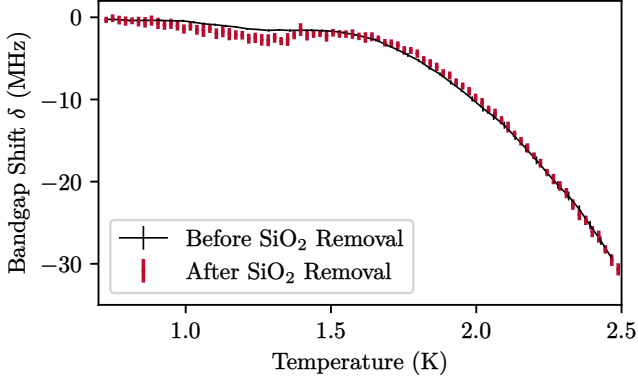


Figure 40: Temperature dependent frequency change before and after SiO_2 removal. The higher uncertainty of the data with SiO_2 removed is due to a shorter measurement duration with a decreased number of averages.

exchange gas pressure in the insert is at maximum 10 mbar, whereas the pressure in Ref. [80] is on the order of 10 kbar. An alternative explanation for the varying k_h value is sample strain. While the insert is designed to mount the sample strain-free, there might be some residual strain caused by the SiO_2 surface oxide which results in changes in the pressure coefficient. To test this proposition, the oxide was removed by hydrofluoric acid in a control measurement which is shown in Fig. 40. The control measurement indeed reveals a significant frequency change related to the pressure-dependent shift.

By comparing the dashed green line where $k_h = 0$ in Fig. 39 to the fit (red line), it becomes clear that the relative impact of the exchange gas pressure is largest around the dew point where the pressure drops sharply. For larger temperatures, the pressure only increases linearly in the exchange gas insert and the overall pressure is much less compared to a liquid helium immersion bath where the pressure increases exponentially. The impact of hydrostatic pressure on the measured parameters here is therefore much lower compared to Ref. [25], where the frequency shift is dominated by the

^4He vapor pressure. The high vapor pressure leads to increased uncertainty in the phonon coupling parameter because the hydrostatic pressure shift correlates with the temperature-dependent shift. The fit for this work yields $A = -0.90(5) \text{ MHz K}^{-p}$, which is roughly only half the value compared to Ref. [25]. The measured value A is closer to the theoretical phonon coupling coefficient, but still leaves a discrepancy of a factor 30. The factor of two discrepancy between the phonon coupling coefficient measured here and the one given in Ref. [25] is verified in a secondary control experiment with a higher temperature range up to 5 K and decreased absolute frequency resolution. This secondary experiment rules out the possibility of an experimental artifact related to the low frequency shifts in the regime below 3 K.

It is important to note that around 0.9 K, the boiling $^4\text{He}/^3\text{He}$ mixture causes additional pressure, and consequently positional fluctuations of the sample that cannot be suppressed by pressure regulation or positional feedback control. The relevant area is marked as gray in Fig. 39.

9.4 SAMPLE HEATING AND COOLING DYNAMICS

Presented in the following are the results of capturing the fast dynamics of the D^0X frequency using the high-velocity scanning setup. The measured frequency shifts are also used to detect the local lattice temperature in a contactless measurement via Eq. 42. To heat the sample locally, above bandgap excitation is used to create free carriers that relax through the Auger effect and subsequent phonon emission [56]. The AWG sequencer in Fig. 36 controls the ABE laser uptime with a resolution of 100 μs synchronously to the frequency scans to provide precise modulation of the heat input.

Figure 41 shows the change in D^0X frequency after switching the ABE on and off periodically every 16 s. Switching the excitation on results in the neutralization of charged ions, which changes the quasi-static electric field around the donor. After the excitation is turned off, the donors and acceptors become slowly ionized again due to donor-acceptor recombination. The frequency shift over time is multi-exponential and has a long time constant, which agrees with existing donor-acceptor photoluminescence measurement in

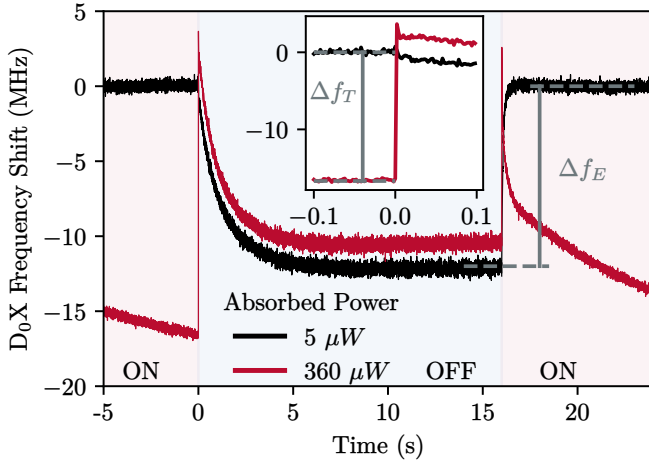


Figure 41: The D^0X resonance frequency dynamics after switching the ABE excitation on and off. The inset shows a persisting frequency offset, even when the ABE is switched off at $t = 0$. For low ABE powers, the electric field shift Δf_E is dominant, whereas for high ABE powers the temperature shift Δf_T becomes large as well.

low doped Si [81]. A significant Stark shift under absence of ABE for the 3.3.6 sample (see Tab. 3) is also reported in Ref. [44].

The frequency change according to the electric field of the donor bound exciton level can be estimated using the measured Stark shift of the D^0X transition of $0.80(17)$ MHz cm V⁻¹ [41]. The electric field distribution at the donor due to ionized donor-acceptor pairs can be calculated via the random distribution of dipoles. The average electric field in this approximation is [82]

$$\bar{E} = \frac{\Gamma_r d q}{4\pi\epsilon_0\epsilon_r} r_0^3, \quad (43)$$

where $\Gamma_r \approx 1.081$ is the half width of the Lorentzian field distribution, d is the average dipole length, and r_0 is the average distance between the dipoles. The dipole length and distance in the investigated sample can be calculated from the donor concentration ρ_D and the acceptor concentration ρ_A , respectively. Although the donor concentration is well determined at 1.2×10^{15} cm⁻³, the acceptor concentration ranges somewhere between 1×10^{12} cm⁻³ and 1×10^{14} cm⁻³. Using the average separation of $(4\pi\rho/3)^{-1/3}$ resulting from a Poisson distribution of donor and acceptor distances, the measured Stark shift of 12.1(2) MHz yields an acceptor concentration of $n_A = 4.6(10) \times 10^{13}$ cm⁻³. This value agrees well with the acceptor concentration measured in Ref. [83] for a ²⁸Si sample from the same growth facility. There is another small frequency shift of roughly 3 MHz which persists when the ABE is switched off. This effect, visible in the insert of Fig. 41, depends on the intensity of ABE and can be attributed to the screening of long-lasting surface electric fields by free carriers.

With an increase in the ABE power, the neutralization of the ions becomes faster and the temperature change of the sample becomes relevant as well. In contrast to sample heating, the final amount of neutralized ions does not increase significantly with higher ABE power. The electric field frequency shift caused by the ions can therefore be subtracted from higher-power measurements to obtain the temperature-dependent frequency shift only. Figure 42 shows the changes in sample temperature for switching on and off the ABE with 0.6 mW power. There is a striking difference be-

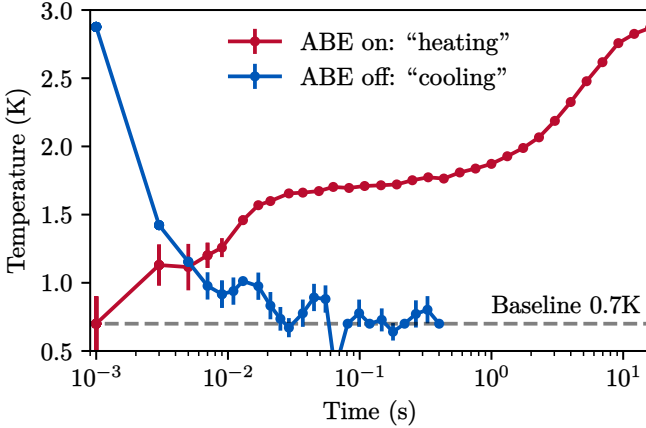


Figure 42: The lattice temperature dynamics calculated according to Eq. 42. The absorbed power during sample heating is 0.6 mW.

tween the heating and cooling dynamics, which can be explained by considering the two different sample cooling mechanisms. On the one hand, cooling is performed by convective exchange with the ^4He gas⁴ and, on the other hand, by proximity to the copper surface of the sample insert. When the sample is heated, the temperature rises slowly because the exchange gas has a finite thermal capacity and transfers heat to the sample insert continuously. When the heating is interrupted, the sample cools down quickly because there is only proximity heat transfer to the copper and not to the warmer exchange gas. To quantitatively describe this behavior, a linear heat transfer model is used, which is shown in Fig. 43. This model includes the sample temperature T_S , the exchange gas temperature T_H , the base temperature T_B , and the heat transfer due to the ABE excitation \dot{Q}_L . A quantitative description of the heat

⁴ The Rayleigh number is estimated from the insert geometry to surpass 10^5 , which is in the extremely turbulent regime. High Rayleigh number convection using cold helium gas is also investigated, e.g., in Ref. [84].

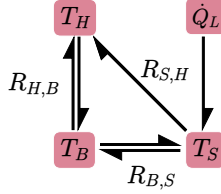


Figure 43: A flow diagram of the heat transfer model used to explain the results in Fig. 42. The corresponding set of differential Eqs. 44 to 46 quantitatively describe the heat flow.

transfer can be obtained by solving the following set of differential equations

$$\dot{T}_B = 0, \quad (44)$$

$$\begin{aligned} \dot{T}_S C_S &= \frac{(T_B - T_S)}{R_{B,S}} \\ &+ \frac{(T_H - T_S)}{R_{H,S}} \theta(T_S - T_H) + \dot{Q}_L, \end{aligned} \quad (45)$$

$$\begin{aligned} \dot{T}_H C_H &= \frac{(T_B - T_H)}{R_{B,H}} \\ &+ \frac{(T_S - T_H)}{R_{H,S}} \theta(T_S - T_H), \end{aligned} \quad (46)$$

where $R_{i,j}$ are the thermal resistances, C_i are the thermal capacities, and θ is the Heaviside step function. Simulating the heat flow is performed by calculating C_H from the specific heat of an ideal gas and the volume of the sample insert. C_S is taken as the specific heat of Si in the Debye limit [85] multiplied by the sample mass. The thermal resistances R_i are optimized to accurately describe the time dependence of T_S in Fig. 44. The simulation result with optimized boundary resistances matches the slow rise from exchange gas convection observed in the experiment and the rapid rise and fall due to the small heat capacity of the sample. The thermal capacities and optimized resistances are shown in Tab. 6.

Very fast ABE modulation isolates the proximity heat transfer from the slow heating of the exchange gas due to the small heat

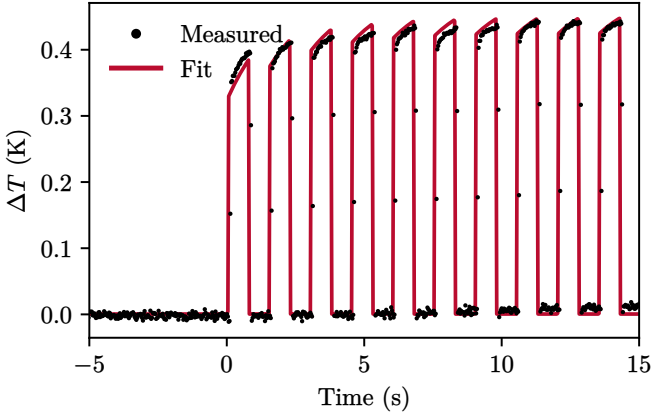


Figure 44: The measured temperature response for 1.5 s periodic modulation of the heat flow with 0.36 mW peak absorbed power and a base temperature of 2.0 K. The slow rise of the local maxima is caused by an increase in exchange gas temperature.

	Absolute (mK W ⁻¹)	Specific (mK W ⁻¹ cm ⁻²)
$R_{H,B}$	2.0(1)	0.20(1)
$R_{S,H}$	1.0(3)	4.7(3)
$R_{B,S}$	1.0(1)	31(3)
	(mJ K ⁻¹)	(C_V , J g ⁻¹ K ⁻¹)
C_S	$1.3 \times 10^{-8} T_S^3$	$8.6 \times 10^{-7} T_S^3$
C_H	1.75	3.1

Table 6: Thermal resistances and capacities used to solve Eqs. 44 to 46 with heat flow \dot{Q}_L according to Fig. 44.

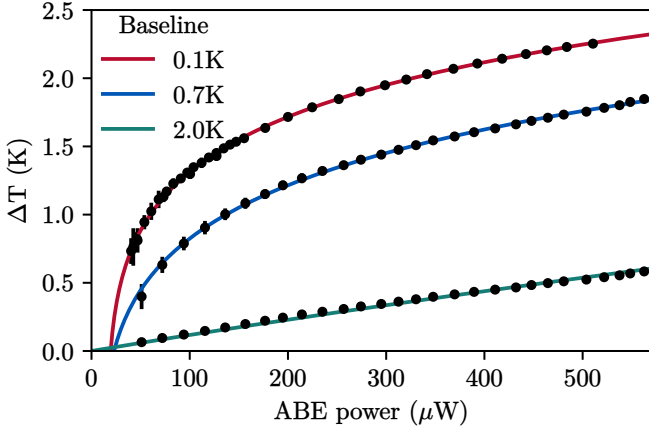


Figure 45: Results of fast ABE modulation with only 20 ms period and extraction of the temperature differences for different base temperatures. The green line is a quasi-linear fit according to Eq. 47 and the red and blue lines are logarithmic fits.

capacity of the sample. Following this observation, another experiment is performed where the ABE is modulated with a 20 ms period in order to extract the temperature-dependent thermal resistance between the sample and the copper surface. The fast modulation allows to separate the ABE neutralization effect of ions by assuming a steady-state neutralization given by the average ABE power applied. Subtracting this steady-state frequency using the known base temperature and Eq. 42 yields, with high accuracy, the temperature difference between the base and the sample. Figure 45 shows the resulting temperature differences for fast modulation of ABE depending on power and base temperature. For the base temperature 2.0 K, which is above the dew point, the behavior is quasi-linear. The quasi-linear behavior can be understood in terms of gas-gap conductance, where the heat flow is given by [86]

$$\dot{Q} = \frac{f}{12} \frac{k_B}{\sigma} \bar{v} \frac{\Delta T}{d} = \frac{f}{12} \frac{k_B}{\sigma} \sqrt{\frac{8k_B T}{\pi m}} \frac{\Delta T}{d}. \quad (47)$$

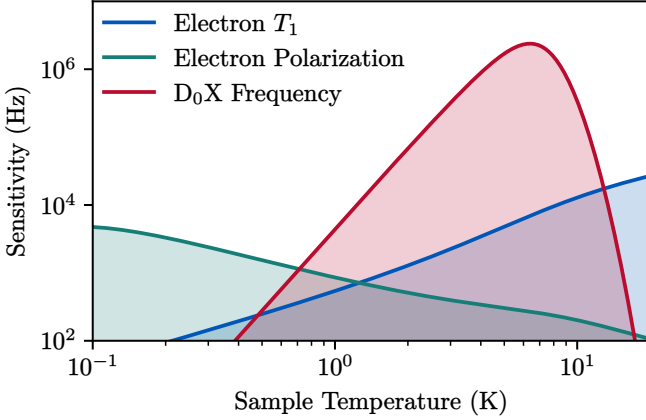


Figure 46: The relative sensitivity of different contactless temperature sensing techniques. The polarization measurement assumes an external magnetic field of 0.1 T and 0.1 % absolute accuracy [87]. The relative accuracy for the electron spin relaxation time T_1 is fixed at 1 %, and the absolute accuracy of the D^0X frequency measurement is 0.2 MHz.

Here, $f = 3$ are the three translational degrees of freedom, \bar{v} is the average velocity of the gas, σ is the effective atomic cross-section, m is the mass of the helium atom, k_B is the Boltzmann constant, and d is the average gap size. The only unknown in Eq. 47 is the average gap size, which depends on the surface roughness and curvature of both the sample and the copper. Fitting the surface roughness for $T = 2.0$ K yields the average gap size of $d = 13.0(1)$ μm , which is a realistic value given the unpolished copper surface [58]. For the base temperatures 0.1 K and 0.7 K, which is below the dew point, the ΔT behavior is logarithmic, which may be related to the roughly exponential decrease of helium vapor pressure. Heat is transported through ballistic He atoms for very low gas pressures and therefore the heat exchange scales linearly with the vapor pressure [58].

Building on the results of fast and precise time- and temperature-dependent measurements of the D^0X frequency, possible applications of the setup for non-contact temperature sensing are discussed below. Figure 46 shows the relative sensitivity of the D^0X

frequency measurements and compares them to measurements of electron polarization and electron spin relaxation times. The sensitivity parameter is defined according to Ref. [87] and describes the relative change in output for relative changes in temperature weighted by the measurement time and uncertainty. The comparison shows the excellent performance of the D^0X frequency thermometer in the range from 1.0 K to 10 K. For higher temperatures, the sensitivity decreases due to the thermal excitation of the D^0X and a spectral broadening due to phonon Raman scattering. The main issue of the other sensing techniques in this temperature regime is the long spin relaxation time of the donor-bound electron, which results in a long thermalization time of the spins.

LOW-TEMPERATURE RELAXATION OF D^0 ELECTRON SPINS

10.1 INTRODUCTION

The absence of nuclear spins in $^{28}\text{Si}:\text{P}$ reduces magnetic noise and thus allows for very long spin coherence times. While spin coherence times of seconds have been reported in $^{28}\text{Si}:\text{P}$ [5], they are fundamentally limited only by the spin-lattice relaxation time T_1 , which is cast into the inequality of $T_2 \leq 2T_1$ (see Sect. 5.4). Although the T_1 times of silicon donors have been studied in great detail for various doping concentrations [88], all of these studies date back half a century ago when highly pure, isotopically enriched Si material was not available. In addition to the low material quality, the exact theoretical description of the temperature dependence of the spin relaxation rate $\Gamma = 1/T_1$ is left ambiguous due to limited data points and accessible temperature ranges [24]. For example, the existence of the term $T^7 B^2$ in Eq. 20 can neither be confirmed nor ruled out by existing measurements [89]. The spin-lattice relaxation time at very low temperatures is known to depend on donor concentration [90–92] and is caused by the relaxation of donor clusters. The temperature dependence of this relaxation mechanism is unknown due to the lack of precise T_1 data at the lowest temperatures. Existing measurements regarding the magnetic field dependency of T_1 reflect the predicted TB^4 behavior, but the available data has an increased uncertainty caused by the specifics of ESR measurements [89]. The magnetic field in ESR measurements needs to match the resonance frequency of the microwave resonator, and thus must be swept back and forth to detect the magnetic field dependent spin relaxation time. The all-optical method presented in this work avoids this issue by directly detecting the spectrally narrow $D^0\text{X}$ absorption spectrum with a pump probe scheme which, among other benefits, allows for more than 80% initial D^0 polarization.

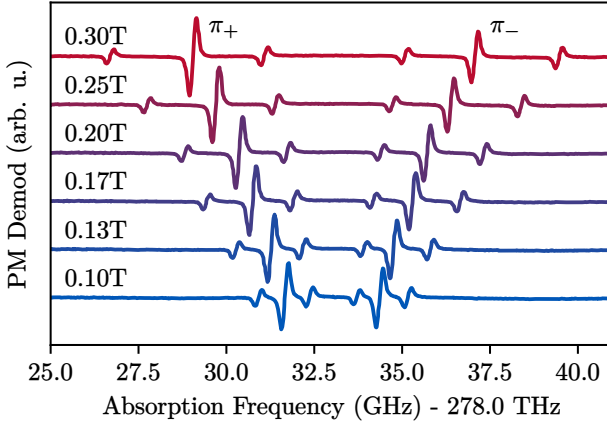


Figure 47: The D^0X PM absorption spectrum at different magnetic fields and 1.4K temperature. The small features correspond to the circularly polarized σ transitions and the larger features correspond to the linearly polarized π transitions.

10.2 SETUP AND METHODS

Frequency modulated absorption spectroscopy is ideal for measuring the D^0 spin-lattice relaxation at various magnetic fields and temperatures in $^{28}\text{Si:P}$ due to the narrow D^0X transitions, highly efficient optical pumping, and wide frequency scanning range. Figure 48 shows the setup used to perform high-precision pump probe experiments with donor spins in $^{28}\text{Si:P}$. A single phase-modulated ECDL pumps the donors and probes the D^0X transitions, which ensures that the spins are pumped and probed inside a perfectly overlapping, roughly $90\mu\text{m}$ wide region provided by the laser focus. The PM absorption signal of the probe laser is detected via a low-noise photodetector and a lock-in amplifier. Two shutters block the laser beam and any other light passing the cryostat windows during long durations over which the spins are neither probed nor pumped. The pump and probe powers are controlled via a motorized OD filter wheel to roughly 1 mW and $1\mu\text{W}$, respectively. The wavelength meter frequency control provides a long-term stability

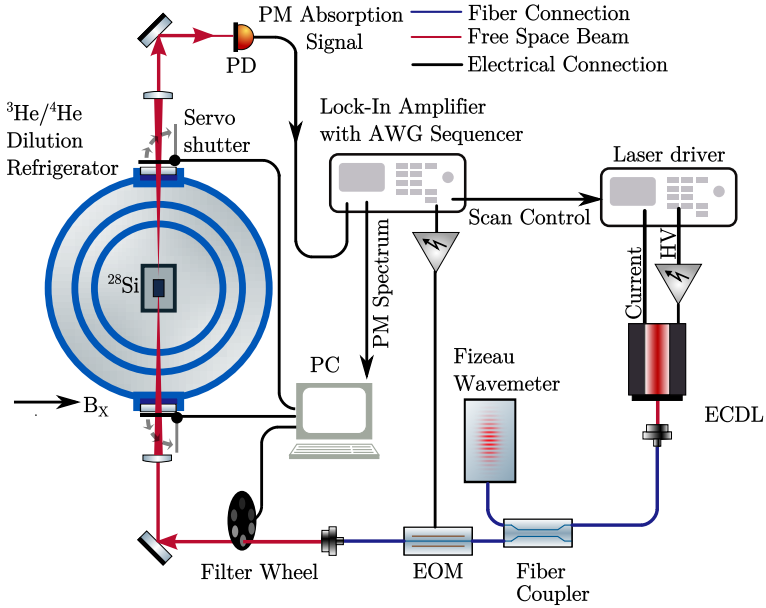


Figure 48: The setup for measuring T_1 relaxation times. Two servo shutters block the cryostat windows completely. A remotely controlled OD filter wheel controls the laser power for optical pump and probe experiments.

< 10 MHz of the laser and assures a correct scanning range and pumping frequency, even over measurement durations of days.

Because the experiment covers a wide range of magnetic fields from 0.1 T to 1.1 T, the magnetic field-dependent resonance frequency must be calibrated in the first step. Figure 47 shows PM absorption scans performed with the wavelength meter at different magnetic field values. The laser polarization in Fig. 47 is adjusted such, that a slightly elliptical polarization is obtained in order to show the circularly polarized σ transitions as well as the linearly polarized transitions. The distinct resonances in Fig. 47 are used to calibrate the exact frequency settings for efficient optical pumping at each magnetic field value. For the T_1 relaxation measurements, the laser is propagating along the [001] crystal axis, and the mag-

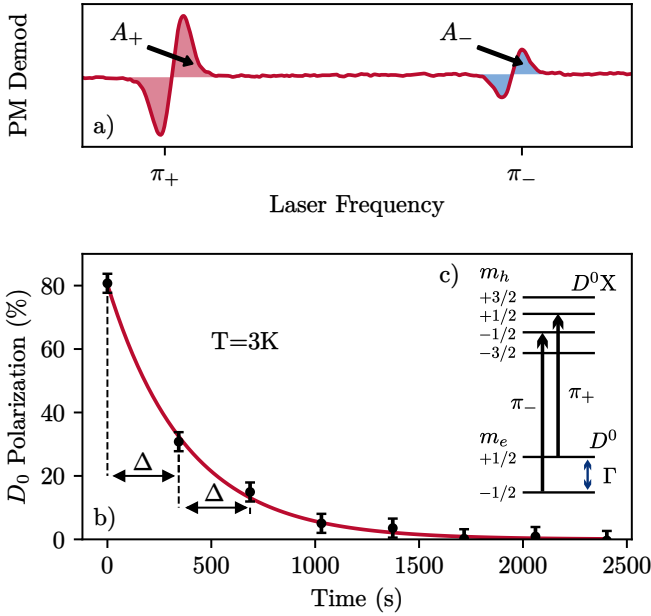


Figure 49: The polarization scan and time dependent polarizations.

(a) The differential absorption spectrum yields the D^0 spin polarization according to Eq. 48. (b) Polarization decay for $\Delta = 350$ s, $H = 60$ mT and $T = 3$ K. (c) Simplified energy level diagram marking the probed transitions and the corresponding spin relaxation rate $\Gamma = 1/T_1$.

netic field direction is transverse along the $[110]$ axis. Figure 49 shows an exemplary frequency scan that is used to detect the spin polarization of the donor electron. High initial spin polarizations are achieved by pumping the low-energy transition π_+ of the linearly polarized doublet. Over the duration of the optical pump, the laser is stabilized to the magnetic field dependent resonance frequency with the wavelength meter. For scanning over the π doublet transitions, the laser frequency offset is first adjusted to the calibrated midpoint between both transitions using the wavelength meter. After the scanning offset is adjusted, the laser frequency is swept twice within 100 ms in a symmetric triangular fashion to ob-

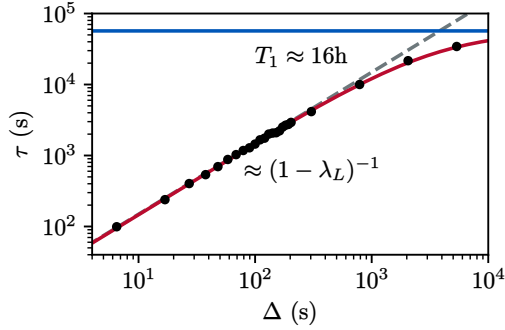


Figure 50: The dependence of the spin polarization decay times τ on the pause interval Δ at 0.5 K and 60 mT yields an intrinsic relaxation time of $T_1 \approx 16\text{h}$ (solid blue line). The laser depolarization factor in this measurement is $\lambda_L \approx 0.94$.

tain a single absorption spectrum. The offset needs to be adjusted regularly before each scan to compensate for laser frequency drift over long measurement times.

The D^0 spin polarization P is obtained by calculating the relative weighted difference between the absorption areas A of the doublet resonances in Fig. 49:

$$P = \frac{A_+ - A_-}{A_+ + A_-}. \quad (48)$$

Polarization measurements are performed at regular intervals Δ to obtain the polarization decay shown in Fig. 49. The cryostat windows are blocked completely over the duration of Δ by aluminum shutters to ensure that no residual parasitic light absorption occurs during this interval, which may cause spin polarization decay.

After each scan, the spin polarization decreases slightly due to the probe laser repopulation effect by a factor $\lambda_L \lesssim 1$. This effect results in an increase of the detected spin polarization decay time τ for longer measurement intervals Δ which can be seen in Fig. 50. The depolarization factor λ_L generally depends on the scanning speed, laser intensity and number of scans, but can be extracted

from the linear dependence for low Δ values shown as the dashed gray line in Fig. 50.

Measuring the D^0 spin relaxation times without perturbation due to the laser scanning is possible by measuring the polarization decay for increasing values of Δ . The dependence of the polarization decay constant τ on Δ is calculated in the following. After n scans, the laser polarization becomes

$$P_n = \lambda_L^n \exp(-\Gamma n \Delta'), \quad (49)$$

where $\Delta' = \Delta + 100$ ms is used to account for the duration of a single scan, and Γ is the intrinsic spin relaxation rate. The measured time-dependent spin-polarization decay can be written accordingly by using $t = \Delta' n$ as

$$P(t) = P_0 \exp(-\Gamma t) \lambda_L^{t/\Delta'} \quad (50)$$

$$= P_0 \exp(-(\Gamma - \ln(\lambda_L)/\Delta')t). \quad (51)$$

Equation 51 describes a simple exponential decay with an effective relaxation rate of

$$\Gamma_{\text{eff}} = \left(\Gamma - \frac{\ln(\lambda_L)}{\Delta'} \right). \quad (52)$$

Using the effective relaxation rate $\Gamma_{\text{eff}}(\Delta')$ allows to distinguish the intrinsic spin relaxation from laser-induced relaxation through measurements with increasing Δ . The red line in Fig. 50 shows a fit of Eq. 52 to the measured data, yielding an intrinsic spin relaxation rate of roughly 16 hours.

10.3 RESULTS

The intrinsic T_1 time is acquired in the same way using Eq. 52 for temperatures above 2.5 K and plotted as black dots in Fig. 51. In this regime, the spin relaxation is well described by the relation (see Sect. 5.4)

$$\frac{1}{T_1} = k_H B^4 T + k_9 T^9, \quad (53)$$

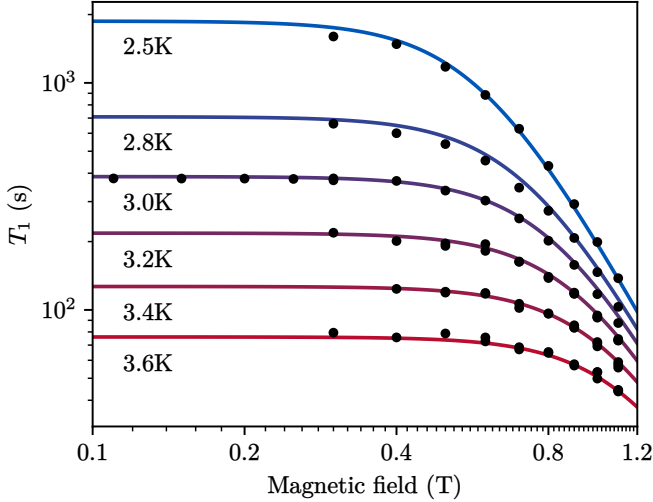


Figure 51: The magnetic field dependence of T_1 for intermediate temperatures 2.5 K to 3.6 K. The solid lines are calculated according to Eq. 53 with $k_H = 1.8(1) \text{ mHz T}^{-4} \text{ K}^{-1}$ and $k_9 = 0.13(2) \text{ } \mu\text{Hz K}^{-9}$.

where the coefficients k_H and k_9 are given in Tab. 7. The solid lines in Fig. 51 are calculated with the above constants and demonstrate an excellent agreement of the data with Eq. 53 over the entire range of parameters. The k_H and k_9 terms in Eq. 53 are already described in Refs. [18, 24, 89, 92]. To compare the coefficients with existing measurements on natural silicon, the relevant data is extracted from Refs. [18, 92, 93] and shown in Fig. 52. The resulting coefficients are summarized in Tab. 7. While the k_9 coefficient agrees well with ESR measurements in Ref. [18], the k_H coefficients vary for the different sources. The variations are likely due to a low accuracy of T_1 and fewer points for the magnetic field dependencies in Refs. [92, 93], as can be seen in Fig. 52. Compared to existing measurements of the magnetic field dependencies, the data in this work offers a much higher accuracy and a wider range of temperatures, which leads to a much higher precision for k_H . Nevertheless, it can be stated that the measurements for the intermediate temperature regime here agree in principle with the existing data, which is not

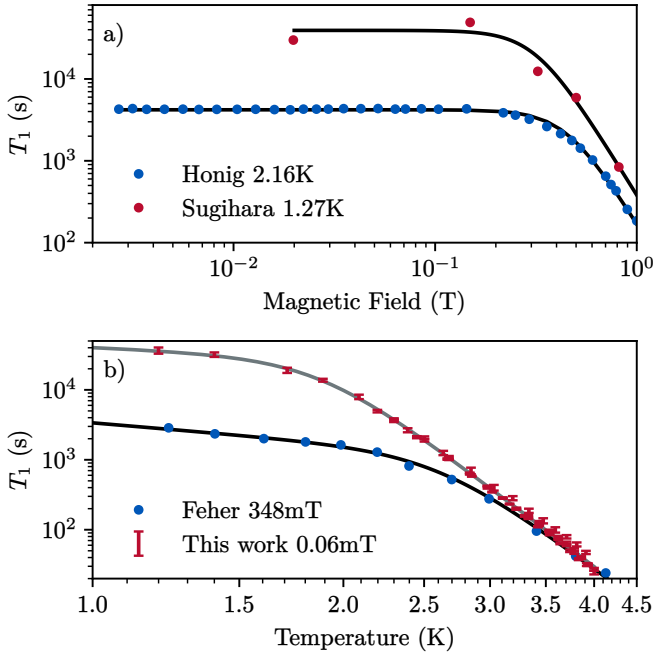


Figure 52: Measurements from Refs. [18, 92, 93] and the corresponding fits (black curves) which are performed to extract exclusively the TB^4 and T^9 coefficients shown in Tab. 7. The T^9 coefficient in this work has a much lower uncertainty compared to existing values due to the lower magnetic field, standard deviation, and more data points. (a) The solid lines are fits according to $1/T_1 = k_H TB^4 + k_0$ for the data in Refs. [92, 93] where the sample doping concentrations are in both cases $1 \times 10^{15} \text{ cm}^{-3}$. (b) The solid grey line is calculated from Eq. 55 and the solid black line is a fit according to $1/T_1 = k_H TB^4 + k_9 T^9$ using the data in Ref. [18] where the sample doping concentration is $n_d = 9 \times 10^{15} \text{ cm}^{-3}$. The lower magnetic field here leads to more reliable determination of k_9 due to the absence of the TB^4 dependency.

Table 7: Summary of the coefficients in Eq. 55 that completely describe the D^0 spin relaxation of the $^{28}\text{Si:P}$ sample. The data in the lower rows is extracted from measurements on natural silicon using the fits shown in Fig. 52. The value of $0.1 \mu\text{Hz K}^{-9}$ in Ref. [24] was likely also extracted using data from Ref. [18]. In Ref. [18] a T^7 dependence of $1/T_1$ was assumed, even though the T^9 dependence provides an equally good fit as demonstrated in Fig. 52.

k_0 (μHz)	k_1 ($\mu\text{Hz K}^{-1}$)	k_H ($\text{mHz T}^{-4} \text{K}^{-1}$)	k_9 ($\mu\text{Hz K}^{-9}$)
13(2)	11(3)	1.8(1)	0.13(2)
		2.6 ¹	0.1 ³
		0.8 ²	0.13 ⁴

¹Ref. [93] $n_d = 1 \times 10^{15} \text{ cm}^{-3}$ with B^4 fit from extracted data.

²Ref. [92] $n_d = 1 \times 10^{15} \text{ cm}^{-3}$ with B^4 fit from extracted data.

³Ref. [24] $n_d = 9 \times 10^{15} \text{ cm}^{-3}$.

⁴Ref. [18] $n_d = 7 \times 10^{15} \text{ cm}^{-3}$ with T^9 fit from extracted data.

surprising, since k_9 and k_H do not depend on sample quality or isotopic concentration.

The regime of very low temperatures is discussed next, where no experimental data was available up to date. Figure 53 shows measurements of T_1 between 0.5 K and 4 K for different magnetic fields. At a very low magnetic field and temperature, the spin relaxation time becomes extremely long, which is visible from the blue line in Fig. 53 that shows the 60 mT temperature dependence. In addition to the T^9 term at higher temperatures, the relaxation rate at low magnetic fields includes a linear term and is described by the relation

$$\frac{1}{T_1} = k_0 + k_1 T + k_9 T^9. \quad (54)$$

The two coefficients $k_0 = 13(2) \mu\text{Hz}$ and $k_1 = 1.8(1) \mu\text{Hz K}^{-1}$ are likely related to a neutral donor pair relaxation mechanism, which is described in, e.g., Refs. [89, 91]. Extrapolating the spin relaxation time to zero temperature at $H = 0.06 \text{ T}$ yields an extremely long value of $1/k_0 \approx 21 \text{ h}$. This relaxation time is orders of magnitude longer than the fundamental limit of T_1 assumed in Ref. [5].

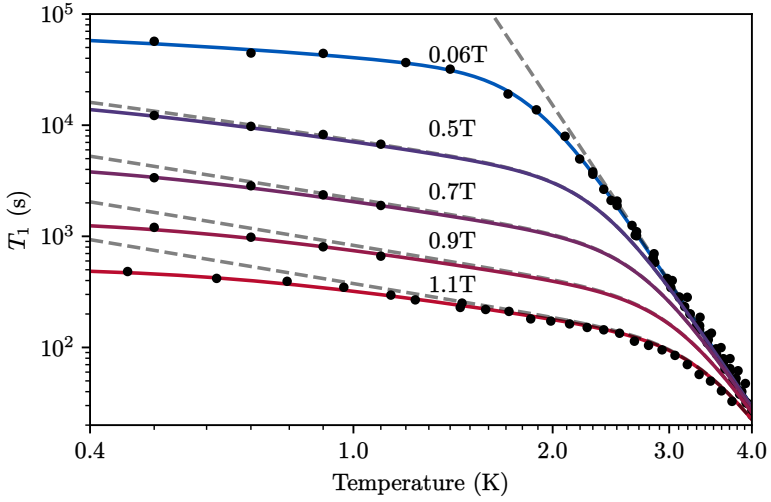


Figure 53: The spin relaxation time T_1 for very low temperatures and various magnetic fields. The dashed lines are calculated according to Eq. 53 using the coefficients given in Tab. 7. The solid lines are calculated according to Eq. 55, which includes the donor-donor pair relaxation terms and the bosonic phonon distribution factor.

For increasing magnetic fields and low temperatures, the TB^4 term no longer provides an accurate description of spin relaxation, which is well demonstrated by the dashed lines in Fig. 53. The low-temperature limit of the TB^4 term is already discussed in Ref. [94], and yields an additional factor that depends on the distribution of the phonon energies. Consequently, a full description of the spin relaxation at low temperatures is given by

$$\frac{1}{T_1} = k_0 + k_1 T + k_9 T^9 + k_H \frac{g\mu_B}{2k_B} B^5 \left(\frac{2}{e^{\frac{g\mu_B H}{k_B T}} - 1} + 1 \right), \quad (55)$$

where g is the electron g factor, μ_B is the Bohr magneton, and k_B is the Boltzmann constant. The expression above, together with the coefficients given in Tab. 7 gives a complete and accurate description of the T_1 time of the donor electrons for our sample.

Equation 55 yields at very low temperatures a B^5 dependence and not a TB^4 dependence, which can be seen by comparing the solid and dashed lines in Fig. 53. The low temperature regime is relevant for $^{28}\text{Si:P}$ quantum technology, as demonstrated in Ref. [95], where the external magnetic field is 2 T and the temperature is 40 mK. The T_1 time measured in Ref. [95] is about a magnitude shorter than detected here, suggesting a limitation by the Purcell effect in their device. The significant difference in the measured spin relaxation times shows that the T_1 times measured with the method here likely provide an upper limit of T_1 for the given sample, which can be used to evaluate the performance of $^{28}\text{Si:P}$ devices based on the same material system.

Part V

SUMMARY AND OUTLOOK

SUMMARY

The advent of scalable quantum technology drives the research with a prospect of more tools to solve difficult problems in many scientific areas. Silicon is still at the foundation of modern classical computers now and may also be in the future for integrated quantum technology, as shown here and by existing research on $^{28}\text{Si}:\text{P}$ donors and other defects.

In the first part of this thesis, I motivate the use of donor electrons in isotopically enriched silicon for quantum computational applications. The main focus is on the history of research on isotopically enriched silicon, including some of the astonishing properties of donors in the said material. The computational performance limitations given by the spin-lattice relaxation time which represents a limit for spin coherence is discussed. Measuring the silicon bandgap to evaluate the temperature of $^{28}\text{Si}:\text{P}$ based devices locally, and thereby determining their performance limit is motivated as well.

In the second part of this thesis, I summarize the existing theory on donor electrons and donor-bound excitons in $^{28}\text{Si}:\text{P}$. The summary includes the optical absorption spectrum of donor-bound excitons and the spin relaxation of donor electrons, as well as theoretical calculations of the temperature dependence of the bandgap for the Debye limit of phonons.

In the third part of this thesis, I present a basic setup to perform phase-modulated optical absorption spectroscopy with a tunable diode laser at cryogenic temperatures. The special design for a helium exchange gas insert provides efficient thermal transfer between the sample and the cryostat. Efficient thermal transfer between the sample and the insert is quantitatively demonstrated in a later chapter. Chapter 7 discusses the foundations of PM absorption spectroscopy and provides additional practical information on the optimal choice of modulation parameters for a given experiment. In Chap. 8, I present my setup for performing high

precision optical spectroscopy by locking the scanning laser phase to a stabilized reference laser using an optical phase-locked loop (OPLL). The OPLL performance is quantitatively evaluated and demonstrates the ability for fast sweeps with 400 GHz s^{-1} and a frequency stability of 2.8 kHz.

In Chap. 9 of the experimental part, I measure the temperature dependence of the donor-bound exciton transition frequency which allows to directly measure temperature shift of the Si bandgap with high precision. I am able to confirm that the the bandgap energy follows a T^4 dependence in the temperature range of 0.05 K to 4 K with high resolution absorption measurements at a relative accuracy for the bandgap energy of 7×10^{-10} . The T^4 dependence is in accordance with the Debye model of the phonon energy distribution in the low-temperature limit $T \rightarrow 0$. In this experiment, the phonon coupling coefficient is determined to be 30 times smaller than current predictions from theory, which suggests that cancellation of the acoustic phonon contributions is not completely accounted for in the latest published calculations. In time dependent measurements of the donor-bound exciton transition frequency, I determine a Stark shift of 12.1(2) MHz under above-bandgap excitation caused by a random distribution of ionized donor-acceptor pairs. Calculating the electric field of the random dipoles together with the known Stark shift of the D^0X transition yields the previously unknown acceptor concentration of $4.6(10) \times 10^{13} \text{ cm}^{-3}$. Using the above results, I lay the foundation for using the D^0X transition in $^{28}\text{Si:P}$ for local contactless measurements of the lattice temperature and small electric fields in ^{28}Si with a time resolution of 1 ms. The temperature measurements accurately describe the gas-gap heat transfer and convective heat transfer in the ^4He exchange gas sample insert. These results verify especially the efficient cooling of the sample in the custom sample insert and can be used generally to evaluate the heating of $^{28}\text{Si:P}$ based devices by local, contactless temperature measurements.

In Chap. 10, I establish an optical pump probe technique that allows to measure the intrinsic spin-lattice relaxation time with very high efficiency and has several benefits to classical electron spin resonance measurements. Using this technique, I determine the T^9 two-phonon Raman process as the only relevant mecha-

nism of donor electron spin relaxation in $^{28}\text{Si:P}$ at low magnetic fields for the intermediate temperature regime 2 K to 4 K. The two-phonon Raman coefficient is measured here with much higher accuracy and for a wider variety of magnetic field values than in existing data, which allows to rule out the ambiguous T^7H^2 Raman process measured in natural silicon with high confidence. At very low temperatures, an extremely long spin relaxation time exceeding 20 hours is measured exceeding orders of magnitude of the originally assumed limit. For low temperatures and high magnetic fields, I was able to observe the impact of the bosonic phonon distribution on the spin-lattice relaxation with high accuracy, which was predicted by theory but not observed until now.

As a result, my experiments further motivate the use of phosphorus donors in $^{28}\text{Si:P}$ for spin qubit applications by setting a new limit on the donor electron spin coherence. Compared to other optically addressable quantum systems such as self-assembled quantum dots and nitrogen-vacancy centres in diamond, donor ensembles in silicon are more suited for quantum computation due to the longer spin-lattice relaxation times and the efficient addressability. The small frequency variance between different donors in ultra-pure $^{28}\text{Si:P}$ bulk material is advantageous for coupling many donors resulting in an excellent scalability of the system. While these are great prospects for the donor electrons, they somewhat lack behind these other systems in quantum sensing applications and single photon generation because of the low temperature requirements and long radiative lifetimes of the excited states. However, self-assembled quantum dots can be engineered in size and shape in order to match the donor electron resonance frequencies and potentially allow for coupling and even entanglement between both quantum systems. This hybrid strategy would allow to use the best properties of each system for, e.g., storing, manipulating, and transmitting quantum information within larger computational clusters. As an outlook for future developments, it is useful to look at the initialization of registers of such donor spins integrated hybrid systems which could be performed optically via resonant absorption of coherent light. Resonant initialization of the donor electron spin is closely tied to spectral hole burning because the ensemble is broadened by the donor-donor interactions. The next chapter briefly dis-

cusses my results on spectral hole burning as an outlook for future experiments on donor ensembles.

OUTLOOK

12.1 SPECTRAL HOLE BURNING

Efficient spin state initialization is of utmost importance for fast and reliable quantum computation and quantum error correction schemes [3]. Understanding the mechanism of spin initialization by optical pumping in $^{28}\text{Si}:\text{P}$ requires studying the origin of the inhomogeneous broadening of the donor-bound exciton transition. Spectral hole burning with continuous ABE excitation and optical pump has already been used to determine the homogeneous linewidth of the donor-bound exciton transition in ^{28}Si and $^{\text{nat}}\text{Si}$ [45]. Unfortunately, Ref. [45] does not give a definitive explanation of the difference in the measured spectral hole width of 20 neV compared to the natural linewidth of 5 neV.

Instead of a steady-state approach, a different technique called persistent spectral hole burning is applied here to create and detect the spectral holes. Persistent spectral hole burning spectrally modifies the inhomogeneously broadened absorption lines in solids at low temperatures for time periods much longer than the lifetime of the excited states [96]. Although persistent spectral hole burning can provide additional insight into the mechanism of homogeneous broadening, to the best of my knowledge, there are currently no published experiments with persistent holes in Si. Since the donor electron spin relaxation times in Si:P become very long at low temperatures, it is possible to burn long-lived spectral holes into the broadened D^0X absorption spectrum, which can be manipulated and reset by ABE excitation. Such experiments with persistent holes give insight into the spin initialization time for the donor ensemble and single donors, which is relevant for quantum computational applications. Furthermore, the stochastically varying electric field imprinted by ABE excitation could be detected by measuring the frequency shift and width of the persistent spectral holes. According to Ref. [45] it may also be possible to obtain information

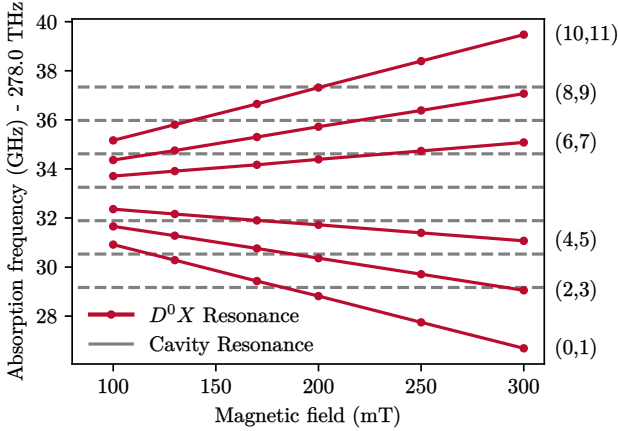


Figure 54: The resonant peaks in the D^0X absorption spectrum and the cavity transmission spectrum which has a mode spacing of roughly 1.362 GHz. The magnetic field dependence can be used to adjust the D^0X resonance frequency to one of the cavity resonances for spectral hole burning.

about the D^0X spin relaxation by measuring the magnetic field dependence of the spectral hole broadening.

The OPLL setup described in Chap. 9 is, with slight modifications, capable of burning and detecting very narrow persistent spectral holes by precise amplitude modulation and frequency control of the laser. Phase modulation absorption spectroscopy is ideal for detecting the narrow spectral holes that superimpose the broadened background absorption signal. The benefit, compared to DC absorption methods, lies mainly in the linear scaling of the PM absorption signal with the frequency derivative, which puts a higher relative weight to the narrow spectral hole compared to the wider background. Here, two approaches are used to create and detect spectral holes with the existing OPLL scanning setup. Firstly, the setup in Fig. 36 is modified to use the reference laser with ABE to create the spectral anti-holes in a steady-state, and secondly the scanning laser is modulated quickly in amplitude to burn and probe persistent spectral holes using only the scanning laser.

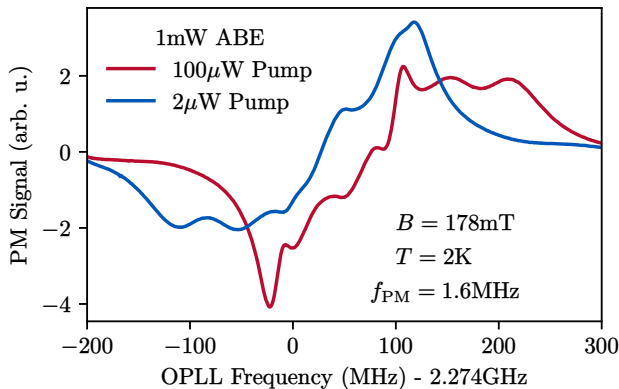


Figure 55: The PM demodulation spectrum obtained from probing the linearly polarized π_- transition in a transverse magnetic field under narrow-band optical pumping. The pump laser is locked to the ULE cavity and the magnetic field is chosen to match the π_+ transition frequency to the pump laser frequency. The probe laser is phase modulated at 1.6 MHz with a modulation index of $a \approx 0.7$ and scanned using the OPLL around a relative detuning of 2.274 GHz that matches the $\pi_- \rightarrow \pi_+$ frequency splitting at a magnetic field of 178 mT.

Burning spectral holes using the cavity-locked reference laser is possible by adjusting the magnetic field so that the π_+ transition overlaps with one of the cavity resonances. Figure 54 shows the cavity resonances as well as the D^0X resonances depending on the external magnetic field. At $B = 178$ mT, the π_+ resonance overlaps with one of the cavity resonances, and the reference laser creates spectral anti-holes at the π_- resonance. The spectral anti-holes can be detected by the probe laser using an OPLL frequency offset that matches the difference frequency between the π_+ and π_- transitions. In the first experiment, the steady-state spectral hole is created by continuous pumping of the π_+ transition using the reference laser and additional ABE which uniformly reverts the narrow-band spin polarization created by the pump. Figure 55 shows the spectrum obtained under the conditions above by scanning the probe laser around the π_- transition using the OPLL fre-

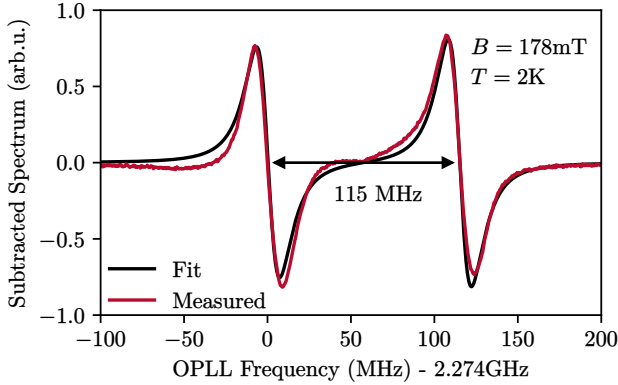


Figure 56: Experimental anti-hole spectrum obtained from subtracting spectra with periodic pump modulation. A Lorentzian distribution with $\gamma = 12$ MHz is shown as a black solid line. The measured separation of the two resonances is close to the hyperfine splitting of 117.53 MHz.

quency offset of 2.274 GHz at 0.14 T magnetic field. The resulting PM spectrum shows an undulation of the D^0X absorption depending on the pump power, which is caused by the spectral anti-holes. The background-free anti-hole spectrum is obtained by periodically switching the pump on and off between the scans and subtracting the according spectra. Figure 56 shows the subtracted spectrum obtained in this way. The anti-holes which exist for the transition with opposite electron spin become clearly visible in the background-free spectrum. The anti-hole spectrum shows two distinct peaks, which are separated by the D^0 hyperfine splitting. These two peaks originate from the reversal of nuclear energies for the opposite electron states [45]. Although the relative depth of the two anti-hole peaks depend on the magnetic field setting, they are equal if the pumping laser is in the center of the two π_+ transitions (2,3 in Fig. 11) where both nuclear states are pumped equally with the same probability. The widths of the anti-holes are determined by a fit of Lorentzian resonance ($\gamma = 12$ MHz) with the PM spectrum which is shown as the black solid line in Fig. 56. The fit does not describe the spectrum perfectly due to the high PM index of $a \approx 0.7$ in this

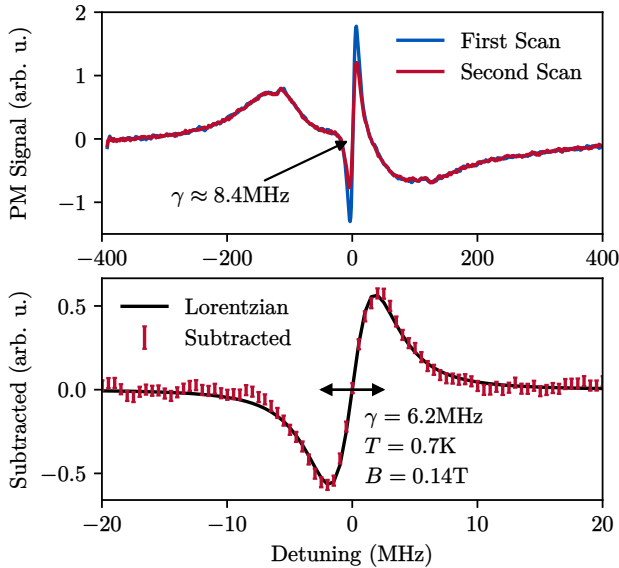


Figure 57: Persistent spectral hole which is burned and probed by the same laser. The phase modulation index is $a \approx 0.06$ and much lower compared to Fig. 55. The hole is burned with a power of $10 \mu\text{W}$ for the duration of 0.16 ms . The spectra after the first and second scan are subtracted to obtain the background-free hole spectrum shown in the lower part of this figure.

measurement, which leads to a spectral distortion (see. Chap. 7). Therefore, the actual width of the holes is expected to be significantly smaller.

Next, persistent spectral hole burning is performed with smaller modulation indices to determine the width of the spectral holes in the absence of spectral distortion. Persistent spectral hole burning is performed by modulating the scanning laser with a high-speed fiber Mach-Zehnder modulator. The holes are burned with $10 \mu\text{W}$ maximum power of the laser for a defined duration, and scanned with an intermediate power of $1 \mu\text{W}$. The following procedure is used to burn persistent holes using the scanning laser: First, the laser power is adjusted to zero and the laser frequency is set close

to the center of the resonance. Next, the laser power is adjusted to maximum amplitude for a defined pump duration τ_p between 10 μs and 10 ms using the fast modulator. After the pumping, the laser amplitude is adjusted to zero again and the frequency is quickly set to the edge of the scanning range. From there, the laser amplitude is set to an intermediate value of 1 μW and is quickly scanned twice back and forth over the resonance to obtain the hole spectrum. The result of this procedure is demonstrated in Fig. 57. A single spectral hole is visible overlaid on the inhomogeneous background spectrum. The width of this hole is about 8.4 MHz, and therefore slightly smaller than the width of the anti-holes, which is due to a lower modulation index $a = 0.06$ in this experiment. The spectral hole depth is slightly reduced after the first scan, which is due to optical pumping from the scan laser. Because the scanning speed is well controlled in the OPLL setup, the spectra of the first and second scans can be subtracted to obtain a background-free hole spectrum, which is shown in the lower part of Fig. 57. The subtracted hole spectrum is well described by a Lorentzian distribution derivative which can be seen by the solid black line in Fig. 57. The width $\gamma = 6.2 \text{ MHz}$ of the background-free spectrum is lower compared to the unsubtracted width and depends on the depth of the spectral hole.

Using this procedure, the dependence of the pump duration on the spectral hole broadening and depth is investigated. Figure 58 shows the spectral holes with different pump durations. While there is a slight asymmetry which originates from the inhomogeneous background distribution, it can clearly be seen that the Lorentzian shape becomes wider and distorted for longer pump durations, which is due to the saturation of electron spin polarization. The width and depth of the spectral holes are plotted in Fig. 59 to determine pump rates and the onset of pump saturation. The depths are shown as red dots and follow a logarithmic dependency, which indicates that the given pump durations are within the saturation regime. The widths γ are obtained by subtracting the background as in Fig. 57 and plotted as blue dots in Fig. 59. There is a visible increase in γ for longer pump durations which is caused by the saturation effect. Extrapolating the hole widths for small pump durations yields the limiting value of $\gamma \approx 5 \text{ MHz} \hat{=} 21 \text{ neV}$. This value

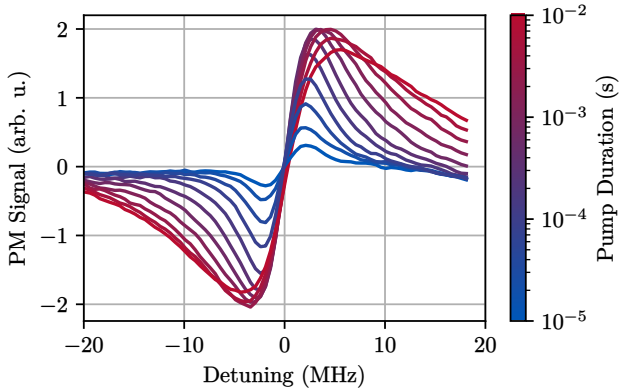


Figure 58: Evolution of the persistent spectral hole for increasing pump durations at 0.14 T magnetic field and 0.7 K temperature. The PM signal is obtained with a modulation frequency of 1.5 MHz and index 0.06.

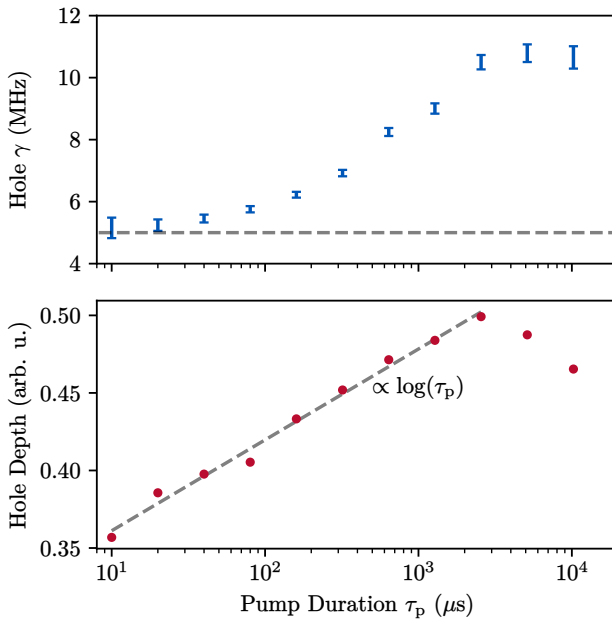


Figure 59: The persistent hole spectra in Fig. 58 are evaluated for the widths γ and depths. The FWHM value approaches 5 MHz for decreasing pump durations and the hole depths increase logarithmically due to saturation.

is close to the value of 20 neV obtained by extrapolating to zero pump power in Ref. [45] using sample c in Tab. 3.

In conclusion, I have demonstrated the creation and detection of steady-state anti-holes and persistent spectral holes using the existing OPLL setup. Different methods for background subtraction are provided above, which allow to accurately determine the linewidth of the spectral holes. The linewidths of persistent holes are determined at a very low PM index and extrapolated for decreasing pump durations resulting in a homogeneous linewidth of 5 MHz which well agrees with existing measurements. Nevertheless, to understand the discrepancy between the lifetime limited linewidth and the measured homogeneous linewidth more experiments are necessary. Possible experiments include time-dependent ABE manipulation of spectral holes, which could determine the impact of ion charge fluctuations in the donor environment on the homogeneous linewidth, as well as the magnetic field dependency of γ which may determine the influence of D^0X spin relaxation on the measured linewidths.

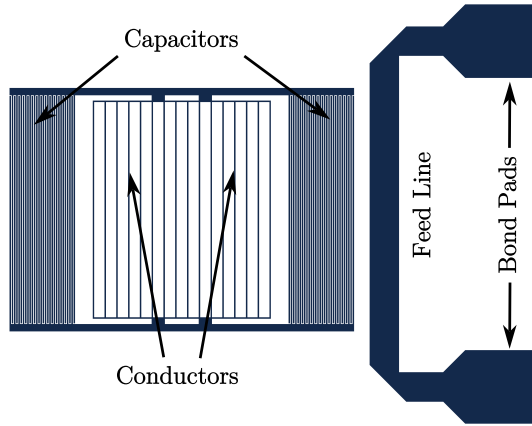


Figure 60: Layout of a niobium microresonator. The feed line capacitively couples the transmitted power to the resonator. The resonator is similar to a LC circuit, with the conductors in the middle and two capacities on the sides.

12.2 MICRORESONATORS FOR ESR

Electron spin resonance is a powerful technique ideally suited to generate control sequences for manipulating spins [54]. ESR plays an important role in the control of donor electron spins in $^{28}\text{Si:P}$, because it can drive the quantum coherence of donor electrons that are excellent carriers of quantum information [2]. Although a different method exists for driving two-level systems with dichromatic laser pulses [97], the applicability to the donor spin ensemble in $^{28}\text{Si:P}$ is questionable due to the low optical oscillator strength of the D^0X transition. Therefore, the only obvious way to drive the two-level D^0 ground state coherence is a microwave magnetic field source. There are several issues with integrating a microwave resonator into the existing low-temperature setup. While the cryogen-free dilution refrigerator is ideal for long-term low-temperature measurements, it only possesses a limited cooling power of 4 mW at the lowest temperatures. The low cooling power is a problem for conventional ESR resonators because they need powers $\gtrsim 10$ mW [98] to create sufficient magnetic field magnitudes due to resis-

tive losses inside the conductor. For this reason, superconducting microwave resonators (microresonators) are more suited to perform ESR experiments with the given setup. Several designs have been researched for various applications including spin resonance with donor electrons in $^{28}\text{Si:P}$ [99–103]. Figure 60 shows the specially designed microresonator for the given setup. The design utilizes a combination of conductors and capacities and therefore behaves very similarly to a LC resonator. The conductor count and their spacing is optimized via electromagnetic simulations to provide a very homogeneous magnetic field distribution for the sample mounted roughly $100\ \mu\text{m}$ above the conductors. Compared to standing waveguide resonators, the LC design allows for more compact dimensions and high magnetic field homogeneity for the given operating frequency. The conductor of choice for the resonator is elemental niobium, which becomes superconducting below $\approx 9\ \text{K}$ and has a critical magnetic field of $\gtrsim 0.35\ \text{T}$ in the thin-film plane [104]. Niobium is sputtered with $150\ \text{nm}$ thickness on a sapphire substrate, mounted on top of a PCB, and connected with short bond wires to the RF feed-line. The sample is mounted on top of the resonator with a $100\ \mu\text{m}$ thick spacer made of Kapton tape.

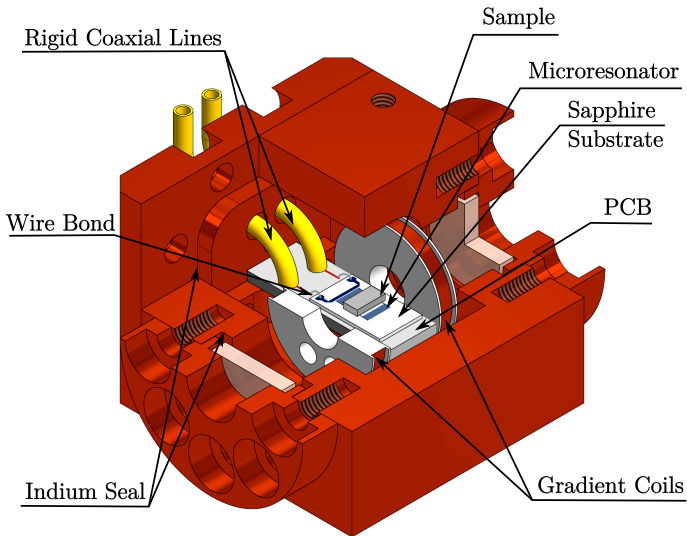


Figure 61: The exchange-gas sample insert for simultaneous optical absorption and ESR experiments.

12.3 SAMPLE INSERT FOR ESR

The sample insert made of non-magnetic beryllium copper for low-temperature RF experiments with the microresonator is shown in Fig. 61. The design is fundamentally similar to the insert in Fig. 18, but it has added mounts for the microresonator PCB and high-frequency coaxial electric connections. Additional gradient coils allow to precisely adjust the magnetic field offset and gradient for the ESR experiments. The main difficulty in assembling the sample insert is to create the electrical feed-through and prevent He-II leaks at the same time. To ensure leak-tightness, the coaxial lines are made from a rigid copper tube via insertion of the inner insulation from a conventional coaxial cable. The problem with using conventional coaxial cables directly is the woven copper mesh, which can easily cause leaks. The isolator and copper tube are bonded with Stycast epoxy to the insert at elevated temperatures 60°C to 70°C . All parts need to be sanded and ultrasonically cleaned prior to the bonding process to prevent leaks.

BIBLIOGRAPHY

- ¹A. G. J. MacFarlane, J. P. Dowling, and G. J. Milburn, “Quantum technology: the second quantum revolution,” *Philos. Trans. Royal Soc. A* **361**, 1655 (2003).
- ²A. Chatterjee et al., “Semiconductor qubits in practice,” *Nat. Rev. Phys.* **3**, 157 (2021).
- ³D. P. DiVincenzo, “The Physical Implementation of Quantum Computation,” *Fortschritte der Phys.* **48**, 771 (2000).
- ⁴T. D. Ladd et al., “Quantum computers,” *Nature* **464**, 45 (2010).
- ⁵A. M. Tyryshkin et al., “Electron spin coherence exceeding seconds in high-purity silicon,” *Nature Mater.* **11**, 143 (2012).
- ⁶A. Morello, J. J. Pla, P. Bertet, and D. N. Jamieson, “Donor Spins in Silicon for Quantum Technologies,” *Adv. Quantum Technol.* **3**, 2000005 (2020).
- ⁷D. B. Higginbottom et al., “Optical observation of single spins in silicon,” *Nature* **607**, 266 (2022).
- ⁸L. Feng et al., “Silicon photonic devices for scalable quantum information applications,” *arXiv*, [10.48550/ARXIV.2208.05104](https://arxiv.org/abs/10.48550/ARXIV.2208.05104) (2022).
- ⁹B. E. Kane, “A silicon-based nuclear spin quantum computer,” *Nature* **393**, 133 (1998).
- ¹⁰J. H. Wesenberg et al., “Quantum computing with an electron spin ensemble,” *Phys. Rev. Lett.* **103**, 070502 (2009).
- ¹¹A. Bienfait et al., “Controlling spin relaxation with a cavity,” *Nature* **531**, 74 (2016).
- ¹²A. Bienfait et al., “Reaching the quantum limit of sensitivity in electron spin resonance,” *Nature Nanotech.* **11**, 253 (2016).
- ¹³C. Eichler, A. J. Sigillito, S. A. Lyon, and J. R. Petta, “Electron spin resonance at the level of 10^4 spins using low impedance superconducting resonators,” *Phys. Rev. Lett.* **118**, 037701 (2017).

- ¹⁴G. Flower, J. Bourhill, M. Goryachev, and M. E. Tobar, “Broadening frequency range of a ferromagnetic axion haloscope with strongly coupled cavity–magnon polaritons,” *Phys. Dark Universe* **25**, 100306 (2019).
- ¹⁵P. Y. Yu and M. Cardona, *Fundamentals of Semiconductors*, Vol. 1, Graduate Texts in Physics (Springer, Berlin, 2010).
- ¹⁶R. C. Fletcher et al., “Spin Resonance of Donors in Silicon,” *Phys. Rev.* **94**, 1392 (1954).
- ¹⁷J. M. Luttinger and W. Kohn, “Motion of Electrons and Holes in Perturbed Periodic Fields,” *Phys. Rev.* **97**, 869 (1955).
- ¹⁸G. Feher, “Electron spin resonance experiments on donors in silicon. i. electronic structure of donors by the electron nuclear double resonance technique,” *Phys. Rev.* **114**, 1219 (1959).
- ¹⁹A. S. Kaminskil, V. A. Karasyuk, and Y. E. Pokrovski, “Luminescence of excitons bound to phosphorus atoms in silicon subjected to a magnetic field,” *Sov. Phys. JETP* 52(2) **45**, 211 (1980).
- ²⁰M. Cardona and M. L. Thewalt, “Isotope effects on the optical spectra of semiconductors,” *Rev. Mod. Phys.* **77**, 1173 (2005).
- ²¹P. Becker, H.-J. Pohl, H. Riemann, and N. Abrosimov, “Enrichment of silicon for a better kilogram,” *Phys. stat. sol.* **207**, 49 (2010).
- ²²A. Yang et al., “Single-frequency laser spectroscopy of the boron bound exciton in ^{28}Si ,” *Phys. Rev. B* **80**, 195203 (2009).
- ²³K. Saeedi et al., “Room-Temperature Quantum Bit Storage Exceeding 39 Minutes Using Ionized Donors in Silicon-28,” *Science* **342**, 830 (2013).
- ²⁴T. G. Castner, “Raman Spin-Lattice Relaxation of Shallow Donors in Silicon,” *Phys. Rev.* **130**, 58 (1963).
- ²⁵M. Cardona, T. A. Meyer, and M. L. W. Thewalt, “Temperature Dependence of the Energy Gap of Semiconductors in the Low-Temperature Limit,” *Phys. Rev. Lett.* **92**, 196403 (2004).
- ²⁶B. E. Deal and A. S. Grove, “General relationship for the thermal oxidation of silicon,” *J. Appl. Phys.* **36**, 3770 (1965).

- ²⁷R. Pierret, *Advanced semiconductor fundamentals*, Modular series on solid state devices (Prentice Hall, 2003).
- ²⁸K. Nishikawa and R. Barrie, "Phonon broadening of impurity spectral lines: i. general theory," *Canadian J. Phys.* **41**, 1135 (1963).
- ²⁹Y. P. Varshni, "Temperature dependence of the energy gap in semiconductors," *Physica* **34**, 149 (1967).
- ³⁰M. Cardona and R. K. Kremer, "Temperature dependence of the electronic gaps of semiconductors," *Thin Solid Films* **571**, 680 (2014).
- ³¹R. Gross and A. Marx, *Festkörperphysik* (De Gruyter Oldenbourg, 2014).
- ³²P. B. Allen and J. P. Nery, "Low-temperature semiconductor band-gap thermal shifts: T^4 shifts from ordinary acoustic and T^2 from piezoacoustic coupling," *Phys. Rev. B* **95**, 035211 (2017).
- ³³J. Bardeen and W. Shockley, "Deformation potentials and mobilities in non-polar crystals," *Phys. Rev.* **80**, 72 (1950).
- ³⁴W. Kohn and J. M. Luttinger, "Theory of donor states in silicon," *Phys. Rev.* **98**, 915 (1955).
- ³⁵J. C. Hensel, H. Hasegawa, and M. Nakayama, "Cyclotron resonance in uniaxially stressed silicon. ii. nature of the covalent bond," *Phys. Rev.* **138**, A225–238 (1965).
- ³⁶M. V. Klymenko, S. Rogge, and F. Remacle, "Multivalley envelope function equations and effective potentials for phosphorus impurity in silicon," *Phys. Rev. B* **92**, 195302 (2015).
- ³⁷M. J. Gullans and J. M. Taylor, "Optical control of donor spin qubits in silicon," *Phys. Rev. B* **92**, 195411 (2015).
- ³⁸G. Breit and I. I. Rabi, "Measurement of Nuclear Spin," *Phys. Rev.* **38**, 2082 (1931).
- ³⁹G. Kirczenow, "A shell model of bound multiexciton complexes in silicon," *Canadian J. Phys.* **55**, 1787 (1977).
- ⁴⁰M. Thewalt, "Excited states of donor bound excitons and bound multiexciton complexes in silicon," *Solid State Commun.* **21**, 937 (1977).

- ⁴¹C. C. Lo et al., “Hybrid optical–electrical detection of donor electron spins with bound excitons in silicon,” *Nat. Mater.* **14**, 490 (2015).
- ⁴²W. Schmid, “Auger lifetimes for excitons bound to neutral donors and acceptors in Si,” *Phys. Stat. Sol.* **84**, 529 (1977).
- ⁴³A. Yang et al., “Nuclear polarization of phosphorus donors in ²⁸Si by selective optical pumping,” in *Aip conference proceedings*, Vol. 1199, 1 (American Institute of Physics, 2010), p. 375.
- ⁴⁴A. Yang, “Optical hyperpolarization and detection of electron and nuclear spins of phosphorus donors in highly enriched ²⁸Si,” PhD Thesis (2010).
- ⁴⁵A. Yang et al., “Homogeneous linewidth of the ³¹P bound exciton transition in silicon,” *Appl. Phys. Lett.* **95**, 2007 (2009).
- ⁴⁶J. R. Klauder and P. W. Anderson, “Spectral Diffusion Decay in Spin Resonance Experiments,” *Phys. Rev.* **125**, 912 (1962).
- ⁴⁷I. Žutić, J. Fabian, and S. Das Sarma, “Spintronics: Fundamentals and applications,” *Rev. Mod. Phys.* **76**, 323 (2004).
- ⁴⁸E. Abrahams, “Donor electron spin relaxation in silicon,” *Phys. Rev.* **107**, 491 (1957).
- ⁴⁹J. H. Van Vleck, “Paramagnetic relaxation times for titanium and chrome alum,” *Phys. Rev.* **57**, 426 (1940).
- ⁵⁰R. Orbach, “On the theory of spin-lattice relaxation in paramagnetic salts,” *Proc. Phys. Soc. A* **77**, 821 (1961).
- ⁵¹T. G. Castner, “Raman spin-lattice relaxation of shallow donors in silicon,” *Phys. Rev.* **130**, 58 (1963).
- ⁵²Y. Song and H. Dery, “Analysis of phonon-induced spin relaxation processes in silicon,” *Phys. Rev. B* **86**, 085201 (2012).
- ⁵³L. M. Roth, “*g* Factor and donor spin-lattice relaxation for electrons in germanium and silicon,” *Phys. Rev.* **118**, 1534 (1960).
- ⁵⁴A. Schweiger and G. Jeschke, *Principles of pulse electron paramagnetic resonance* (Oxford University Press, 2001).
- ⁵⁵D. Suter, *The physics of laser-atom interactions*, Cambridge Studies in Modern Optics (Cambridge University Press, 1997).

- ⁵⁶M. Beck, N. V. Abrosimov, J. Hübner, and M. Oestreich, “Impact of optically induced carriers on the spin relaxation of localized electron spins in isotopically enriched silicon,” *Phys. Rev. B* **99**, 245201 (2019).
- ⁵⁷G. L. Pollack, “Kapitza resistance,” *Rev. Mod. Phys.* **41**, 48 (1969).
- ⁵⁸C. V. Madhusudana and C. Madhusudana, *Thermal contact conductance*, Vol. 79, Mechanical Engineering (Springer, 1996).
- ⁵⁹P. J. Dean, W. F. Flood, and G. Kaminsky, “Absorption due to Bound Excitons in Silicon,” *Phys. Rev.* **163**, 721 (1967).
- ⁶⁰G. G. Macfarlane, T. P. McLean, J. E. Quarrington, and V. Roberts, “Exciton and phonon effects in the absorption spectra of germanium and silicon,” *J. Phys. Chem. Solids* **8**, 388 (1959).
- ⁶¹W. Demtröder, *Laserspektroskopie* (Springer, 2007).
- ⁶²K. J. Morse et al., “Zero-field optical magnetic resonance study of phosphorus donors in 28-silicon,” *Phys. Rev. B* **97**, 115205 (2018).
- ⁶³M. Wollenhaupt et al., “Femtosecond strong-field quantum control with sinusoidally phase-modulated pulses,” *Phys. Rev. A* **73**, 063409 (2006).
- ⁶⁴J. M. Supplee, E. A. Whittaker, and W. Lenth, “Theoretical description of frequency modulation and wavelength modulation spectroscopy,” *Appl. Opt.* **33**, 6294 (1994).
- ⁶⁵R. de L. Kronig, “On the theory of dispersion of x-rays,” *J. Opt. Soc. Am.* **12**, 547 (1926).
- ⁶⁶W. Smith, *Experimental physics: principles and practice for the laboratory* (CRC Press, 2020).
- ⁶⁷Z. Instruments, “Principles of lock-in detection and the state of the art,” *CH-8005 Zurich, Switzerland* (2016).
- ⁶⁸H. Sun, *A practical guide to handling laser diode beams*, Vol. 147 (Springer, 2015).
- ⁶⁹W. W. Chow and S. W. Koch, *Semiconductor-laser fundamentals: physics of the gain materials* (Springer Science & Business Media, 1999).

- ⁷⁰S. Bennetts et al., “External cavity diode lasers with 5kHz linewidth and 200nm tuning range at $1.55\mu\text{m}$ and methods for linewidth measurement,” *Opt. Express* **22**, 10642 (2014).
- ⁷¹D. K. Shin et al., “Widely tunable, narrow linewidth external-cavity gain chip laser for spectroscopy between $1.0\mu\text{m}$ and $1.1\mu\text{m}$,” *Opt. Express* **24**, 27403 (2016).
- ⁷²N. Hodgson and H. Weber, *Laser resonators and beam propagation: fundamentals, advanced concepts, applications*, Vol. 108 (Springer, 2005).
- ⁷³T. Legero, T. Kessler, and U. Sterr, “Tuning the thermal expansion properties of optical reference cavities with fused silica mirrors,” *J. Opt. Soc. Am. B* **27**, 914 (2010).
- ⁷⁴E. D. Black, “An introduction to Pound–Drever–Hall laser frequency stabilization,” *Am. J. Phys.* **69**, 79 (2002).
- ⁷⁵J. I. Thorpe, K. Numata, and J. Livas, “Laser frequency stabilization and control through offset sideband locking to optical cavities,” *Opt. Express* **16**, 15980 (2008).
- ⁷⁶E. Sauter, N. V. Abrosimov, J. Hübner, and M. Oestreich, “Low temperature relaxation of donor bound electron spins in $^{28}\text{Si:P}$,” *Phys. Rev. Lett.* **126**, 137402 (2021).
- ⁷⁷F. du Burck and O. Lopez, “Correction of the residual amplitude modulation in fm spectroscopy,” in *Conference on precision electromagnetic measurements* (2002), p. 226.
- ⁷⁸F. du Burck, O. Lopez, and A. El Basri, “Narrow-band correction of the residual amplitude modulation in frequency-modulation spectroscopy,” *IEEE Trans. Instrum. Meas.* **52**, 288 (2003).
- ⁷⁹H. A. Kierstead, “Lambda curve of liquid He^4 ,” *Phys. Rev.* **162**, 153 (1967).
- ⁸⁰B. Welber, C. Kim, M. Cardona, and S. Rodriguez, “Dependence of the indirect energy gap of silicon on hydrostatic pressure,” *Solid State Commun.* **17**, 1021 (1975).
- ⁸¹P. Dirksen, A. Henstra, and W. T. Wenckebach, “An electron spin echo study of donor-acceptor recombination,” *J. Phys. Condens. Matter* **1**, 7085 (1989).

- ⁸²J. H. Wesenberg and K. Mølmer, “Field inside a random distribution of parallel dipoles,” *Phys. Rev. Lett.* **93**, 143903 (2004).
- ⁸³M. L. W. Thewalt et al., “Direct observation of the donor nuclear spin in a near-gap bound exciton transition: ³¹P in highly enriched ²⁸Si,” *J. Appl. Phys.* **101**, 081724 (2007).
- ⁸⁴J Niemela, “Ultra-high Rayleigh number convection in cryogenic helium gas,” *Physica B* **284-288**, 61 (2000).
- ⁸⁵Q. Hu et al., “Low-temperature specific heat of isotopically enriched silicon single crystals,” *Phys. Lett. A* **299**, 656 (2002).
- ⁸⁶W. Demtröder, *Experimentalphysik 1* (Springer, Berlin, 2015), p. 185.
- ⁸⁷H Marshak, “Nuclear orientation thermometry,” *J. Res. Na. Bur. Stand.* **88**, 175 (1983).
- ⁸⁸T. G. Castner, “Orbach spin-lattice relaxation of shallow donors in silicon,” *Phys. Rev.* **155**, 816 (1967).
- ⁸⁹G. Yang and A. Honig, “Concentration- and Compensation-Dependent Spin-Lattice Relaxation in n-Type Silicon,” *Phys. Rev.* **168**, 271 (1968).
- ⁹⁰J. Marko and A. Honig, “Measurements of concentration-dependent spin-lattice relaxation times in phosphorus-doped silicon at low temperatures,” *Solid State Commun.* **8**, 1639 (1970).
- ⁹¹P. R. Cullis and J. R. Marko, “Electron paramagnetic resonance properties of n-type silicon in the intermediate impurity-concentration range,” *Phys. Rev. B* **11**, 4184 (1975).
- ⁹²K. Sugihara, “Concentration dependent spin-lattice relaxation in n-type silicon,” *J. Phys. Chem. Sol.* **29**, 1099 (1968).
- ⁹³A. Honig and E. Stupp, “Electron spin-lattice relaxation in phosphorus-doped silicon,” *Phys. Rev.* **117**, 69 (1960).
- ⁹⁴H. Hasegawa, “Spin-lattice relaxation of shallow donor states in Ge and Si through a direct phonon process,” *Phys. Rev.* **118**, 1523 (1960).
- ⁹⁵A. Morello et al., “Single-shot readout of an electron spin in silicon,” *Nature* **467**, 687 (2010).

- ⁹⁶W. E. Moerner, ed., *Persistent spectral hole-burning: science and applications* (Springer Berlin Heidelberg, 1988).
- ⁹⁷Y. M. He et al., “Coherently driving a single quantum two-level system with dichromatic laser pulses,” *Nat. Phys.* **15**, 941 (2019).
- ⁹⁸S. Roy, S. Saha, J. Sarkar, and C. Mitra, “Development of planar microstrip resonators for electron spin resonance spectroscopy,” *EPJ Appl. Phys.* **90**, 31001 (2020).
- ⁹⁹A. Bienfait et al., “Reaching the quantum limit of sensitivity in electron spin resonance,” *Nature Nanotech.* **11**, 253 (2015).
- ¹⁰⁰S. Weichselbaumer et al., “Quantitative modeling of superconducting planar resonators for electron spin resonance,” *Phys. Rev. Appl.* **12**, 024021 (2019).
- ¹⁰¹L. McKenzie-Sell et al., “Low-impedance superconducting microwave resonators for strong coupling to small magnetic mode volumes,” *Phys. Rev. B* **99**, 140414 (2019).
- ¹⁰²C. Eichler, A. J. Sigillito, S. A. Lyon, and J. R. Petta, “Electron spin resonance at the level of 10^4 spins using low impedance superconducting resonators,” *Phys. Rev. Lett.* **118**, 037701 (2017).
- ¹⁰³H. R. Mohebbi et al., “Composite arrays of superconducting microstrip line resonators,” *J. Appl. Phys.* **115**, 094502 (2014).
- ¹⁰⁴S. Kwon et al., “Magnetic field dependent microwave losses in superconducting niobium microstrip resonators,” *J. Appl. Phys.* **124**, 033903 (2018).

SCIENTIFIC CONTRIBUTIONS

JOURNAL PUBLICATIONS

- ¹E. Sauter, N. V. Abrosimov, J. Hübner, and M. Oestreich, “Low temperature relaxation of donor bound electron spins in $^{28}\text{Si:P}$,” *Phys. Rev. Lett.* **126**, 137402 (2021).
- ²E. Sauter, N. V. Abrosimov, J. Hübner, and M. Oestreich, “Time-resolved temperature dependence of the bandgap of $^{28}\text{Si:P}$ at very low temperatures,” **Submitted** (2022).
- ³R. Peibst et al., “From PERC to tandem: POLO- and p^+/n^+ poly-Si tunneling junction as interface between bottom and top cell,” *IEEE J. Photovolt.* **9**, 49 (2019).
- ⁴C Hollemann et al., “Separating the two polarities of the POLO contacts of an 26.1%-efficient IBC solar cell,” *Sci. Rep.* **10**, 658 (2020).

CONFERENCE CONTRIBUTIONS

- ¹E. Sauter, N. V. Abrosimov, J. Hübner, and M. Oestreich, “Temperature dependence of the bandgap of ^{28}Si and its use as time-resolved, high precision thermometer,” *Verhandlungen der DPG* (2022).
- ²E. Sauter, “Optical spin injection in silicon,” *Verhandlungen der DPG* (2019).

SUPERVISED THESES

- ¹R. Lennard, “Herstellung und charakterisierung von supraleitenden mikroresonatoren für elektronenspinresonanz,” Masterarbeit, Leibniz Universität Hannover, Inst. f. FKP (2022).
- ²K. Rempel, “Spektroskopie an $^{28}\text{Si:P}$ im tieftemperaturregime,” Bachelorarbeit, Leibniz Universität Hannover, Inst. f. FKP (2022).

- ³R. Lennard, “Installation eines tieftemperatur-messplatzes für zeitaufgelöste photolumineszenz-spektroskopie an GaAs,” Bachelorarbeit, Leibniz Universität Hannover, Inst. f. FKP (2020).
- ⁴M. Bonkowski, “Optische messungen der ladungsträgerlebenszeit in intrinsischem silizium,” Bachelorarbeit, Leibniz Universität Hannover, Inst. f. FKP (2019).
- ⁵J. Bäuerlein, “Optische untersuchung der spindynamik in silizium,” Bachelorarbeit, Leibniz Universität Hannover, Inst. f. FKP (2019).

CURRICULUM VITAE



Name	Eduard Enrico Sauter
Born	1995 in Germany - Brunswick
06/2005 - 06/2013	Gymnasium Gaußschule in Brunswick
06/2013	Abitur
09/2013 - 09/2016	Bachelor Thesis “Spin Dynamics of Excitons in a GaAs Quantum Well” at the LUH
09/2016 - 09/2018	Master Thesis “Spin Dynamics and Selection Rules in Bulk Silicon” at the LUH
since 10/2018	Research associate and PhD student at the Institute for Solid State Physics - Nanostructures Group, LUH

NOTES
